Functionalising AFM tips for pick and place manipulation of micro and nanoparticles



Soh Jia Hao Eugene

St. Edmund Hall

University of Oxford

A thesis submitted for the degree of

Doctor of Philosophy

Trinity 2021

This thesis is dedicated to
my parents
Soh Gin Ghee and Lim Gek Lay

Acknowledgements

This thesis is the result of the many people providing me not only with scientific guidance and support, but also encouragement and a friendly work environment.

Firstly, I would like to thank my supervisor Harish Bhaskaran for allowing me to pursue my ideas freely while providing valuable guidance along the way. He is always present to provide encouragement and show appreciation whether experiments work or not. I appreciate the spontaneous lab/office visits and coffee corner discussions. I am grateful to be part of his remarkable research group. I must also thank Benjamin Porter and Nhlakanipho Mkhize who taught me many experimental and technical skills when I was a new student.

I also had the wonderful opportunity to work with collaborators from the Institute of Materials Research and Engineering (IMRE). I owe my thanks to Sean O'Shea for teaching me the wonders of the atomic force microscope, which also began my research journey in this field. I thoroughly enjoyed the time we spend conducting and discussing experiments together. I must also thank Dan Daniel for introducing me to interesting ideas and experimental challenges. I appreciate his guidance and have learned a lot from him. Thanks also goes to Lu Ding and Sergey Gorelik for all their guidance and support on the nanoantenna project.

A big thank you to the members of the Advanced Manufacturing and Engineering group for all the help you have provided. Getting through a thesis requires more than academic support; the friendship and bonds forged over the years are very important too. To my good friends and colleagues Tara Milne, James Tan, Xuan Li, Yu Shu and Utku Ali, my experience here would be so much less fun without you. All the nights out, BBQ, punting, etc. will all be kept in good memory.

Finally, and most importantly, I would like to thank my parents and my sister for listening to all my academic woes and providing support and encouragement all the time.

Abstract

Nanofabrication techniques have always been at the heart of realising novel functional nanodevices. Modern nanomanufacturing relies heavily on lithography, which is the patterning of two-dimensional structures on radiation sensitive polymers in multiple steps to create nanodevices. Although suitable for mass manufacturing, lithography lacks the capability to precisely manipulate a single to few particles. The main goal of my research is to develop new technologies that are capable of manipulating single to few particles ranging from nanometer to micrometer scale. With the development of these new particle manipulation technologies, we demonstrate new applications that would have been difficult to realise with current existing nanomanufacturing methods. Here, we will look at how the atomic force microscope (AFM) can be used as a particle manipulator. The cantilever of the AFM acts as a robotic arm with nanometer precision in all three spatial dimensions. We show that by appropriately functionalising or modifying the cantilever, we can manipulate different types of particles (from nano- to micrometer sized) for various applications.

We demonstrate that gold nanoparticles can be picked up by an AFM tip modified with a suitably attractive monolayer. However, picking up a single nanoparticle with this method proved challenging due to monolayers diffusing through each other over time. Hence, the picking up could not be localised, which led to the use of dielectrophoresis. We show that by coating the tip with specific coatings (i.e. GST, carbon) that are capable of forming conductive filaments, the electric field can be further localised resulting in the picking up of single 20 nm gold particles — a significant improvement compared to tips without the coating. We show that these filamentary probes also have applications in high-resolution Kelvin probe force microscopy. We achieved a spatial resolution improvement over commercial platinum probes by $\sim$48%.

Besides suitable coatings, microchannels can be fabricated within the cantilever. Such cantilevers are commercially available and are often used to deliver small amounts of fluids with a pressure controller. We use this technology to aspirate and dispense 1 μm particles that are larger than the aperture size in a liquid medium. Moreover, we can also print nanoparticle inks with the hollow cantilever in air. We developed methods to monitor the deposition process in-situ as well as image the substrate before and during deposition. This enables us to align the deposition of

nanoparticles into sub-500 nm gaps. This have direct applications in fabrication of microLEDs and hybrid photonic nanostructures.

Furthermore, we demonstrate that microparticles of liquid metal can be picked up by coating the cantilever with gold, which is more adhesive to the liquid metal compared to the polystyrene substrate. We are able to pick up and place liquid metal particles at will. Moreover, the contact area can be controlled by adjusting the applied force. We demonstrate an application of such a liquid metal droplet probe system by making small area ($\sim$4 – 12 μm^2) molecular junctions in the weak-coupling regime.

There are various ways an AFM cantilever can be modified to facilitate the manipulation of nano- and microparticles. These are general techniques and the concepts presented here can be extended and applied to many different systems. With this understanding, experimental parameters such as coating material and voltages can be modified accordingly depending on the particle type and application. The ability to manipulate single to few particles will enable interdisciplinary researchers to study novel interactions between functional particles and nanostructures.

Contents

List of Figures xiii

List of Abbreviations xxi

1 Introduction 1
- 1.1 Top-down vs bottom-up nanofabrication . . . 1
- 1.2 Particle nanomanipulation . . . 3
  - 1.2.1 Building hybrid devices . . . 5
- 1.3 Thesis goals . . . 5

2 State of the art 7
- 2.1 Optical manipulation . . . 8
- 2.2 Self-assembly of particles . . . 12
- 2.3 External field driven manipulation . . . 17
- 2.4 Microgrippers . . . 20
- 2.5 Scanning probe manipulation . . . 21
  - 2.5.1 Operating principles . . . 22
  - 2.5.2 Pushing with the AFM tip . . . 24
  - 2.5.3 Electric field manipulation . . . 25
  - 2.5.4 Chemical functionalisation of the AFM tip . . . 28
  - 2.5.5 Dip-Pen technique and its derivatives . . . 30
- 2.6 Current challenges and opportunities with particle manipulation . . . 36
- 2.7 Chapter summary . . . 38

3 Coating of self-assembled monolayers 39
- 3.1 Introduction . . . 39
- 3.2 Aims of chapter . . . 40
- 3.3 Self-assembly of nanoparticles on molecular monolayers . . . 40
  - 3.3.1 Materials and methods . . . 41
  - 3.3.2 Gold nanoparticles and their affinity to SAMs . . . 42
  - 3.3.3 AFM tips . . . 45
- 3.4 Chapter Summary . . . 47

4 Coatings with conductive nano-filaments **49**
4.1 Introduction . . . 49
4.2 Aims of chapter . . . 50
4.3 Creating high resolution tips . . . 50
4.3.1 Coating, and switching in conductive AFM . . . 51
4.3.2 Switching mechanism . . . 52
4.3.3 Stability of filamentary probes . . . 55
4.4 Single nanoparticle nanomanipulation . . . 56
4.4.1 Dielectrophoresis - Theory . . . 56
4.4.2 Materials and Methods . . . 58
4.4.3 Results and discussion . . . 59
4.5 Applications for high-resolution conductive AFM . . . 62
4.5.1 Kelvin probe microscopy - Theory . . . 62
4.5.2 Materials and methods . . . 65
4.5.3 Results and discussion . . . 68
4.6 Chapter Summary . . . 70

5 Hollow cantilevers **73**
5.1 Introduction . . . 73
5.2 Aims of chapter . . . 75
5.3 FluidFM Set-up . . . 75
5.4 Pick and place of 1 μm particles . . . 76
5.4.1 Materials and methods . . . 76
5.4.2 Results and discussion . . . 76
5.4.3 In-situ monitoring . . . 78
5.4.4 Exploring pick and place in air . . . 78
5.5 Nanoprinting . . . 81
5.5.1 Nanoparticle inks . . . 81
5.5.2 Printing quantum dots onto micro- and nano- structures . . . 88
5.5.3 Alignment to structures . . . 91
5.5.4 In-situ monitoring and troubleshooting . . . 94
5.6 Chapter summary . . . 95

6 Tipless cantilevers for picking up EGaIn droplets **99**
6.1 Introduction . . . 100
6.2 Aims of chapter . . . 100
6.3 Background . . . 101
6.3.1 EGaIn and its manipulation techniques . . . 101
6.3.2 EGaIn as a technique to make molecular junctions . . . 102
6.4 Materials and Methods . . . 103

6.4.1 Creating EGaIn droplet probes . . . 103
6.4.2 Substrate preparation . . . 105
6.4.3 Self-assembly . . . 105
6.5 Characterisation of EGaIn droplet probes . . . 105
6.5.1 Surface roughness of picked-up EGaIn droplet . . . 105
6.5.2 Contact mechanics of EGaIn droplets . . . 107
6.5.3 Crack formation in millimetric-sized droplet . . . 112
6.5.4 The effect of oxide for electrical measurements . . . 113
6.6 Benchmarking on alkanethiol SAMs . . . 114
6.6.1 Stability of droplet probe . . . 117
6.7 Chapter Summary . . . 117

7 Conclusions **119**

Appendices

A Attempts at placing single particle **127**
A.1 Placing on APTES coated substrate . . . 127
A.2 Placing on photoresist substrates . . . 128

B Attempts at picking up single liquid metal microspheres **131**
B.1 Picking up EGaIn microspheres at the liquid-air interface . . . 131

References **135**

List of Figures

1.1 Schematic describing the top-down and bottom-up approaches to nanofabrication. Adapted from [2]. 2

2.1 (a) Illustration of the operating mechanism of the opto-thermo-electrohydrodynamic tweezers system. By moving the laser on the plasmonic nanohole array, a single particle (blue sphere) is trapped away from the laser and follows the motion of the laser beam horizontally along the pattern edge. The inset shows the forces acting on a trapped particle when the laser and a.c. electric field is applied. ACEO, a.c. electro-osmotic flow; F_{ACEO} the drag force from the a.c. electro-osmotic flow; F_{ETP}, the drag force from the electrothermoplasmonic (ETP) flow; F_{es}, the particle–surface interaction force. (b) Electric field profile when a laser is focused at the centre of the nanohole array. At the trapping position, the electric field from the light is small enough to eliminate its influence on the trapped particle (adapted from [42]). 11

2.2 Schematic showing the steps to form electrostatically assembled alternating layers of gold and silver colloidal particles (adapted from [58]). 14

2.3 (a) The meniscus of a colloidal suspension containing 60 nm Au particles is moving over the patterned PDMS surface of a printing plate. (b) Simulation of the evaporation (colours indicate concentrations) and the streamlines (red lines) of the laminar flow that drags along particles towards the three-phase contact line, where they form an accumulation zone. The main panel is a simulation at a relative humidity (RH) of 50% and the inset for a RH of 95%. (c,d) The accumulation zone, visible in the micrographs as a bright yellow line, moves over the printing plate. Depending on the geometry they encounter, particles at the contact line form sparse patterns, for example, arrays (c) or dense arrangements such as lines (d) (adapted from [73]). 16

2.4 Schematics of the two-stage mechanism of crystallization deduced from the set of diffraction and microscopy data. (a) Immediately after the field is applied, the particles align in chains due to the induced dipole-dipole interactions. Simultaneously, the gradient-driven DEP force pulls the chains and particles toward the surface of the substrate between the electrodes. (b) The particle chains confined on the surface crystallize to form 2D hexagonal crystals aligned by the field (adapted from [80]). 18

2.5 SEM image of a three-pronged microgripper capable of both grasping and active release of microobjects (adapted from [106]). 21

2.6 Schematic showing the basic components of an AFM. 23

2.7 Nanomanipulation with visual guidance. (a) An image taken at 1 Hz before any manipulation. The nanoparticle enclosed in the arrow mark was kicked to the right using the standard method. Following the kicking event, images were taken at a scanning speed of (b) 1 Hz and (c) 5 Hz. In both cases, the nanoparticle enclosed in the circles moved a short distance but stopped before reaching the target position. (d) Controlled manipulation was achieved at a higher scanning rate of 7 Hz. The scanning speed was abruptly reduced from 7 to 1 Hz once the target position was reached. Ghost images behind the moving particle provide a useful and clear visual guidance during the manipulation (adapted from [126]). 26

2.8 Attracting particles with positive DEP (pDEP) and repelling and holding them with negative DEP (nDEP). All scale bars are 5 μm. (a) Schematic of a particle being drawn into the field maxima with pDEP. (b-f) A time sequence of fluorescence images depicting the bead marked with the red arrow being drawn into the tip with pDEP. The schematic cross section is overlaid in the approximate position of the triaxial probe as a guide to the eye. (g) Schematic of one particle being repelled from the probe by nDEP and another being held in the nDEP trap. (h-l) A time sequence of fluorescence images depicting the triaxial probe repelling beads with nDEP. The majority of the beads are pushed back into suspension while the beads marked with the red arrow are held in the nDEP trap (adapted from [131]). 28

2.9 A schematic representation of the electro-enhanced capillary nanomanipulation technique. (a) Initial situation with the probe at some distance from the nanoparticle; (b) formation and growth of the water bridge by the application of a voltage pulse; (c) probe withdrawal and capillary force pulling the nanoparticle upwards; (d) nanoparticle detachment and displacement while attached to the probe; (e) release of the nanoparticle by contact with the substrate; (f) piezoretracted and nanoparticle in the final situation (adapted from [138]). 29

2.10 SEM images showing (a) an unmodified silicon nitride tip (Olympus TR400PSA) and (b) a tip coated with gold nanoparticles, which have an average size of 40 nm. Images of the tips modified with passive and active layers terminated with single gold nanoparticles with approximate sizes of 25 and 14 nm are shown in (c) and (d), respectively. In all cases, the tips were sputtered with a gold coating of about 2 nm to enhance the quality of the image (adapted from [141]). 31

2.11 (a) Schematic of Au nanoparticle delivery by the nanofountain probe, (b) Optical image of nanofountain pen cantilevers, inset: aperture of probe tip (adapted from [160]). 33

2.12 (a-d) Schematics of the fabrication procedure of a polymer composite microtube. (a) Deposition of PMMA/PPy NPs at the edge of a meniscus due to outward flow in a fast evaporating solvent, forming a ring-like deposit. (b) As the micropipette is slowly pulled up (< 25 μm/s) away from the substrate, the outward liquid flow continually accumulates the NPs on the ring-like deposit, forming a microtube. Here the accumulation is confined within the meniscus that is guided upward by the micropipette. (c) Once exposed to the air by taking away the micropipette from the microtube, the remanent solution inside the microtube rapidly evaporates, finally leaving a hollow microtube in (d). The four sequential optical images, (e-h), taken in real-time during the abrication, show the corresponding processes of (a-d), respectively (adapted from [169]). 35

3.1 The chemical structures of (a) APTES, (b) POTS, (c) TMODS and (d) MPS. (e) Schematic showing a silicon oxide substrate after treatment with piranha solution to generate hydroxyl groups, followed by silanization with APTES. The positively charged amine groups electrostatically attracts negatively charged citrate-capped gold nanoparticles in solution. 41

3.2 SEM images of gold nanoparticles assembled on (a) APTES, (b) TMODS, (c) POTS and (d) MPS. 43
3.3 SEM images of gold nanoparticles after a phase transfer to hexane assembled on MPS. 44
3.4 Schematic of the phase transfer process of gold nanoparticles from aqueous solution to hexane. The ligands are exchanged from citrate to oleate groups. The oleate groups have better affinty to hexane compared to the aqueous solution, thus achieving the phase transfer. 44
3.5 SEM images of AFM tips coated with (a) APTES, (b) TMODS, (c) POTS and (d) nothing. 45
3.6 (a) Schematic representation of how a combination of monolayers will lead to localised assembly of gold nanoparticles. SEM images of (b) tip coated with APTES only and (c) tip coated with POTS followed by APTES only at the apex. 46
3.7 The change in contact angle of APTES functionalised substrates in POTS and vice versa over time. The inset shows water contact angle images of substrates coated with POTS (top) and APTES (bottom). 48

4.1 Schematic of an AFM tip illustrating how a conductive filament can enhance the resolution of electrical measurements. The high-resolution probe has a small volume of low resistance coating surrounded by the higher resistance coating. This confines the electric field to a region smaller than the dimensions of the probe tip, thus enhancing electrical resolution. 51
4.2 (a) Representative I-V curve measured when switching the carbon coating phase on the AFM tip. As the voltage is ramped up from 0 to 4 V, the sudden spike in current at about 3 V suggests a change from a high resistance state to a low resistance state. A linear line on the reverse ramp indicates that the phase change is non-volatile. (b) Switching voltage versus thickness of amorphous carbon coating. (c) Switching voltages of varied composition probes coated with 10 nm of amorphous carbon. (d) Switching voltages on different substrate materials using silicon probes coated with 10 nm of carbon. 54
4.3 (a) SEM images taken of a carbon coated tip in the LRS 2 weeks after experiments, stored in ambient conditions. The yellow colour in (a) highlights the carbon coating. (b) shows the original SEM image of the same tip. 55

4.4 (a) Schematic describing dielectrophoresis. A non-uniform field is produced between the sharp and planar electrode. The particle will be attracted to or repelled from the sharp electrode in positive or negative DEP respectively. (b) Graph showing the dependence of frequency on Re[CM]. This determines whether positive or negative DEP occurs. 57
4.5 (a) Schematic showing the process of fabricating highresolution probes. The reconfigurable material is coated onto an AFM tip followed by switching a nanoscale conductive filament at the apex of the tip. The tip can then be used to pick up a nanoparticle through dielectrophoresis or to conduct high-resolution electrical measurements. (b) SEM images of a representative carbon-coated platinum tip before threshold switching, (c) after switching, and (d) after dielectrophoresis to pick up the 20 nm gold nanoparticle. The yellow color highlights the carbon coating. The scale bars are 200 nm. 60
4.6 Images compare the effectiveness of probes for capturing nanoparticles using electric fields with and without conductive filamentation. (a) An SEM (back scattered electron) image of a representative carbon-coated platinum tip after dielectrophoresis to pick up a single gold nanoparticle. A large portion of the tip cone illustrates the locality of the electric field resulting in single nanoparticle capturing only at the apex. (b) Carbon-coated tip without creation of a nanoscale conductive filament, (c) Pt tip without a coating, (d) filamentary GST tip, and (e) filamentary carbon-coated tip picks a single Au nanoparticle. Images are a compilation collected by SEM and TEM, thus the contrast reversal. 61
4.7 (a) STEM high-angle annular dark field image (left) and corresponding EDX maps of a representative switched GST tip after picking up gold nanoparticles from a single contact point on the apex of the tip. (b) STEM image and corresponding EDX maps of a representative switched carbon tip after picking up a 20 nm gold nanoparticle. EDX confirms the nanoparticle is indeed gold. 61
4.8 (a) Absorption spectra of the EVA-MWCNT film. (b) Absorption spectra of chloroform, EVA in chloroform and EVA-MWCNT in chloroform. 66
4.9 Schematic of the set up for FM-KPFM. 67
4.10 SEM image of CNTs. 69
4.11 Topography, CPD, and the corresponding line sections of scans conducted with (a-f) platinum tips, (g-l) GST, and (m-r) carbon tips with AM- and FM-KPFM on 10 nm diameter carbon nanotubes spray-coated on ITO-substrates. 71

5.1 (a) FluidFM set up consisting of the AFM on top of an inverted microscope. (b) The probe is connected to an external pump via the pneumatic connector. 76
5.2 (a) Optical image and (b) difference image of tip before filling. (c) optical image and (d) difference image of tip after filling. The contrast is much easier to see in the difference image. 77
5.3 Optical image of the substrate (a) before and (b) after pick and place operation. The black boxes outline the region of interests. 78
5.4 Force curves before and after picking up a 1 μm particle. 79
5.5 Adhesion measured with fluidFM tips in (a) air and (b) water while varying pressure applied. Higher adhesion is generally observed when negative pressures are applied and vice versa. Variability is due to the irregular shaped tip. Adhesion in water is greatly reduced. . . . 80
5.6 (a) AFM image and (b) corresponding line section of rhodamine B dye deposited with 200 mbar overpressure. (c) AFM image and (d) corresponding line section of rhodamine B dye deposited with 20 mbar overpressure. Deposition droplet size can be controlled by varying overpressure. 83
5.7 (a) AFM image of the overall region. (b) zoomed in image on one of the dye droplets showing the volcano shaped structure. (c) 3D view of the volcano-shaped structure and (d) corresponding linere cross-section. (e) Schematic showing how the final geometry is determined by the droplet wrapping around the tip in fast evaporating droplets. 84
5.8 (a) SEM image of overall region and (b) zoomed in region of larger dye droplets. (c) SEM image of overall regions and (d) zoomed in region of smaller dye droplets exhibiting the volcano shaped structure. 85
5.9 (a) AuNP droplet on gold coated substrate. Large drop due to the wettability of the substrate. 85
5.10 (a-c) Various examples of droplets with few to single AuNP per droplet on quartz. 86
5.11 Spectrum of CdTe in water solution, the center and edge of a dried dropcasted solution and a spot deposited using FluidFM probes. . . 88
5.12 (a) AFM image showing that the well is completely filled. Its corresponding (b) optical image and (c) line section. 90
5.13 (a) Optical image and (b) photoluminescence image of an array of nanoantenna pillars with QDs printed on them. 91
5.14 AFM images of two different types of antenna structures. (a) and (c) shows the antenna before QD deposition while (b) and (d) shows the corresponding image after QD deposition. 92

5.15 (a) Vertical deflection on Au substrate. (b) Amplitude on Au substrate. (c) Vertical deflection on Quartz substrate. (d) Amplitude on quartz substrate. 93
5.16 (a) AFM image of a region of nanoantennas taken with a filled fluidFM probe in non-contact mode to and (b) its corresponding zoomed in image. 94
5.17 Vertical deflection of the cantilever vs time. The pressure applied to the reservoir is adjusted every 3s from 0 mbar to 800 mbar in increments and decrements of 200 mbar. 95
5.18 This figure shows an array where some dots are deposited, while others are not. We notice a clear difference in the retract curves. . . 96

6.1 (a) Schematic of an AFM cantilever and EGaIn droplets on a SAM substrate illustrating the ability to pick up droplets of various sizes and making molecular junctions in-situ. (b) SEM image of an EGaIn droplet after being picked up by the cantilever. 104
6.2 (a) AFM topographic image of an EGaIn droplet attached to a cantilever after the picking up process. (b) The corresponding AFM image of a zoomed-in region on the spherical droplet and (c) its corresponding line section. (d) A fitted sphere (blue line) based on a radially averaged line section (gray line) of the topographic image in (a). The contact angle is found to be $\theta_c = 148°$. (e) SEM image of the same EGaIn droplet. 106
6.3 Droplet geometries in (a) air (wetting) and (b) in ethanol (non-wetting) during force spectroscopy measurements. 107
6.4 (a, b) Force spectroscopy of an EGaIn droplet ($2R$ = 10, 12 μm) contacting the C4 surface in air and in ethanol, respectively. z is the droplet position after correcting for cantilever deflection. (c, d) Droplet geometries obtained by solving Young-Laplace equation and micrographs of the droplet's base at locations 1–3 in air. Scale bars are 4 μm. (e, f) The corresponding droplet geometries and micrographs in ethanol. Scale bars are 4 μm. (g, h) Comparison between $2r$ as predicted by Young-Laplace equation (blue lines) and observed experimentally in micrographs (red dots) in air and in ethanol, respectively. 109
6.5 (a) Droplet geometry during force spectroscopy. (b) Side view of EGaIn droplet. 109
6.6 (a) Force spectroscopy for micrometer-sized EGaIn droplet. (b) SEM image of the micrometric droplet which remains smooth after force spectroscopy. (c) Force spectroscopy for millimetre-sized EGaIn droplet. (d) Optical micrograph showing concentric cracks on the base of millimetre-sized droplet after force spectroscopy. 113

6.7 Conductive tip (a) sitting on, (b) piercing an EGaIn droplet and (c) the droplet probe AFM method. (d) Simultaneous force spectroscopy and current measurements for a conductive tip contacting the EGaIn droplet. (e) IV sweeps on C4 SAM for the three configurations in (a), (b) and (c). Each curve is an average of at least 40 separate curves. 115

6.8 (a) Schematic of the electrical set-up. The EGaIn droplet probe contacts a molecular SAM adsorbed on a template-stripped gold substrate that is grounded. The structure is connected to a source-measure unit that sources a voltage and measures the current. (b) J(V) traces of junctions of different alkanethiol lengths. The right y-axis represents the corresponding current magnitude for an average-sized junction (with microdroplet diameter of 4.76 μm). (b) Extraction of the exponential decay parameter, β from current density values taken at -5 V. The error bars represent the 95% confidence interval. 115

6.9 SEM image of (a) an EGaIn droplet probe 1 week after electrical measurements on SAM. The droplet probe remains conductive and maintains its spherical shape. (b) An EGaIn probe exposed to Hydrochloric acid vapour to remove the oxide. This results in the EGaIn losing its spherical shape as it wets and coats the cantilever. (c) Another example of an EGaIn droplet that has burst and amalgamated with gold coated cantilever. Cantilevers such as (b) and (c) will result in junctions that short-circuit and is not suitable for making reliable molecular junctions. 117

A.1 (a) AFM image and (b) CPD image taken from KPFM. The APTES monolayer is very thin, hence not obvious in the height image. However, it is clearly seen in the CPD image. 128

A.2 (a) AFM image of the PMMA substrate after attempted deposition. The curved lines are simply patterns that act as a location marker. (b) Line cross section showing the bumps created. 129

B.1 SEM images of (a) a cantilever after picking up microparticles at the water-air interface. Multiple particles are picked up. (b) the cantilever after acid treatment. (c) the same process with a patterned structure on the cantilever to localise the picking up of particles and (d) the cantilever after acid treatment. 132

List of Abbreviations

AFM . . . . . Atomic force microscope or microscopy

DEP . . . . . Dielectrophoresis

DPN . . . . . Dip-pen nanolithography

EGaIn . . . . . Eutectic gallium-indium alloy

GST . . . . . Germanium-antimony-tellurium, $Ge_2Sb_2Te_5$

KPFM . . . . Kelvin probe force microscope or microscopy

SAM . . . . . Self-assembled monolayer

SEM . . . . . Scanning electron microscope or microscopy

STM . . . . . Scanning tunnelling microscope or microscopy

Standard engineering delivers artifacts; exploratory engineering delivers knowledge.

— K. Eric Drexler, *Radical Abundance: How a Revolution in Nanotechnology Will Change Civilization* [1]

1 Introduction

Contents

1.1 Top-down vs bottom-up nanofabrication 1
1.2 Particle nanomanipulation 3
1.2.1 Building hybrid devices 5
1.3 Thesis goals 5

As nanotechnology and nanoscience continue to develop, new materials, structures and applications will definitely be discovered. Developing new nanofabrication techniques will enable such novel designs to be fabricated, tested and eventually mass produced. This introduction will give an overview on mainstream nanofabrication techniques which provide the foundation to understanding the various nanofabrication techniques mentioned. Furthermore, the importance of finding new techniques to manipulate nanoparticles will be discussed. In the last section, I present the scope and goals of this thesis.

1.1 Top-down vs bottom-up nanofabrication

Nanofabrication techniques are generally grouped into two categories: top-down and bottom-up techniques (see Fig. 1.1). In the top-down approach, a piece of material is eroded away until the desired shape or structure is obtained. This

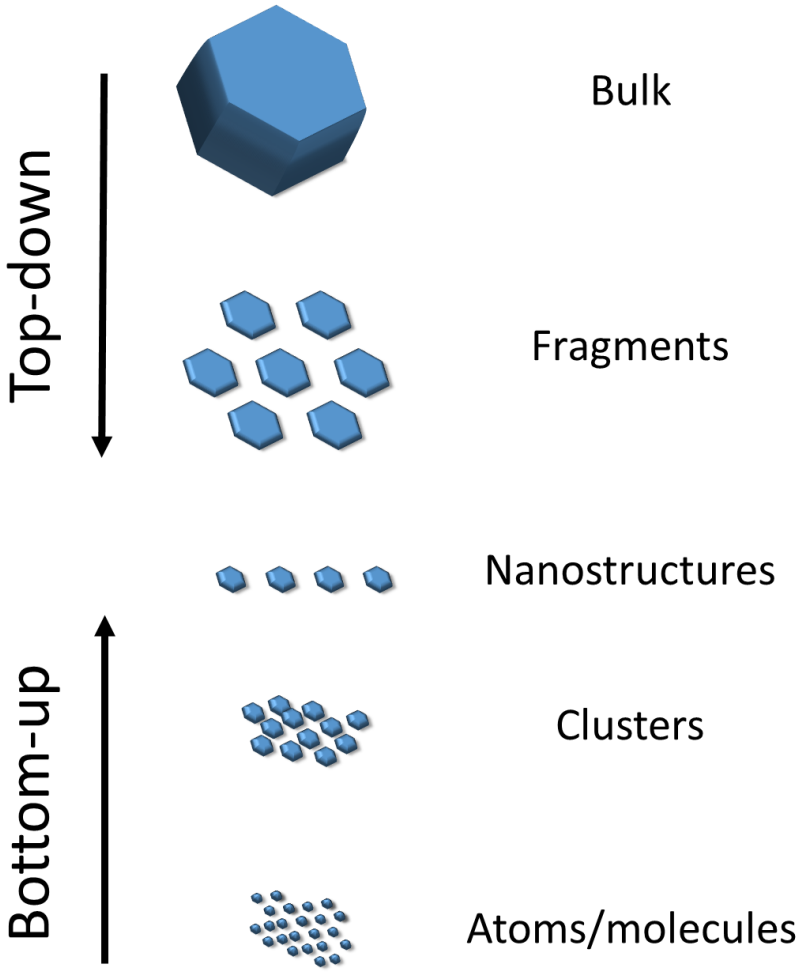


Figure 1.1: Schematic describing the top-down and bottom-up approaches to nanofabrication. Adapted from [2].

is commonly achieved through chemical means by acid etching, or mechanical means through the use of ultraviolet light, electron beams (e-beam) or X-rays. Photolithography (using light) and electron-beam lithography (using electrons) are one of the most commercially successful and commonly used techniques in the semiconductor industry for patterning two-dimensional nanoscale features. In these techniques, the surface to be patterned is coated with a photoresist. Exposing the photoresist to photons or electrons can alter its solubility. By selectively exposing the photoresist, followed by a removal step of immersing in a suitable solvent, feature sizes in the order of hundreds to tens of nanometers can be achieved. Thereafter, using the remaining photoresist as a mask, etching processes or vapour

deposition processes may be used to put patterns onto the substrate. Other top-down approaches include scanning probe lithography and nanoimprint lithography, among others. However, the subtractive nature of top-down nanofabrication techniques is often considered wasteful.

In contrast, the bottom-up approach builds up a more complex structure or assembly from individual basic building blocks which can include atoms, molecules and nanoparticles. Self assembly techniques often make use of chemical or physical forces at the nanoscale to assemble basic units into larger structures. This approach is promising as it leads to little to no wastage. However, bottom-up approaches often lack the ability to precisely position these individual building blocks.

By combining the best aspects of top-down processes such as e-beam lithography with bottom-up processes based on self assembly, nanoparticles can be patterned within nanometer precision [3].

1.2 Particle nanomanipulation

Our microelectronics technology has allowed us to shrink room-sized computers in the 1950s to silicon chips which make up our pocket-sized computers we have today. The shrinkage is made possible by advances in the various top-down approaches discussed above. The transistors that make up individual components of these micro-circuits are still made up of trillions of atoms. In the new style of technology that Drexler envisioned in his 1986 book *Engines of Creation*, these components are considered gargantuan. The new technology which he calls "molecular technology" will handle atoms and molecules with control and precision [4]. He envisioned a "molecular assembler", which is a nanorobot that is capable of manipulating individual atoms to build a desired product.

Just four years after Drexler's vision of "molecular technology", Eigler and Schweizer have managed to rearrange Xe atoms on a Ni substrate to spell out "IBM" with the use of a scanning tunneling microscope (STM) [5]. Following this landmark achievement, other groups have successfully manipulated atoms [6], molecules [7] and nanoparticles [8] with the use of an atomic force microscope

(AFM). Despite progress in single particle manipulation down to the atomic scale, there are critics on how realistic a "molecular assembler" will be. Smalley, an outspoken opponent of Drexler's ideas, raises two problems with the concept of a molecular assembler. He refers to them as the "fat fingers problem" and "sticky fingers problem". The former problem expresses how it is difficult to position all the necessary nanomanipulators with their tips or "fingers" in a nanometer area of assembly. The latter problem explains the difficulty of positioning one atom on top of another with a similar size and "stickiness".

Regardless of the arguments against "molecular assemblers", research into new approaches to manipulate atoms and nanoparticles will no doubt continue. The STM is still one of our most precise nanomanipulator and has been used to fabricate single atom transistors for quantum computing [9]. However, it has requirements such as a vacuum environment, cryogenic temperatures and conductive substrates.

The conditions required to manipulate micrometer sized particles are less strict and we have many more options available. Microgrippers can be fabricated with e-beam lithography and serve as tiny hands to move micro objects around [10]. The forces generated by a beam of light can also be used to trapped particles. The current state of the art techniques for particle manipulation will be discussed in greater detail in Chapter 2.

We have the STM, capable of manipulating atoms and molecules, the smallest building blocks of nature. And various other approaches such as microgrippers and optical traps to manipulate micrometer sized particles. However, few reliable techniques to trap and manipulate nanometer sized particles with nanometer scale precision at ambient conditions are available.

Nanometric sized particles, in a size region between cells and atomic ensembles, are important and have many interesting electrical and optical properties. Being in the right size range, it has interactions with visible light which leads to many optical applications too [11].

1.2.1 Building hybrid devices

The integration of functional nanoparticles with electronic or photonic structures has led to various novel device designs which exceed the functionality of the individual subunits. It opens the door to three dimensional structures and new approaches for hyper-integration. For example, single particle semiconductor devices have been fabricated and studied [12, 13]. In hybrid photonic devices, metallic or semiconducting nanoparticles can play the part of emitters, optical antennas or waveguides. The interaction of these components with other photonic structures depends on their size, geometry and relative locations. For example, gold nanoparticles have been manipulated onto photonic cavities to study the interactions and resonances between this coupled system [14].

Moreover, complicated hybrid structures have been proposed and studied only numerically [15]. Fabrication of such devices is challenging with conventional top-down approaches. Bottom-up approaches also currently lack precise positioning capabilities. Therefore, in order to explore and reveal the intrinsic properties of such novel hybrid nanodevices, methods to reliably trap and manipulate nanoparticles, ideally in a pick-and-place fashion, is required. Scanning probe based methods are one of the most promising ways to achieve this.

1.3 Thesis goals

The aim of this thesis is to explore and develop new techniques of nanoparticle manipulation in ambient conditions. This will pave the way to creating novel devices that traditional nanofabrication techniques have difficulty achieving. After summarising the importance of particle manipulation at the nanoscale and learning about the state of the art techniques (Chapter 2), the rest of the thesis will present the following 4 main results:

1. Exploring the use of self-assembled monolayers (SAMs) to localise the pick up of gold nanoparticles on AFM tips (Chapter 3).

2. Present the invention of a high-resolution electrical AFM probe that is capable of picking up single 20 nm gold particles. The high resolution probe also improves the resolution of conductive AFM techniques which we demonstrate with Kelvin probe force microscopy (Chapter 4).

3. Illustrate the use of a hollowed cantilever technology (fluidFM) to demonstrate pick and place of micron-sized particles as well as deposition of various functional nanoparticles for optical applications (Chapter 5).

4. Demonstrate the direct manipulation of eutectic Gallium-Indium (EGaIn) microparticles to make small area molecular junctions (Chapter 6).

The final chapter summarises the conclusions and suggests ideas in which the work can be further developed.

I did then what I knew how to do. Now that I know better, I do better.

— Maya Angelou

2 State of the art

Contents

2.1 Optical manipulation 8
2.2 Self-assembly of particles 12
2.3 External field driven manipulation 17
2.4 Microgrippers 20
2.5 Scanning probe manipulation 21
2.5.1 Operating principles 22
2.5.2 Pushing with the AFM tip 24
2.5.3 Electric field manipulation 25
2.5.4 Chemical functionalisation of the AFM tip 28
2.5.5 Dip-Pen technique and its derivatives 30
2.6 Current challenges and opportunities with particle manipulation 36
2.7 Chapter summary 38

We have seen how important the manipulation of nanoparticles is for electronic and photonic applications. In the beginning of this chapter, we will discuss the state of the art of particle manipulation from the micro to atomic scale.

In the later sections, the focus will be on scanning probe techniques. As it is the main technique used in this thesis, the important principles of the AFM will be introduced as well. We conclude this chapter by discussing the general challenges and opportunities in particle manipulation.

2.1 Optical manipulation

In general, the change of direction or absorption of light by a body results in transfer of all or part of its momentum from the light beam to the body via elastic or inelastic collisions [16, 17]. Using this principle, optical tweezers use light to trap and manipulate particles. Within the description of ray optics, the gradient force pushes the particle towards the region of highest beam intensity while the scattering force acts upon the particle along the beam propagation direction. Balance of these forces is key to trapping the particle within the optical beam. Pioneered by Ashkin et al. in 1986 [18], they demonstrated the trapping of micrometer to nanometer sized dielectric particles in water. Subsequently, they extended the method to include biological particles such as cells [19]. This had led to a major revolution in single-molecule biophysics.

The trapping and manipulation of micrometer sized particles is well documented [20]. In contrast, the manipulation of nanometer sized particles is considered more challenging. The magnitude of force applied by optical beam decreases with the relative refractive index compared to surrounding medium and volume of the particle. This limits the size and type (e.g. dielectric vs. metallic) of particles that can be manipulated. Despite this challenge, there are ways to manipulate by improving on the set-up and working around particle resonances.

In general, the Rayleigh scattering coefficients are used to calculate the optical forces for particles smaller than $\sim \lambda/20$. For larger nanoparticles, the simple dipole model is insufficient and has to be generalised to include multi-pole effects. For this purpose, the Lorentz-Mie scattering theory is used [21, 22].

The challenges and opportunities in optical tweezers are slightly different for dielectric and metallic nanoparticles.

Manipulation of dielectric particles, metallic particles and molecules

Since the force applied to the particle is dependent on the particle's dielectric constant and relative refractive index, it is small for nanoparticles and would be even smaller for dielectric nanoparticles. Hence, a large laser power is required

to trap and manipulate dielectric nanoparticles [18]. The high power required may damage the particle instead. This problem can be overcome with counter propagating beams instead of a single beam used to trap dielectric nanoparticles [23]. In the counter-propagating geometry, the axial scattering force components are balanced from the opposing directions. Thus, the gradient force component dominates and can exceed that of single-beam tweezers [23].

Although manipulation of nanometric sized particles is difficult, having one dimension in the micrometer range can make things more tractable. For example, nanowires and carbon nanotubes have been manipulated [24, 25].

It was initially thought that it was impossible to trap metallic nanoparticles with optical tweezers [26], but they are now better understood with detailed studies [27, 28]. Metallic nanoparticles exhibit plasmonic resonance, which are resonant excitation of free electrons in the metal. Hence, if the wavelength of the trapping laser matches with the plasmon resonance wavelength, the trapping properties can be significantly altered. Metal nanoparticles can be trapped near the plasmonic resonance or far from it. One of the initial work by Svoboda et al. showed that they can trap 40 nm gold nanoparticles using infrared laser, which is far from the plasmon resonance. At this wavelength, the gold nanoparticles have a large relative refractive index, hence the gradient force is enhanced, enabling the particle to be trapped [29]. Trapping near the resonance affects the gradient force which changes with wavelength dependent polarisibility [30, 31]. In some cases, the polarisibility can become negative causing a repulsive gradient force. For example, Pelton et al. investigated gold nanorods with a longitudinal resonance of around 800 nm. They showed repulsion when the laser is tuned below the resonance wavelength and attraction when the laser is tuned above the resonance [32].

The trapping of gold nanoparticles has led to applications like non-contact scanning near field optical microscopy applications [33]. In another application, Prikulis et al studied the spectrum resonance shift and broadening when two 90 nm silver nanoparticles were brought close together [34].

However, one challenge of working with metallic nanoparticles is increased heating due to its high absorption, which would affect the usefulness in biological applications [35]. In order to minimise the heating effects, an alternative trapping geometry, which relies on the repulsive nature of the scattering force to repel the metal nanoparticles out of the high intensity beam region, may be considered [36].

Besides dielectric and metallic particles, optical tweezers have also been used to trap molecules. DNA has been trapped indirectly by attaching to micron-sized bead with suitable chemistry [37, 38]. Instead of applying forces directly on the molecule, the bead can be manipulated easily with single-beam tweezers. Direct trapping of molecules has also been achieved with higher trapping laser powers and optimising around the resonance of fluorescent labels [39–41].

A recent advancement on optical tweezers combines the effect of plasmonics and electrohydrodynamic flow to manipulate particles [42]. This technique is known as opto-thermo-electrohydrodynamic tweezers. In this technique, an array of plasmonic nanoholes is illuminated with light. Moreover, an AC electric field is applied to create an electrohydrodynamic potential that can rapidly trap sub-10 nm biomolecules. The particles are trapped a few micrometers away from the high-intensity laser focus, hence they experience negligible photothermal heating (Fig, 2.1). Thus, this method is particularly suitable for photo-sensitive particles.

Operation and construction

The main components of an optical tweezer set-up includes the objective—preferably with high numerical aperture—lasers, and lenses for beam delivery. Such a system can be readily implemented around a standard microscope with suitable imaging capabilities. Alternatively, it can be built with standard cage plates and other opto-mechanical components which can provide more flexibility.

In general, the nanoparticles to be trapped and manipulated are dispersed in aqueous solution. Practically, a liquid environment damps the particle motion, thus reducing the effects of Brownian motion which could hinder stable trapping and manipulation. With trapping of nanoparticles, imaging and visualising the particle

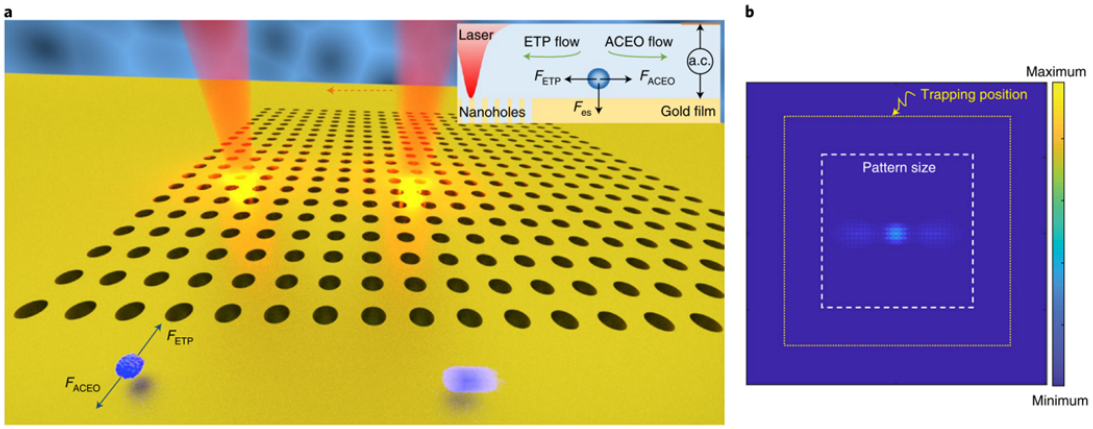


Figure 2.1: (a) Illustration of the operating mechanism of the opto-thermo-electrohydrodynamic tweezers system. By moving the laser on the plasmonic nanohole array, a single particle (blue sphere) is trapped away from the laser and follows the motion of the laser beam horizontally along the pattern edge. The inset shows the forces acting on a trapped particle when the laser and a.c. electric field is applied. ACEO, a.c. electro-osmotic flow; F_{ACEO} the drag force from the a.c. electro-osmotic flow; F_{ETP}, the drag force from the electrothermoplasmonic (ETP) flow; F_{es}, the particle–surface interaction force. (b) Electric field profile when a laser is focused at the centre of the nanohole array. At the trapping position, the electric field from the light is small enough to eliminate its influence on the trapped particle (adapted from [42]).

is an important consideration. There are fundamental limitations to direct imaging of nanoparticles with optical methods if they are smaller than the diffraction limit of visible light. Moreover, in some cases, there is little difference in refractive index between the particle and medium resulting in poor contrast. However, techniques have been developed to indirectly detect the nanoparticles.

Metallic particles usually have a larger refractive index compared to dielectric particles. Hence they are easier to image in brightfield illumination. The contrast and resolution in brightfield microscopy can be improved with Koehler illumination, where the light source is defocused in the sample plane, hence ensuring that the sample is uniformly illuminated by parallel light rays [43]. For small or transparent dielectric particles, differential interference contrast microscopy (DIC) will be a suitable technique [29]. Another imaging technique is darkfield microscopy which only collects the scattered light of particles against a dark background. This technique is particularly useful when particles exhibit certain plasmon or exciton resonances. However, it is challenging to combine dark field microscopy with

tweezing operation. Since the sample is imaged through the same objective lens used for trapping, the numerical aperture of the lens has to be smaller than the numerical aperture of the dark field condenser. High numerical aperture oil or water immersion lenses are preferred for stable trapping of nanoparticles. This limits the combination of possible objective lenses that can be used.

Fluorescent imaging can also be used if the particles or molecules can be tagged with fluorescent markers. However, its application is sometimes limited by the photobleaching effect. Another common method for visualising and imaging particles is the interferometric method made possible with the use of a quadrant photodiode. The interference pattern between the scattered light and the trapping beam is captured by a quadrant photodiode. The optical signal is converted into an electrical signal by the quadrant photodiode and can be used to determine the position of nanoparticles with nanometer precision [44].

2.2 Self-assembly of particles

One of the most common approaches in bottom-up assembly is via the self-assembly of particles. Self-assembly is used to describe the spontaneous process, which tends towards the system's thermodynamic minima, where nanoparticles arrange themselves into organised aggregates or structures. This process may be driven by electrostatics, surface chemistry, hydrophobic/hydrophilic forces and magnetic forces among others. Self-assembly techniques do not require complicated equipment, thus allowing low-cost mass fabrication. Moreover, it results in less material wastage and provides the possibility of three-dimensional assembly down to atomic feature sizes [45].

Langmuir-Blodgett technique

The Langmuir–Blodgett technique is one of the most conventional ways to fabricate nano-films with long range ordering of monolayers and multilayers efficiently [46, 47]. It involves pulling the substrate to be coated through a liquid-air interface where the monolayer is initially adsorbed [48]. Initially, amphiphilic molecules, with

a hydrophilic head and hydrophobic tail, were used to self-assemble into monolayers at the liquid-air interface. More recently, the technique has progressed to also fabricate monolayers of gold nanoparticles [49, 50] and quantum dots [51, 52].

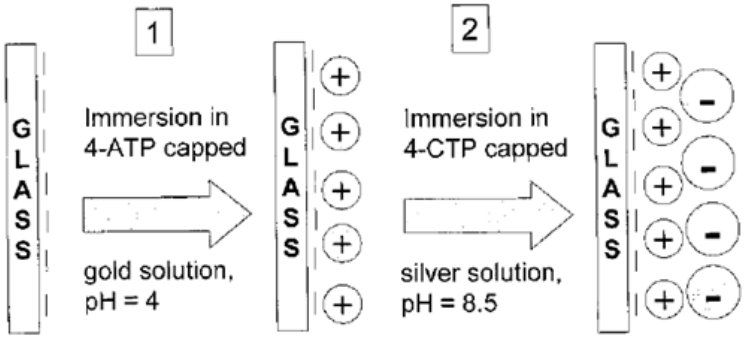
Electrostatic interactions

Another prevalent technique of self-assembly takes advantage of the electrostatic interactions between nanoparticles and molecules. It was pioneered by Iler in 1966 who constructed multilayer films consisting of both positively and negatively charged colloidal particles [53]. Since then, this approach has been widely used to fabricate functional materials with various building blocks such as metals, semiconductors, and organic dyes and particles [54–57].

An example of nanoparticles self-assembled in alternating multilayer fashion has been demonstrated by Kumar et al. [58]. They used gold nanoparticles with amine-terminated ligands (positively charged) and silver nanoparticles with carboxylic terminated ligands (negatively charged). The particles were assembled in a layer by layer fashion by alternately immersing a negatively charged glass substrate into the gold and silver colloidal solution with rinsing steps in between (Fig. 2.2). The terminated ligands are ionised to -NH3^{+} and -COO^{-} at a solution pH of 4.0 and 8.5 respectively.

Chemical interactions

In contast to electrostatic interactions, chemical bonding (e.g. covalent bonds) are more specific in fixing functional groups. This provides more directionality in terms of functional group directions, thus yielding more robust and permanent structures. Chemical self-assembly of nanoparticles primarily involve the use of chemisorption of monomers, polymers, metallic or semiconducting particles onto specific substrates. Spontaneous monolayers can be formed by immersing the substrate in a suitable solution. Typically, oxide-bearing substrates are immersed in organosilanes or metal substrates with alkanethiols [59]. Correspondingly, nanoparticles can have their surface functionalised with ligand molecules via chemisorption. These ligand molecules serve as stabilisers preventing agglomeration of particles in solution as



[a] Step 1: self-assembly of positively charged gold particles on negatively charged glass during immersion in 4-ATP-capped gold solution at pH = 4. Step 2: self-assembly of negatively charged silver particles on gold-coated glass during immersion in 4-CTP-capped silver solution at pH = 8.5.

Figure 2.2: Schematic showing the steps to form electrostatically assembled alternating layers of gold and silver colloidal particles (adapted from [58]).

well as providing a functional group which enables chemical interactions between these particles and monolayers with suitable functional groups. For example, TiO_2 nanoparticles have been attached to gold substrates with the use of bifunctional thiol molecules (i.e. HS–$(CH_2)_{10}$–COOH) [60]. One thiol group has affinity to gold and binds to the substrate while the carboxyl group binds covalently to the TiO_2 nanoparticles. Using a dithiol molecule, CdS quantum dots can also be assembled [61].

Biological molecules

In addition to chemical monolayers, biomolecules acting as linking molecules may be attached to surfaces and particles to facilitate self-assembly. Assembly mediated with biomolecules are mainly due to non-covalent interactions (e.g. hydrogen bonding and van der Waals attractions) and are highly selective. Short DNA molecules, or oligonucleotides, have highly specific binding properties. Two different batches of gold nanoparticle clusters have been self-assembled by attaching non-complentary oligonucleotides capped with thiol groups to the gold particles and adding a solution containing complementary oligonucleotides enabling self-assembly of the two batches of nanoparticles [62, 63]. This technique has also been extended

to the self-assembly of CdSe quantum dots, which enables the quantum dots to be used in biological applications as fluorescent probes [64, 65].

Surface forces

Ordered nanostrutures can also be driven simply by solvent evaporation. The dominating driving force is the reduction of interfacial energy. In an uncontrolled evaporating droplet, liquid from the edges evaporates and is replenished by liquid from the interior [66]. This capillary flow can carry nanoparticles in the solution towards the edge. This is known as the coffee-ring effect, named for the characteristic ring edge we observe in a coffee spill. Marangoni flow is another effect which tends to redistribute particles to the center of the droplet. Marangoni flow is induced by the presence of a surface tension gradient in liquid. A liquid with a high surface tension tends to pull more strongly on the surrounding liquid than one with a low surface tension. This surface tension gradient in a liquid can be caused by a concentration or temperature gradient. Therefore, particles can be made to assemble towards the edges or the center of the droplet by enhancing or diminishing the coffee-ring effect and Marangoni flow effect (e.g. surfactants reduce surface tension gradient).

With controlled solvent evaporation, periodic structures can be assembled [67–69]. If the thickness of the evaporating liquid is suitably controlled, particles can also be confined and assembled within the thin layer of liquid. CdSe quantum dots have been assembled in this way into two- and three-dimensional structures [70]. Similarly, structures of gold and silver nanoparticles were fabricated [71]. Multiple layers can also be achieved [72] using a similar method as Ref. [58].

Combination of techniques

Self-assembly techniques by itself is able to build large organised structures from individual building blocks of nanoparticles and molecules. However, it lacks the capability to precisely direct the location of assembly of these nanoparticles or molecules. Therefore, self-assembly is often used in conjunction with other top-down techniques such as lithography which ensures that the assembly occurs at the desired locations.

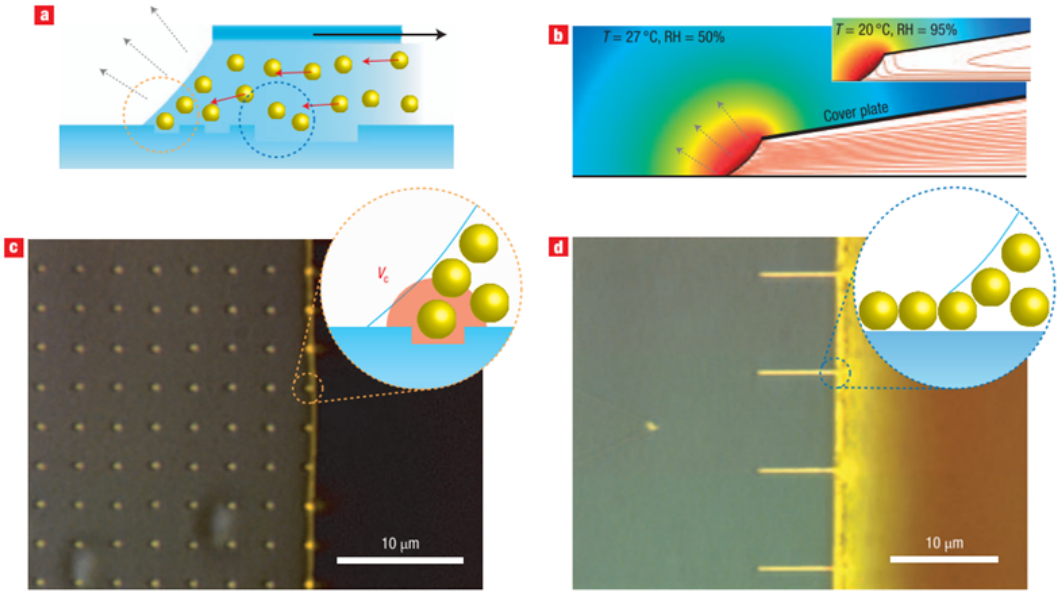


Figure 2.3: (a) The meniscus of a colloidal suspension containing 60 nm Au particles is moving over the patterned PDMS surface of a printing plate. (b) Simulation of the evaporation (colours indicate concentrations) and the streamlines (red lines) of the laminar flow that drags along particles towards the three-phase contact line, where they form an accumulation zone. The main panel is a simulation at a relative humidity (RH) of 50% and the inset for a RH of 95%. (c,d) The accumulation zone, visible in the micrographs as a bright yellow line, moves over the printing plate. Depending on the geometry they encounter, particles at the contact line form sparse patterns, for example, arrays (c) or dense arrangements such as lines (d) (adapted from [73]).

Combining e-beam lithography and evaporation driven self-assembly, Kraus et al. demonstrated single sub-100-nm particle printing with high placement accuracy [73]. The meniscus of a gold colloidal solution moves over a patterned Polydimethylsiloxane (PDMS) stamp (Fig. 2.3). The laminar flow drags along particles towards the three-phase contact line forming an accumulation zone. These particles can be trapped on the surface with suitable patterning of the PDMS substrate forming structures of nanoparticle arrays and lines. The PDMS can subsequently be used as a stamp to transfer these nanoparticles to another substrate [74, 75].

The positioning accuracy is often limited by the resolution of preceding patterning steps. However, Huang et al. showed that 20 nm gold particles can be trapped within a patterned circular region with a diameter of 130 nm patterned by e-

beam lithography [76]. The circular patterned area is functionalised with (3-Aminopropyl)trimethoxysilane (APTES) which confers a positive surface potential of 72 mV. The surrounding surfaces are coated with 6-Mercaptohexanoic acid (MHA) thus conferring a negative surface potential of 134 mV. This substrate is then immersed in a gold colloidal solution with nanoparticles that are capped with negatively charged citrate ions. The gold nanoparticles will thus be attracted towards the positvely charged area while the surrounding negatively charged regions further help to funnel the nanoparticles into the positively charged regions. Once attached, the negatively charged particle opposes additional particles from approaching, thus ensuring a single particle within each circular region.

Combining self-assembly techniques with scanning probe techniques provides a very powerful method to direct the assembly of molecules and particles. This technique will be introduced in more depth in Sec. 2.5.

2.3 External field driven manipulation

Electric field manipulation

Externally applied electrical and magnetic fields can be used to manipulate and direct the assembly of colloidal particles. A particle with a different dielectric index from its surrounding medium will become polarised in an electric field [77]. Moreover, mobile charges around the particle (e.g. electrostatic double layer) also respond to the electric field and hence contribute to the polarisation. The induced field around a polarised particle behaves like a dipole which can result in dipole-dipole interaction between particles. If this interaction is sufficiently strong to overcome Brownian motion, particles can assemble to form particle chains [78, 79]. Alternating current (AC) fields are preferred over direct current (DC) fields to avoid electroosmotic and electrochemical effects. By applying an AC electric field with coplanar electrodes, Lumsdon et al. have shown that micrometer-sized latex particles can be assembled into two-dimensinoal crystalline arrays (Fig. 2.4) [80]. A feature of field-induced assembly of particles is that the particle assembly is

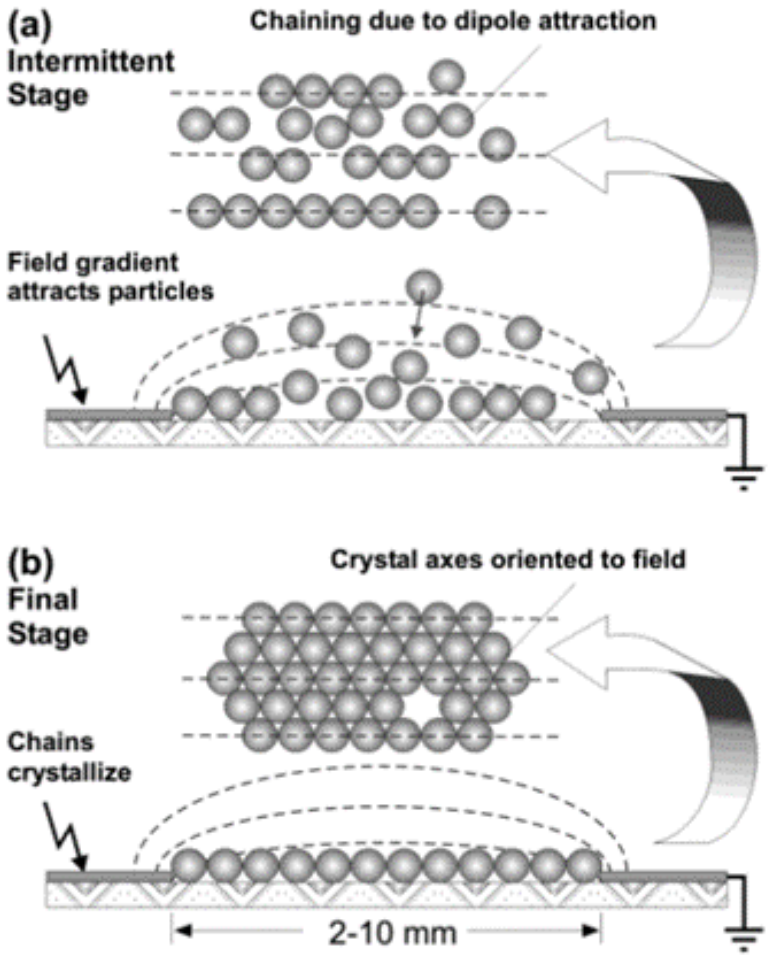


Figure 2.4: Schematics of the two-stage mechanism of crystallization deduced from the set of diffraction and microscopy data. (a) Immediately after the field is applied, the particles align in chains due to the induced dipole-dipole interactions. Simultaneously, the gradient-driven DEP force pulls the chains and particles toward the surface of the substrate between the electrodes. (b) The particle chains confined on the surface crystallize to form 2D hexagonal crystals aligned by the field (adapted from [80]).

reversible. Once the field is removed, the particles return to a disordered state, which would be useful for reconfigurable and switchable assemblies.

Besides dipolar interactions, AC electric fields can also generate electrodynamic flows which exerts a force onto particles, especially those close to the electrode surfaces. Particles have been manipulated into two-dimensional superlattices and other planar assemblies when the electric field is oriented normal to the plane [81, 82]. Moreover, local flows can also be driven by the rotation of particles due to the phase lag of polarisation with the applied electric field [83, 84].

The magnitude of dipolar interaction has to overcome thermal forces in order to drive the assembly of particles. Manipulating nanoparticles become challenging as the dipole-dipole interaction diminishes quickly with particle size. One of the smallest dielectric particles manipulated to grow three-dimensional colloidal crystals were 200 nm [85]. On the other hand, metallic particles experience a much stronger response to fields due to their higher dielectric constants. Hermanson et al. have shown that micrometer wires can be fabricated from 30-45 nm gold particles which are drawn towards the electrodes by dielectrophoresis in an AC electric field [86].

Moreover, the behaviour of particles in the electric field can also be tuned by controlling the surface properties. For example, particles with two or more surfaces with distinct physical properties can be fabricated. They are known as Janus particles. An example would be polymer latex spheres with a hemisphere coated with gold. In the presence of an AC field, these particles would assemble into a unique chain strucure with the metallic halves of neighbouring particles aligning with the direction of the applied electric field and the dielectric half aligning in the orthogonal direction [87].

If the gold is replaced with iron, the structure can be similarly tuned with an applied magnetic field [88].

Magnetic field manipulation

For magnetic particles, an obvious choice would be to use magnetic fields to manipulate them. Known as magnetic tweezers, they are capable of exerting about 200 pN on micron sized particles. The two most common methods of applying a magnetic field are with the use of permanent magnets [89] or electromagnets [90, 91]. The advantage of permanent magnets is that it can provide a constant force which is very useful for sensitive force-displacement measurements. On the other hand, electromagnets provide a faster response and both force and rotation can be controlled by controlling the current through the electromagnet [92]. However, there will be hysteresis as a function of current. The use of a high current also generates a lot of heat thus requiring the need of a cooling system. Without cooling,

the heat generated can lead to hysteresis and thus difficulty in maintaining the force required for manipulation. Electromagnets also generate less force as compared to permanent magnets [91]. However, it allows 3D control [90, 93]. In comparison to optical tweezers, magnetic tweezers do not have a stable 3D trapping potential. Hence, active control of the applied force is required. In contrast, magnetic tweezers is less damaging on sensitive biological samples (e.g. sample heating, photodamage). The scaling up and parallel processing are also easier to implement [94]. The disadvantage of magnetic tweezers is the inability to both manipulate and image like in the AFM. Most set-ups are instead paired with an optical based video detection which limits the size of particles that can be manipulated.

2.4 Microgrippers

The use of microgrippers is another tool we have at our disposal to manipulate micro and nano objects. Microgrippers often make use of two or more probes which act like minature fingers to grab and manipulate structures and are often paired with an optical microscope for visualisation and manipulation of micrometer sized objects [95, 96]. However, nano objects can be manipulated too. For example, microgrippers have been used to break off and transfer single carbon nanotubes for observation in TEM or SEM [97, 98]. There are currently a few designs of microgrippers (e.g. parallel beam [99, 100], rib cage [101], and nanotube [102]). Parallel beam designs are compact and have the ability to open and close as well as having force feedback [99]. However, it produces less force as compared to rib cage designs. Moreover, designs of the microgrippers can be made through optimisation algorithms [103, 104].

One of the most common techniques of actuation is electro-thermal. Such grippers are usually made of resistive material so that the beams of the grippers can be heated when a current is passed through them. This leads to bending of the beam which corresponds to opening or closing of the grippers depending on how the bias is applied. A common problem with microgrippers is adhesion of the nano object to the end-effector, making release difficult [105]. To overcome this, Zhang et al. have designed a three-pronged microgripper with a plunger for active release of the nano

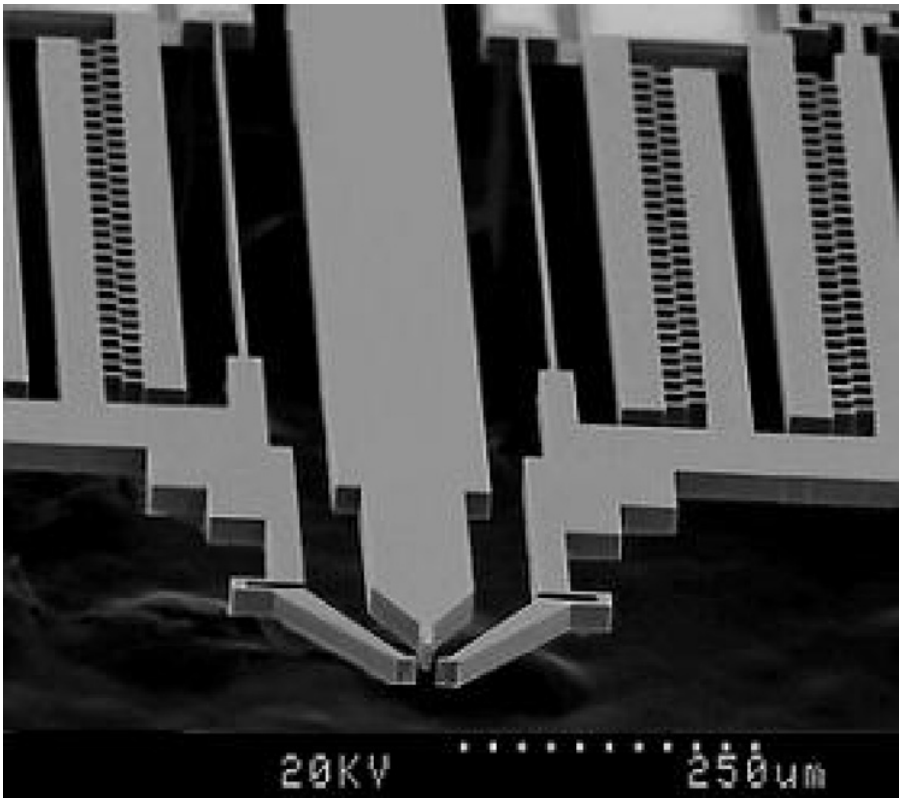


Figure 2.5: SEM image of a three-pronged microgripper capable of both grasping and active release of microobjects (adapted from [106]).

object (Fig. 2.5) [106]. Microgrippers seem to be a promising technique for pick-and-place processes. Attempts at automating the process were also made [106, 107]. However, most grippers are in the micrometer-scale fabricated using conventional lithography steps. Their relative large size and actuating voltages make it difficult for nanoscale work. Moreover, the reliance of van der Waals forces for gripping makes it difficult for gripping very small objects (<100 nm). Nanotube nanotweezers have been fabricated to overcome this problem. But it's fragility and inability to open after closing limits the reliability of pick-and-place processes at the nanoscale [102].

2.5 Scanning probe manipulation

Scanning probe microscopy techniques are able to form very high resolution images of surfaces on the order of fractions of a nanometer. In contrast to "seeing" the surface with photons or electrons like in optical and electron microscopy, scanning probe methods "feel" a surface by rastering a sharp probe over the surface. The gap

distance between the surface and the probe can be regulated using a feedback loop based on tunnelling current as in the STM, and probe-sample force in the AFM.

The AFM is one of the more popular tools for nanomanipulation due to its ability to manipulate a variety of materials (e.g. conducting/insulating nanoparticles, biological samples) in various environments (i.e. vacuum, air, liquid). The throughput of nanomanufacturing using an AFM is definitely lower than conventional lithography methods. However, it is able to pattern arbitrary patterns in 2D and even 3D. Moreover, it has in-situ imaging capabilities which enables the user to visualise their structure before, during, and after manipulation. This makes it a suitable and versatile nanomanufacturing tool for prototyping designs without the high initial costs of conventional lithography set ups. Atoms and nanoparticles may be manipulated (e.g. push/pull, pick-and-place) by a variety of forces (e.g. electrostatic, magnetic, van der Waals, covalent, capillary).

The work in this thesis focuses on the use of AFM to manipulate micro and nanometer sized particles due to its great precision and versatility. Hence, this section will generally focus on AFM techniques. I will also briefly describe the operating principles of the AFM which will help the reader better interpret the content of this thesis.

2.5.1 Operating principles

Figure 2.6 illustrates the basic components of an AFM. The AFM probe usually consists of a cantilever with a sharp tip at one end for imaging (tipless variants and tips with alternative geometry are available too!). The probe is typically scanned by piezo-electric elements, both in the approach direction (z) and the surface (x-y). Modern piezo electric elements can achieve a spatial resolution in the sub-nanometer range. This gives the AFM high resolution in the z-direction. Despite the high resolution of (x-y) positioning, the spatial resolution of images in the (x-y) direction is generally limited by the size and shape of the tip which typically tends to be of the order of a few nanometers.

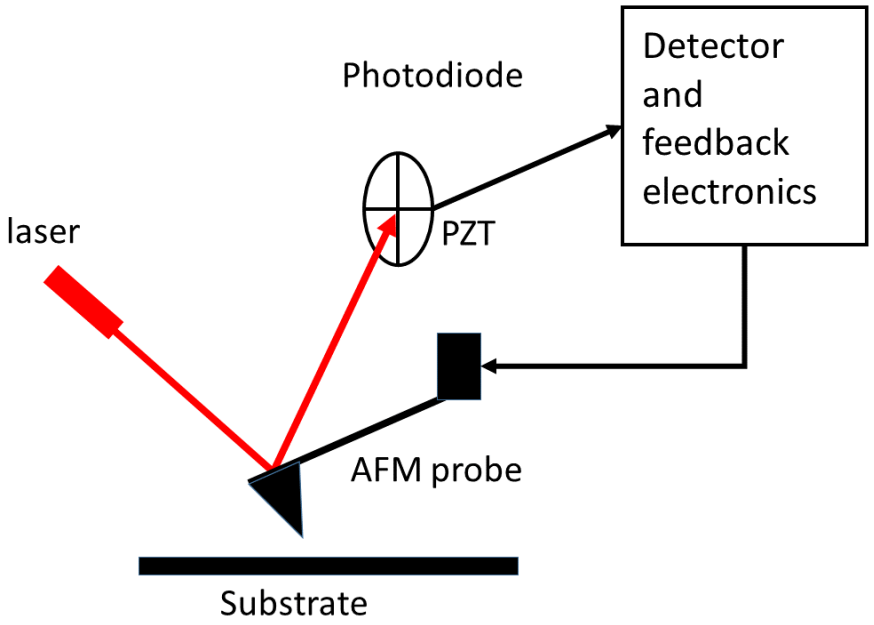


Figure 2.6: Schematic showing the basic components of an AFM.

Close to the substrate, the AFM tip experiences surface forces which may be repellent or attractive. The attractive forces are known as Van der Waals forces and are based on electron coupling interactions of close atoms or molecules [108]. The repulsive forces are attributed mostly to the Pauli exclusion principle, which is when atomic orbitals start to overlap [109]. These forces lead to a change in the cantilever position or resonance frequency, which can be detected. The most common detection means is through optical detection [110]. In the optical detection method, a laser beam is reflected off the free end of the cantilever into a photodetector which precisely registers the force dependent angle of the cantilever. Other less common detection techniques include optical interference [111], capacitive [112], piezoresistive [113] or tuning fork [114] readouts.

An AFM image is acquired by approaching and rastering a tip over a surface in a line by line fashion. The cantilever can be actuated statically (DC mode) or dynamically (AC mode). In the static mode, or contact mode, contact forces lead to a small deflection of the cantilever which is monitored. Contact mode often results in tip wear or sample damage as the tip scans across the surface. It is the common mode used to manipulate particles by pushing them around. In the dynamic modes,

the cantilever is mechanically excited near its resonance frequency. In this way, the tip can be set to intermittently contact the surface or avoid contact altogether in non-contact mode AFM. This leads to reduced tip and surface wear and is the most commonly used mode for high resolution imaging. We can monitor the amplitude and phase of the cantilever which changes as the tip approaches the surface. Small changes in the deflection in DC mode, or amplitude and phase in the AC mode maps the surface forces acting on the cantilever. This provides information such as topology, physical and chemical surface properties of the sample.

Besides simple rastering over a surface, modern AFMs can be programmed to move along a predetermined path. This provides the opportunity to use the tip as a manipulator to push or pull particles in whatever desired directions.

2.5.2 Pushing with the AFM tip

One of the earliest techniques of manipulating objects at the nanoscale is simply by pushing or pulling nanoparticles across a flat substrate [8, 115–119]. For micrometer sized objects, the alignment can be done optically. For example, the micromanipulation of 3D helical microswimmers have been manipulated using an AFM tip with optical alignment [120]. For smaller objects, the most common procedure in manipulation by pushing is by first imaging the surface to locate the particles. This is usually done in tapping mode so as to prevent damage to both the tip and surface. Next, the tip is positioned behind the selected particle before the operating mode is switched to contact mode. The tip is then moved to the desired position dragging the particle along with it. The AFM is subsequently switched to tapping mode and the region of interest is imaged again. This may be repeated to move other nanoparticles. The stiffness of the cantilever must be carefully chosen such that the same tip can be operated both in tapping and contact mode without damaging the substrate but providing enough force to manipulate the nanoparticle in contact mode. It was found that a sharp tip is best suited to push nanoparticles on a flat substrate as well as to avoid adhesion of the particle to the tip [117]. However, through repeated imaging and manipulation, the tip may be

contaminated and thus altering the tip shape. Changes in the tip shape will affect precise deposition of the nanoparticles [8]. Conversely, a blunt tip is better suited for picking up and retaining gold nanoparticles on the tip rather than for pushing [121]. The reliability and repeatability of push/pull mechanisms remain a challenge due to the lack of predictive capability of adhesion and friction at the nanoscale [122, 123]. Moreover, whether the particles slide or roll as they are being moved is also debated in the literature [124, 125]. Pushing techniques are usually limited to flat substrates but three-dimensional manipulations such as pushing a nanoparticle over a step have been demonstrated [116]. The process of "image-manipulate-image" is time consuming and affects the accuracy of manipulation due to tip contamination as well as drift. However, a recent work has shown how 15 nm gold nanoparticles can be moved and imaged simultaneously (Fig. 2.7) [126]. The nanoparticle is given an initial push in a random direction thus reducing its static friction. The AFM is then operated in tapping mode with a scanning rate above a threshold value which results in the nanoparticle moving perpendicular to the fast scanning axis. The manipulation can be stopped by reducing the scan rate below that threshold. The particle can thus be moved controllably and the motion is imaged in the form of "ghost image" taken in tapping mode AFM. Although there has been work on automating the process [127], most pushing manipulation is usually done manually with an operator controlling the process. Most of the difficulty in automation is due to the slow "image-manipulate-image" process. Improving real time feedback will enable easier automation of the process.

2.5.3 Electric field manipulation

As we have seen in Sec. 2.3, electric fields can be used to manipulate particles into networks and structures. We can take advantage of the positioning precision of scanning probe techniques to direct the assembly of particles. Nanoparticles may be manipulated in either alternating current (AC) or direct current (DC) electric fields. AC fields are usually applied in order to make use of dielectrophoresis (DEP). Particles can move due to a non-uniformed electric field and the presence of induced

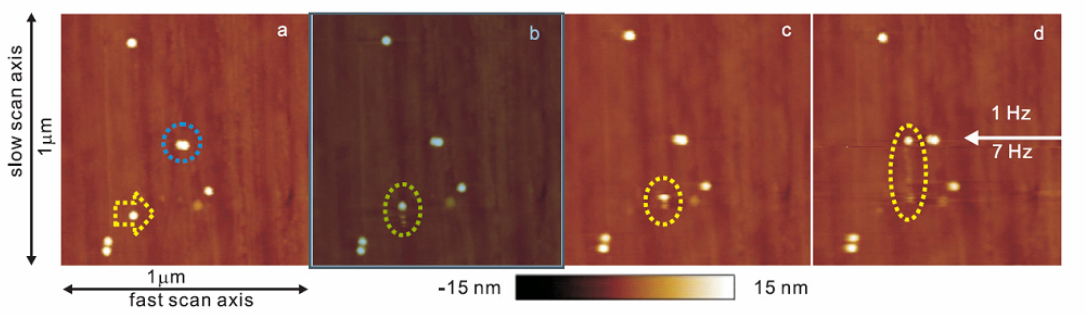


Figure 2.7: Nanomanipulation with visual guidance. (a) An image taken at 1 Hz before any manipulation. The nanoparticle enclosed in the arrow mark was kicked to the right using the standard method. Following the kicking event, images were taken at a scanning speed of (b) 1 Hz and (c) 5 Hz. In both cases, the nanoparticle enclosed in the circles moved a short distance but stopped before reaching the target position. (d) Controlled manipulation was achieved at a higher scanning rate of 7 Hz. The scanning speed was abruptly reduced from 7 to 1 Hz once the target position was reached. Ghost images behind the moving particle provide a useful and clear visual guidance during the manipulation (adapted from [126]).

charges. An advantage of using DEP forces is that the object to be manipulated does not have to be conducting. Moreover, particles can be attracted, retained or repelled by adjusting the voltage frequency switching between either positive or negative DEP. Using a sharp AFM probe, single clusters of nanoparticles can be trapped and patterned on indium tin oxide (ITO) substrates by the use of DEP forces [128]. Brown et al. have demonstrated pick-and-place nanoassembly of 500 nm silica microspheres using DEP [129]. They used a custom made coaxial AFM tip to trap a single microsphere at the apex when an AC field is applied. To release the particle, the field is turned off and the microsphere is brought into contact with the substrate and scrapped off. An improvement in the form of a triaxial probe was subsequently proposed and made [130, 131]. The triaxial probe is able to trap a 100 nm polystyrene sphere in the zero of the electric field profile which is away from the probe tip (Fig. 4.4). This non-contact method of trapping prevents the particle from being stuck to the AFM tip due to van der Waals forces as well as preventing clustering. Release of the particle was achieved by simply changing the voltage frequency to switch to negative DEP which repels the particles.

A DC bias can also be applied to attract and detach nanoparticles from an AFM tip [132]. However, the DC potential bends the AFM probe possibly resulting

in irreversible collapse of the probe into the substrate. Therefore, the user must take into consideration the magnitude of the potential applied and the attractive electrostatic forces between the tip and substrate when using DC manipulation. If the potential is too large, the tip may crash into the sample. However if the potential is too small, the nanoparticle will not be released from the tip due to attractive van der Waals forces. Toset et al. have numerically calculated the balance between tip-sample distance and potential applied such that the nanoparticle may be released without the tip collapsing into the substrate [133]. Cheng et al. have experimentally demonstrated that gold nanoparticles can be picked up by an AFM tip by first laterally manipulating the nanoparticle before applying a bias greater than 4 V between the tip and the gold nanoparticle [134]. The lateral manipulation is helpful for releasing the nanoparticle from binding to the substrate or other contaminants. However, reliability in their technique is dependent on the conductive coating of the probe tip which tends to wear off after repeated uses. The mechanism behind picking up of small nanoparticles ($<$ 4 nm) is also not clear [135]. Possible mechanisms proposed are evaporation and electromigration and deposition of the gold nanoparticle.

High voltage electrostatic forces can also be used to release particles that are stuck to the AFM probe due to adhesive forces (e.g. van der Waals, capillary) [136]. However, this technique requires the AFM probe, nanoparticle and substrate to be conductive. Lifting and sorting of positively and negatively charged nanoparticles have also been demonstrated by controlling the tip bias from -6 V to +6 V [137]. Another mechanism which enables pick-and-place assembly is electro-enhanced capillary forces [138]. It was demonstrated that a water bridge can be induced between a conductive AFM tip and a 25 nm metallic nanoparticle by application of a voltage pulse (Fig. 2.9). This exerts a capillary force that is large enough to detach the particle from the substrate. Subsequently, the particle may be placed at a desired location simply by contacting the substrate. This is an impressive result of pick-and-place nanomanufacturing in ambient conditions using a simple

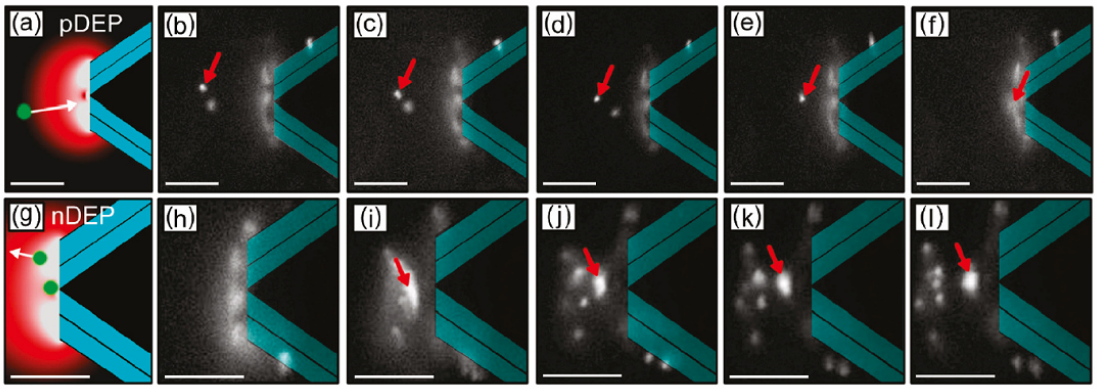


Figure 2.8: Attracting particles with positive DEP (pDEP) and repelling and holding them with negative DEP (nDEP). All scale bars are 5 μm. (a) Schematic of a particle being drawn into the field maxima with pDEP. (b-f) A time sequence of fluorescence images depicting the bead marked with the red arrow being drawn into the tip with pDEP. The schematic cross section is overlaid in the approximate position of the triaxial probe as a guide to the eye. (g) Schematic of one particle being repelled from the probe by nDEP and another being held in the nDEP trap. (h-l) A time sequence of fluorescence images depicting the triaxial probe repelling beads with nDEP. The majority of the beads are pushed back into suspension while the beads marked with the red arrow are held in the nDEP trap (adapted from [131]).

mechanism. However, due to the reliance of the water bridge for pick-and-place, it is crucial that the ambient humidity is well controlled within a certain range.

More recently, Lyu et al. have remarkably shown the pick and place of sub-50 nm fluorescent particles [139]. They overcome the "sticky fingers" problem by coating the AFM tip with a thin layer of fluorocarbon film. They are able to adjust this "stickiness" value by applying an external DC voltage to pick up particles and triangular pulses to place them. This appears to be a very promising technique if the method can be extended to a variety of particles and substrates.

2.5.4 Chemical functionalisation of the AFM tip

Self-assembly is a relatively quick and easy method to uniformly attach nanoparticles to a substrate. Hence, an AFM tip can be coated with a monolayer with a chemical affinity towards the nanoparticle to be manipulated. This can result in picking up nanoparticles by using an AFM tip. Vakarelski et al. have demonstrated that by coating a silicon nitrate AFM tip with a monolayer of (3-Mercaptopropyl)trimethoxysilane (MPS), gold nanoparticles were immobilised by

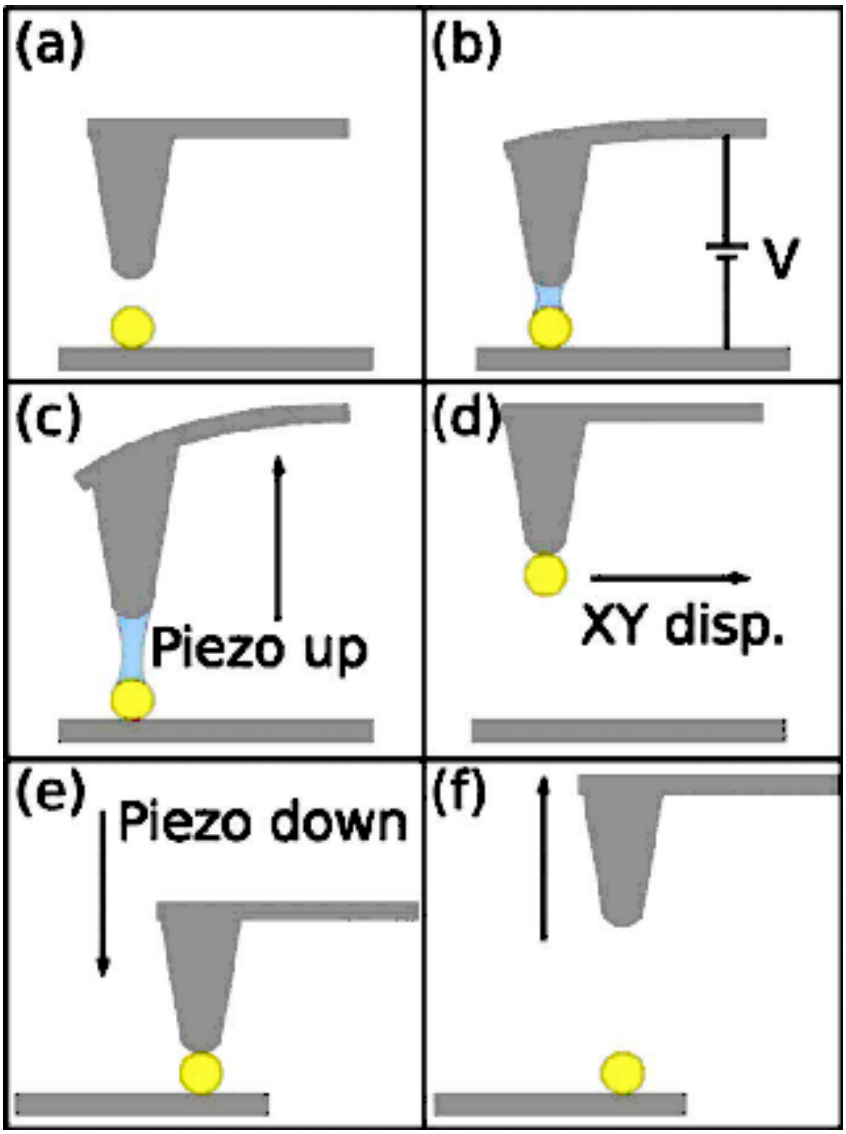


Figure 2.9: A schematic representation of the electro-enhanced capillary nanomanipulation technique. (a) Initial situation with the probe at some distance from the nanoparticle; (b) formation and growth of the water bridge by the application of a voltage pulse; (c) probe withdrawal and capillary force pulling the nanoparticle upwards; (d) nanoparticle detachment and displacement while attached to the probe; (e) release of the nanoparticle by contact with the substrate; (f) piezoretracted and nanoparticle in the final situation (adapted from [138]).

the thiol tail groups of the monolayer [140, 141]. The nanoparticle attachment can be made more specific to the tip apex by first coating the tip with a passivation monolayer (Fig. 2.10). This layer can be removed at the apex by rastering over a clean silica layer thus exposing a fresh oxide surface for MPS to be deposited. In this way, gold nanoparticles can be specifically attracted to the apex of the AFM tip. Vakarelski et al. did not discuss possible release mechanisms. Instead, they use the nanoparticle tip to measure forces between the nanoparticle tip and a mica surface in an aqueous electrolyte solution [140] and to function as a robust nanosurgical needle for direct injection of nanoparticles into cells [142]. As an alternative to chemical functionalisation, epoxy glue have also been used to attach gold nanoparticles to the AFM tip [143]. However, this method has poor control over the nanoparticles resulting in a cluster of nanoparticles at the tip. Chemical functionalising of an AFM tip can prove to be a versatile and specific way of picking up desired nanoparticles. This technique can be extended to almost any kind of nanoparticle if the surface chemistry of the nanoparticle has a chemical affinity towards some surface-confined functional group. Examples include metallic nanoparticles (e.g. Ag, Au) that can be attached to thiol or amino organosilanes [144], and polystyrene nanoparticles binding to amine-terminated monolayers [145]. However, in-situ functionalisation in an AFM as well as methods of detaching these particles from the functionalised surface still needs more exploration for true pick-and-place applications.

2.5.5 Dip-Pen technique and its derivatives

Dip-pen nanolithography

It was discovered in the 1990s that AFM tips "contaminated" with molecules capable of forming self-assembled monolayers (SAMs) were depositing SAMs when the "contaminated" tip was scanned over clean areas of the substrate [146, 147]. This was then developed into a nanodeposition technique in 1999 termed "Dip-Pen Nanolithography" (DPN) by Mirkin's group [148]. The basic idea of DPN is coating an AFM tip with a desired material and depositing it over a substrate through the meniscus formed between the tip and the substrate, similar to the

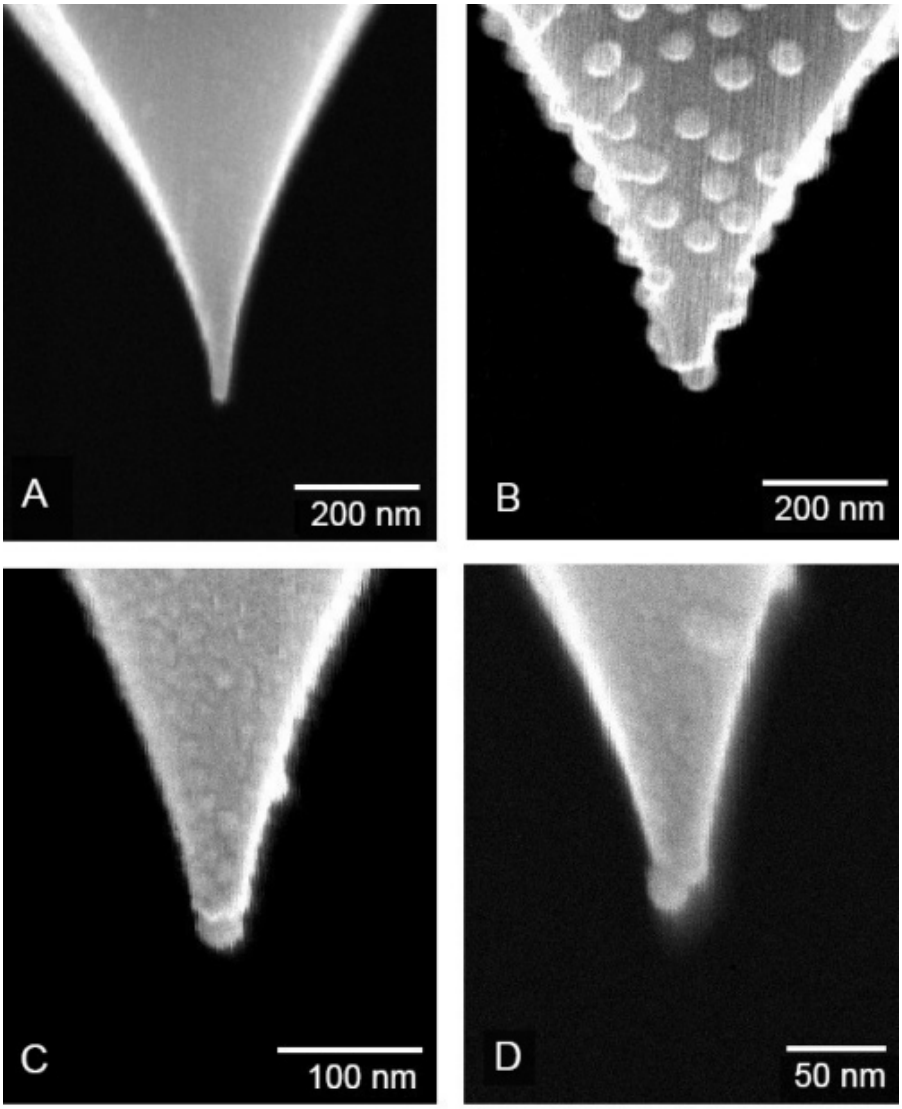


Figure 2.10: SEM images showing (a) an unmodified silicon nitride tip (Olympus TR400PSA) and (b) a tip coated with gold nanoparticles, which have an average size of 40 nm. Images of the tips modified with passive and active layers terminated with single gold nanoparticles with approximate sizes of 25 and 14 nm are shown in (c) and (d), respectively. In all cases, the tips were sputtered with a gold coating of about 2 nm to enhance the quality of the image (adapted from [141]).

way letters are written with a quill pen dipped in ink. Although initially used to deposit SAMs, DPN has been developed to deposit a variety of inks (e.g. small molecules, DNA, polymers, biomolecules, colloidal nanoparticles, metal ions, etc.) onto various substrates with sub-50 nm resolution.

A derivative of DPN is the electrochemical DPN which is able to directly fabricate metal and semiconductor nanostructures [149]. In this technique, the meniscus formed between the tip and substrate functions as an electrochemical cell, transporting and reducing metal salts to be deposited as metal on the substrate. Another derivative is the thermal DPN where the tip can be heated to melt and deposit solid organic inks on a surface [150].

Although DPN has many derivatives and the capabilities to pattern a wide variety of inks, we focus mainly on the techniques that can manipulate particles.

DPN is capable of creating a chemical template which can subsequently be used to assemble nanoparticles. For example, DPN has been used to pattern 16-thiohexadecanoic acid on a gold surface followed by assembly of amine and amidine-modified particles [151]. Moreover, DNA can be used to assembly gold nanoparticles functionalised with the complementary oligonucleotides [152].

It is also capable of directly placing nanoparticles. For example Ben Ali et al. inked an AFM tip with a concentrated solution of alkanethiol-capped 5 nm gold colloids [153]. They were able to deposit the particles in clusters of 50-200 nm by controlling the applied contact force.

Fountain pen approaches

A clear limitation of the DPN technique is that only small quantities of "ink" can be deposited before needing to refill it. Furthermore, evaporation of ink from the tip due to the lack of a sealed reservoir limits the amount of ink that can be used and deposited. Similar to how our writing tools have evolved from quill to fountain pens, so too has the nano/micro patterning techniques. The fountain pen approach to nanoscale patterning consists of probes with reservoirs

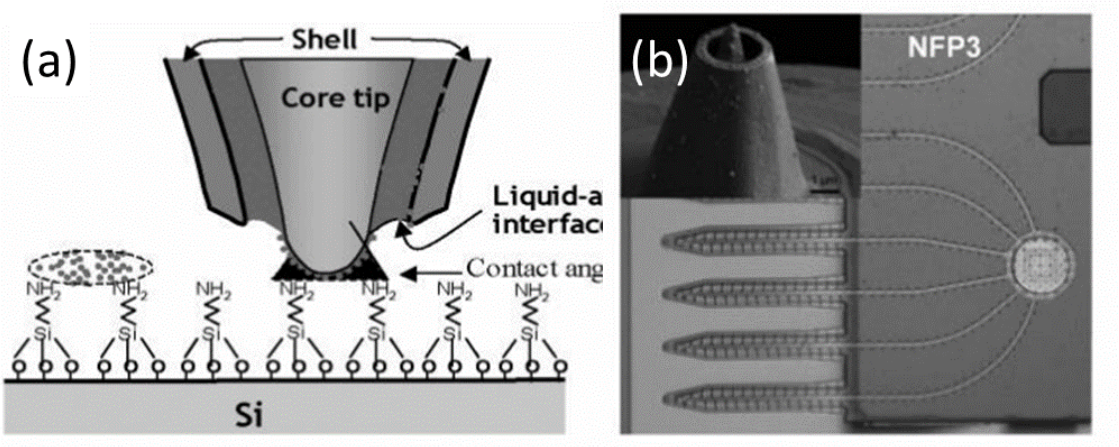


Figure 2.11: (a) Schematic of Au nanoparticle delivery by the nanofountain probe, (b) Optical image of nanofountain pen cantilevers, inset: aperture of probe tip (adapted from [160]).

to hold the ink which can be delivered to nanoscale apertures for meniscus guided deposition of a multitude of inks.

The early fountain pen approaches used micropipettes, similar to scanning ion microscopy, to pattern dots and lines of copper with line widths of 1.8 μm. Microchannels can also be fabricated within AFM tips to transport ink from an adjacent reservoir to the tip [154, 155]. These tips are capable of delivering liquid with resolution down to 70 nm [156].

Initial work on the fountain pen primarily focused on patterning structures in 2D. For example, 2D structures such as continuous gold nanoparticle lines [154, 157] as well as polymeric dots [158] and lenses [159] have been patterned. The first demonstration of writing of gold nanoparticle ink was from a glass capillary followed by laser annealing [157]. They have achieved linewidths of 1-9 μm. Better resolution can be achieved with microchanneled AFM tips (Fig. 2.11) [160]. Aqueous gold colloid solutions can be delivered with diameters less than 200 nm and height corresponding to the dimensions of the nanoparticles (15-20 nm) [160]. The size of the deposition was determined by the contact time with the substrate. The deposited gold nanoparticles are stablised by electrostatic interactions with amine-terminated functionalised substrates.

Moreover, a mixture of inorganic ZnO nanoparticles and organic PEDOT:PSS is used to make nanowires with ambipolar photoresponse using the fountain pen method [161]. An ambipolar photodetector changes the sign of the photoconductance depending on the wavelength of light it is exposed to. Yoo et al. showed that they could adjust the photoconducting properties of the nanowire by controlling the concentration of ZnO nanoparticles (0-30% weight) [161]. PbS quantum dots have also been mixed with polymeric ink and deposited using fountain pen approach to allow for a broader photoresponse spanning into the near IR range [162]. Organic particle inks such as carbon nanoparticles, or better known as nanodiamonds, can also be directly patterned with the volcano-shaped AFM tip [154]. The size feature was found to be dependent to the contact time between the tip and the surface. In particular, 90-350 nm diameter spots of nanodiamonds could be patterned with a contact time of 1.5-5 s.

The technique is also capable of fabricating 3D structures. By controlling humidity and allowing rapid solvent evaporation at the meniscus, ink components can be locally deposited. Suryavanshi et al. used this method to deposit 3D structures of $CuSO_4$ [163]. Other inks such as glucose, KOH and CdSe/ZnS core shell quantum dots have also been used [164].

The final structure features of the deposited ink depends on various factors (e.g. size and shape of the meniscus, substrate surface properties, solvent properties, etc.). The geometry of the meniscus is determined by the respective contact angles at the tip and substrate. The size and shape of the meniscus can be controlled by tuning the hydrophilicity of the substrate. For example, when a hydrophilic tip is used on a hydrophilic substrate, nearly all the liquid flows from the tip to create a large droplet meniscus [165]. Conversely, a smaller meniscus, thereby achieving smaller features sizes, is possible when using a hydrophobic tip on a hydrophobic substrate [166]. Another consideration is the contact time between the tip and substrate, where shorter contact times may result in less material deposition [165, 167].

Pinning effects can also greatly affect the resulting features especially for nanoparticle inks. Pinning can be described as the sticking of a moving liquid-solid-

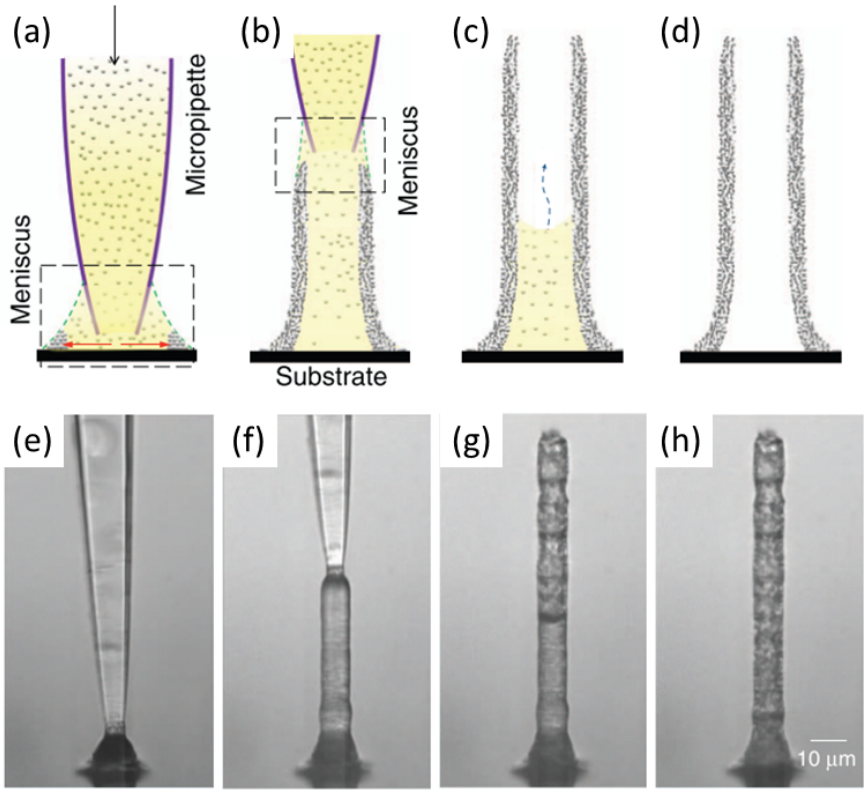


Figure 2.12: (a-d) Schematics of the fabrication procedure of a polymer composite microtube. (a) Deposition of PMMA/PPy NPs at the edge of a meniscus due to outward flow in a fast evaporating solvent, forming a ring-like deposit. (b) As the micropipette is slowly pulled up (< 25 μm/s) away from the substrate, the outward liquid flow continually accumulates the NPs on the ring-like deposit, forming a microtube. Here the accumulation is confined within the meniscus that is guided upward by the micropipette. (c) Once exposed to the air by taking away the micropipette from the microtube, the remanent solution inside the microtube rapidly evaporates, finally leaving a hollow microtube in (d). The four sequential optical images, (e-h), taken in real-time during the abrication, show the corresponding processes of (a-d), respectively (adapted from [169]).

gas interface. With nanoparticle inks, accumulation of particles can occur at this contact line interface [168]. This effect can be taken advantage of to form 3D hollow structures as demonstrated by Won et al. [169]. They used micropipettes (4.4-25 μm diameter) filled with polymeric nanoparticles. Due to fast solvent evaporation and outward liquid flow, a ring of deposited nanoparticles is formed in the meniscus. Continuous accumulation of nanoparticles is then achieved by guiding the meniscus upwards thereby forming a free-standing hollow microtube (Fig. 2.12).

2.6 Current challenges and opportunities with particle manipulation

From the above sections, we have familiarised ourselves with the techniques available for particle manipulation across the various length scales. No single technique is considered superior or inferior to another. Understanding each of their advantages and limitations would be useful in deciding which technique is suitable given a specific substrate or application and its requirements. This section aims to inform the reader on the general considerations when deciding or developing a particle manipulation technique for use.

Particle size and physical properties

The particle to be manipulated is often determined by the application requirements. For example the material and size of a particle is important for optical resonance effects which depends on the design of the optical device. Techniques such as self-assembly would generally work across length scales. At the atomic scale, our best instrument would be the STM. At the micrometer scale, various techniques such as optical manipulation and microgrippers are suitable. In optical manipulation methods, the dielectric constant and particle size determines the magntitude of trapping force that can be applied to the particle. For this reason, optical methods are most commonly used for micron-sized objects. However, as we have seen, modifications to the set-up and trapping regions can be made to manipulate particles down to hundreds of nanometers (e.g. Ref.[42]). However, there are few techniques available to manipulate nanometer sized particles, especially in ambient conditions.

Precision

Techniques such as self-assembly are able to manipulate a large number of particles into desired patterns, usually pre-defined by a top-down method such as e-beam lithography. Optical tweezers are able to trap nanoparticles, but manipulating them in all three spatial dimensions relative to a substrate can be challenging due to set-up limitations such as alignment of the beam and lenses, etc. Probe based

methods have very high precision in all three spatial dimensions due to highly precise piezo-electric motors. The fountain pen approach is able to place clusters of nanoparticles with a resolution of 70 nm [156]. However, few techniques are available to pick and place single nanoparticles. Moreover, precise placement onto a substrate requires some kind of imaging capability to locate and deposit the particle precisely at the desired location.

In-situ imaging

In order to align particles onto a substrate, some kind of visualisation of the process is required. The user should be able to know whether they have picked up or released particles and also be able to locate where on the substrate they have placed the particles. For example, microgrippers are often paired with an optical microscope or SEM to visualise the manipulation process. Optical tweezers rely on optical methods of visualisation which is diffraction limited. Despite this, techniques have been developed to image the particles indirectly by relying on specific particle properties like dielectric constant contrast and resonances. Nonetheless, it is still a challenge to directly imaging nanoparticles that are in close proximity to each other. Probe-based techniques are able to image by rastering the tip over the surface. With sharp tips, a spatial resoltuion of sub-10nm is easily achieved. However, the manipulation and imaging is often done sequentially and not real time.

Environment

The environment in which the manipulation is conducted in is another consideration. Optical tweezers are often conducted in a colloidal solution. Depending on the size of particles, microgrippers can be operated in air for larger particles and in a vacuum SEM chamber in order to visualise the smaller nano objects. Self-assembly techniques often involved submerging the substrate into a SAM or colloidal solution. Probe-based methods can be conducted both in air, liquid or vacuum conditions. Manipulation in a liquid would be the ideal environment for experiments in biochemistry and medicine. However, patterning in air would be preferred in some situations where submerging the substrate in a liquid would damage it. For

example, particles to be manipulated onto a substrate with electronics. Nanoparticle manipulation in air is still very challenging to achieve due to the "sticky hands" problem. The manipulation technique will have to overcome the capillary forces that is dominant for small particles in air. Moreover, it is noteworthy that when manipulating particles in liquids, we have to take into consideration how the particles are anchored to the substrate as they could be washed away together with the liquid when drying the substrate.

Throughput

Throughput is an important consideration for scaling up and mass production of devices. However, it is less important for proof-of-concept designs or niche applications. Directed self-assembly techniques would have the highest throughput and is also capable of patterning over a large area. Optical tweezers often have low throughput. However, multiple laser beams may be used but at the cost of more complicated set-ups and higher power consumption [170]. Probe based techniques can be scaled up with parallel probes [171].

2.7 Chapter summary

We have seen the common techniques available for us to manipulate particles into 2D and even 3D structures on substrates. More importantly, we see that a combination of techniques provides a much more powerful technique to manipulate particles. There is an opportunity for developing a technique that is capable of manipulating particles, ideally single nanoparticles, in air using the AFM. Such a technique will enable many new applications in nanoengineering.

3

Coating of self-assembled monolayers

Contents

3.1 Introduction 39
3.2 Aims of chapter 40
3.3 Self-assembly of nanoparticles on molecular monolayers 40
3.3.1 Materials and methods 41
3.3.2 Gold nanoparticles and their affinity to SAMs 42
3.3.3 AFM tips 45
3.4 Chapter Summary 47

3.1 Introduction

The AFM is a useful tool for manipulating micro and nano objects due to its ability to topographically visualise the substrate which enables the user to target a specific location with nanometer precision. Therefore, it would be sensible to modify the AFM tip to re-purpose it as a nanoscale manipulator. In this chapter, we explore the use of self-assembled monolayers (SAM) on AFM tips to attract gold nanoparticles. Gold nanoparticles are chosen due to: (i) the ease of functionalisation and well known binding to SAMs [172], (ii) wide applications in biology [173], nanoelectronics [174] and photonics [175], among others.

3.2 Aims of chapter

- Demonstrate the use of SAMs to pick up gold nanoparticles on an AFM tip apex.
- Briefly discuss the possibility of using a combination of monolayers to further localise picking up of gold nanoparticles on the tip apex.

3.3 Self-assembly of nanoparticles on molecular monolayers

Self-assembled monolayers (SAM) of organic molecules are formed on surfaces in an ordered layer by adsorption [176]. Single nanoparticle precision placement have been achieved on self-assembled monolayers on a planar substrate [76]. Here we explore how gold nanoparticles are attracted to various monolayers and whether we can use monolayers to achieve single nanoparticle pick up on an AFM tip. The monolayers used in this study are: (3-Aminopropyl)triethoxysilane (APTES), 1H,1H,2H,2H-Perfluorooctyltriethoxysilane (POTS), trimethoxy(octadecyl)silane (TMODS) and (3-Mercaptopropyl)trimethoxysilane (MPS). Their chemical structures are shown in Fig. 3.1(a – d) respectively. In general, these molecules can undergo silanization with silicon oxide surfaces. The silicon oxide surface is first activated by exposing surface hydroxyl (-OH) groups after a piranha cleaning process. These hydroxyl groups can displace the alkoxy groups (R-O) on the silane, thus forming covalent -Si-O-Si- bonds. In solution, amino-terminated SAMs such as APTES are known to form ammonium ($-NH_3^+$) ions on the substrate surface [177, 178]. This can electrostatically attract citrate stabilised (COO^-) gold nanoparticles (Fig. 3.1(e))[172]. The thiol groups in MPS are able to form covalent bonds with gold nanoparticles (AuNP) [179]. Fluorinated SAMs (e.g. POTS) and long chain alkylsilanes (e.g. TMODS) are known to impart hydrophobicity to substrates [180, 181]. POTS is more hydrophobic compared to TMODS due to the long chain of fluorocarbons [182]. Therefore, aqueous gold nanoparticle solution will be inhibited from assembling on the TMODS and POTS surfaces.

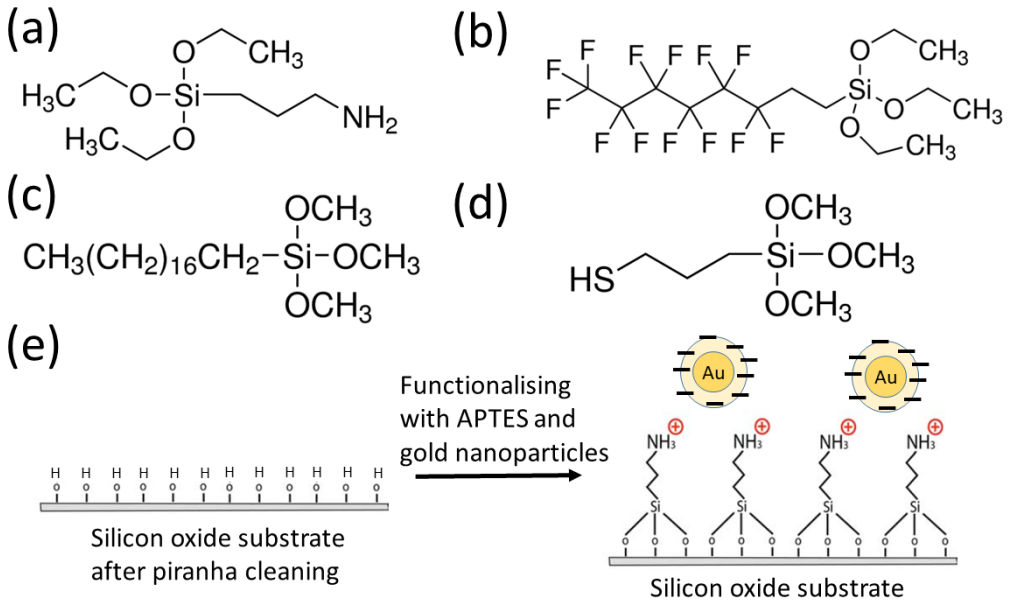


Figure 3.1: The chemical structures of (a) APTES, (b) POTS, (c) TMODS and (d) MPS. (e) Schematic showing a silicon oxide substrate after treatment with piranha solution to generate hydroxyl groups, followed by silanization with APTES. The positively charged amine groups electrostatically attracts negatively charged citrate-capped gold nanoparticles in solution.

3.3.1 Materials and methods

Preparing monolayer solution and functionalising substrates

The monolayers studied are 99% APTES, 98% POTS, 90% TMODS and 95% MPS [1]. Silicon oxide substrates were sonicated in acetone, isopropyl alcohol (IPA) and deionised (DI) water for 5 minutes each and dried under a stream of nitrogen gas. The dried substrates were immersed in freshly prepared piranha solution (30% H_2O_2 and 97.5% H_2SO_4 [1], 1:3) for 30 minutes at 100^{o}C. After cleaning and allowing the piranha solution to cool, the substrates were rinsed in deionised water twice. Subsequently, the cleaned substrates were immersed in 10 mM solution of monolayers dissolved in anhydrous toluene overnight (usually 12h) at room temperature. After overnight assembly, excess physisorbed molecules are rinsed off by sonication in acetone, IPA and DI water for 10 minutes each. 20 nm aqueous gold nanoparticles capped with citrate ligands (BBI solutions) were assembled on the functionalised substrates for 10 minutes. Subsequently, the substrates were

[1]The percentages refer to purity assay percentage given by the supplier, Sigma-Aldrich [183]

rinsed in DI water and IPA before drying in a stream of nitrogen gas. All chemicals were obtained from Sigma-Aldrich.

Cleaning and functionalising of AFM tips were done with similar procedures above. The tips were held with a custom made teflon holder which makes it convenient to process multiple AFM tips at once. It is important to ensure that the holder is kept clean to prevent contamination and destabilising of AuNP solution during assembly.

Phase transfer of gold nanoparticles from aqueous solution to hexane

Gold colloidal solution in hexane is prepared by a phase transfer method [184]. Hexane (20 ml) and sodium oleate (20 mg) was added to the aqueous gold nanoparticle colloidal solution (20 ml). The mixture was emulsified by vigorous stirring for 1 h. Subsequently, magnesium chloride (0.125 g in 3 ml of water) was added to the emulsion while stirring. The mixture was then left to stand at room temperature for 4 h which results in separation to two distinct liquid layers. The bottom layer is a transparent aqueous solution while the top layer is a dark red colour of gold nanoparticle colloidal solution in hexane.

3.3.2 Gold nanoparticles and their affinity to SAMs

We first test the effectiveness of these monolayers on planar surfaces to determine how gold nanoparticles interact with them. These experiments also serve as a baseline to compare to when using SAMs to assemble AuNP on a high aspect ratio structure like an AFM tip. Figure 3.2 shows how well the AuNP assemble on (a) APTES, (b) TMODS, (c) POTS, and (d) MPS.

We observe a dense and uniform layer formed on APTES due to the electrostatic forces between the negatively charged citrate ligand on the gold nanoparticles and the positively charged amino group of the APTES [185]. There is little to no assembly observed on TMODS and POTS as they cause the surface to become hydrophobic, with POTS being more hydrophobic than TMODS. Correspondingly, we notice slightly more assembly on TMODS compared to POTS. The presence

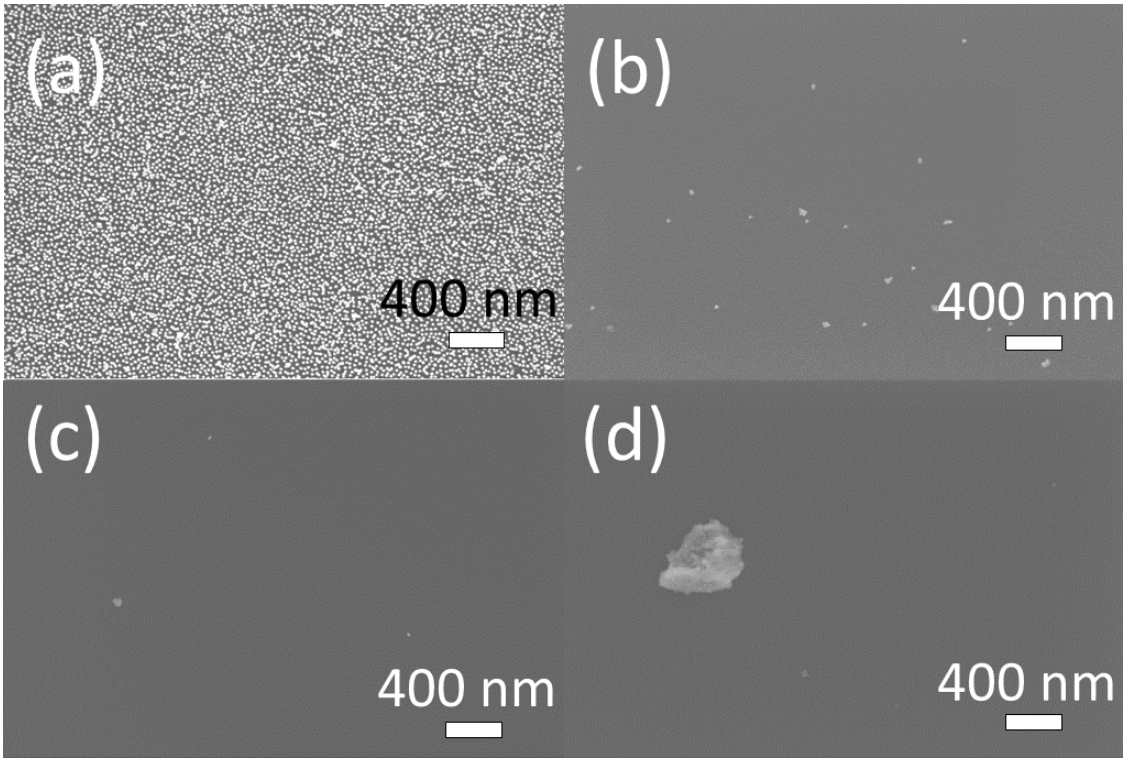


Figure 3.2: SEM images of gold nanoparticles assembled on (a) APTES, (b) TMODS, (c) POTS and (d) MPS.

of some nanoparticles on the surface is probably due to sedimentation and weak van der Waals forces. Gold nanoparticles are expected to assemble on MPS by forming a covalent bond. Citrate capped gold nanoparticles have been shown to be able to bond to the MPS monolayer. However, due to the hydrophobicity of the thiol tail groups of MPS, the assembly of aqueous gold nanoparticles on the MPS surface is hindered [186]. This leads to the poor assembly observed. Our observation of poor assembly of aqueous citrate-capped gold nanoparticles on MPS is corroborated by Vakarelski et al., possibly due to propriety surfactants used for stabilisation [140]. However, after a phase transfer of aqueous gold nanoparticles to hexane, better assembly is observed (Fig. 3.3). During the phase transfer, the ligand capping layer of the gold nanoparticles is exchanged from citrate to oleate groups (Fig. 3.4)[184]. Sodium oleate acts as an emulsifer of hexanes in the aqueous gold colloidal solution while the addition of magnesium chloride to the emulsion promotes the salt formation of oleate anions. The C=C double bond of the oleate salt interacts and adsorbs onto the surface of the gold colloidal particles. These gold

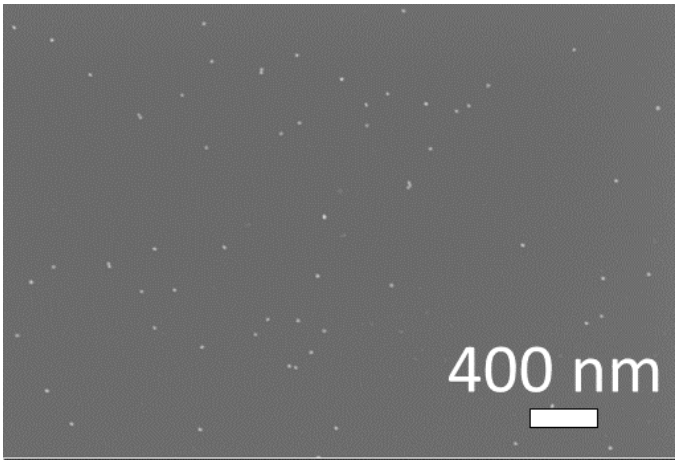


Figure 3.3: SEM images of gold nanoparticles after a phase transfer to hexane assembled on MPS.

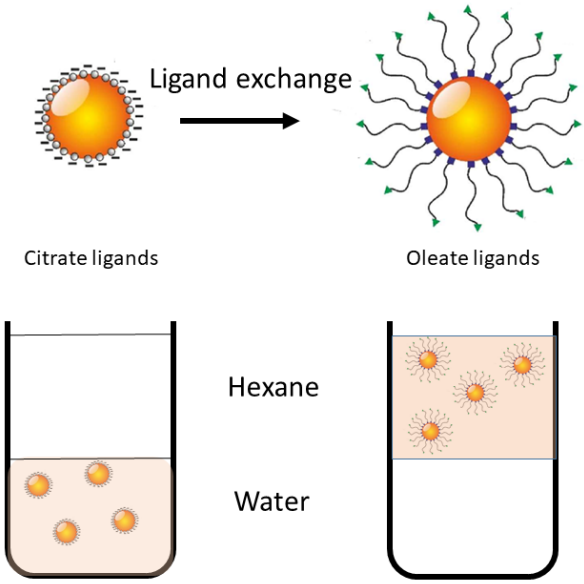


Figure 3.4: Schematic of the phase transfer process of gold nanoparticles from aqueous solution to hexane. The ligands are exchanged from citrate to oleate groups. The oleate groups have better affinty to hexane compared to the aqueous solution, thus achieving the phase transfer.

nanoparticles with the oleate ligands now have a higher affinity to hexane compared to the original aqueous solution, thus achieving the phase transfer, and subsequently better assembly of the modified gold nanoparticles on MPS. The need for a phase transfer to facilitate gold nanoparticles assembly on MPS makes MPS a poor choice to transfer gold nanoparticles attached to an APTES coated tip in an AFM.

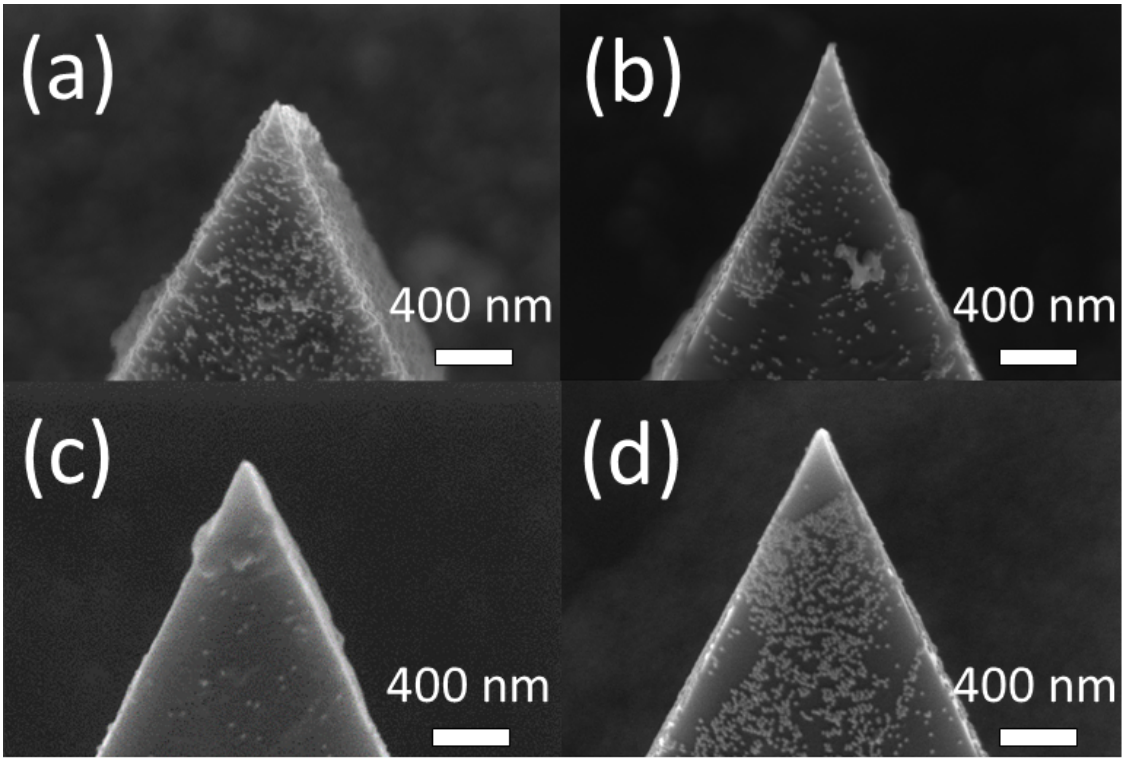


Figure 3.5: SEM images of AFM tips coated with (a) APTES, (b) TMODS, (c) POTS and (d) nothing.

3.3.3 AFM tips

Knowing that we can control the affinity of gold nanoparticles to the substrate based on what SAM we functionalise the silicon dioxide with, we are curious to see if we can do the same on an AFM tip with nanoscale features and a sharp geometry. Figure 3.5 shows AFM tips coated with various SAMs. We observe a densely packed assembly of gold nanoparticles on APTES and a few particles on TMODS and POTS. This is similar to the trends observed in Sec. 3.3.2. On the tip without any coating, we observed some nanoparticles adhered to the surface. However, they are not uniformly assembled and are in patches. This is likely due to the particles settling onto the surface over time.

Combination of monolayers

In an attempt to further localise particle attachment to only the tip apex, we coat the AFM tip with two different SAMs: APTES which has a high affinity to citrate

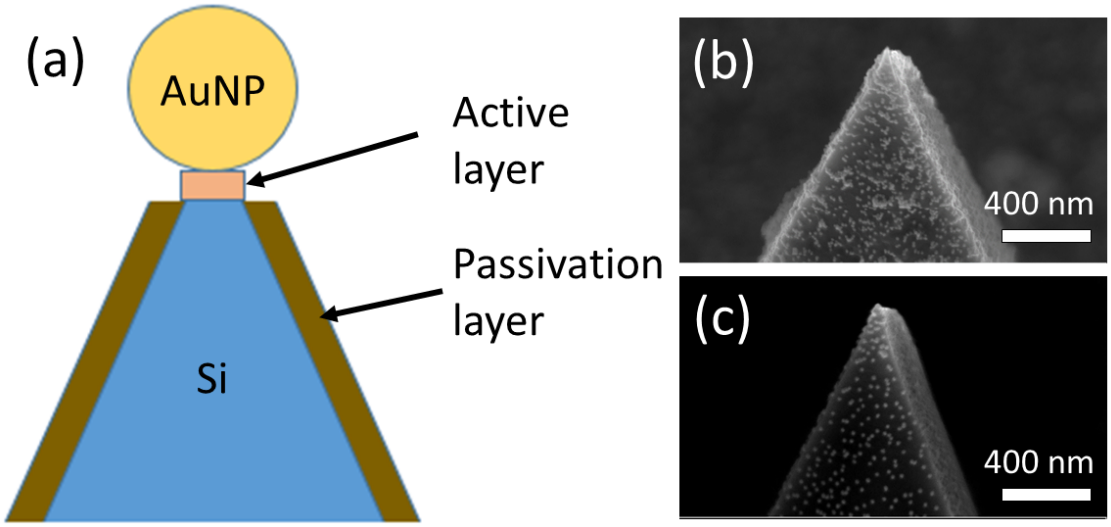


Figure 3.6: (a) Schematic representation of how a combination of monolayers will lead to localised assembly of gold nanoparticles. SEM images of (b) tip coated with APTES only and (c) tip coated with POTS followed by APTES only at the apex.

capped gold nanoparticles and POTS which has a low affinity. Figure 3.6(a) shows a schematic of the desired tip. POTS was first assembled onto the AFM tip followed by mechanical removal of POTS at the apex by means of contact mode AFM thus exposing the silicon underneath. APTES is then assembled onto the exposed silicon followed by nanoparticle assembly. We expect that the nanoparticles will preferentially attach to the small region of APTES at the apex while the POTS will repel gold nanoparticles due to its hydrophobicity. However, this was not observed (see Fig. 3.6(c)). Instead, gold nanoparticles are attached all over the tip cone albeit at a lower density as compared to a tip coated with purely APTES.

We hypothesize that APTES can diffuse through the POTS passivation coating layer. To test this hypothesis, we conducted water contact angle studies. Both APTES and POTS were assembled on multiple silicon dioxide substrates overnight (12 h), followed by rinsing. Subsequently, we immerse the POTS coated substrates in APTES solution for various lengths of times and take contact angle measurements periodically. Similarly, to see how POTS can diffuse through APTES, we repeat the same experiment but with APTES coated substrates in POTS solution. To be sure that the change in contact angle is not due to monolayer degradation over time, we compare the contact angle measurements to APTES and POTS

substrates placed in anhydrous toluene without any monolayer dissolved as a control experiment. The substrates were taken out and rinsed after various durations of monolayer assembly. POTS, being hydrophobic, has a large contact angle (∼90°) while APTES, being hydrophilic has a smaller contact angle (∼50°). Figure 3.7 summarises the results. Each data point is an average of the contact angle measured over three substrates that has undergone the same procedure. The contact angle of APTES coated substrates in POTS increases over time (red line) and tends towards the contact angle value for POTS alone. This suggests that POTS replaces most of the APTES molecules on the substrate. On the other hand, the contact angle for POTS submerged in APTES only changed from 98.3° to 68.2° more gradually over 70 h. In the control experiments in anhydrous toluene, we see that the contact angle of APTES and POTS coated substrates do not change much over 75 h. This suggests that the monolayers are able to diffuse through each other and assemble on the silicon substrate, thus changing its hydrophobicity. POTS diffuses into APTES more readily than APTES replaces POTS. This is consistent with the known facts that longer chains produces a better quality SAM film with higher packing density and less disorder [187, 188]. Therefore, it is more difficult for a shorter chain SAM to disrupt the longer chain SAM. Longer chain SAMs also have a larger heat of adsorption due to the larger attractive force between the long chain molecules. Thermodynamically, the adsorption of long chain SAMs is favoured. In the context of the double layer coating for localising gold nanoparticles to the tip apex, a long chain passivation monolayer should be selected (e.g. POTS). However, due to the fact that monolayers are able to diffuse into one another, it is difficult to achieve a clean passivative and attractive region as in Fig. 3.6(a).

3.4 Chapter Summary

In this chapter, we show that we can functionalise AFM tips with different types of monolayers. Some are attractive to citrate-capped gold nanoparticles while others inhibit their assembly. We tried to localise the assembly of nanoparticles to the tip apex by using a combination of attractive monolayers at the tip apex

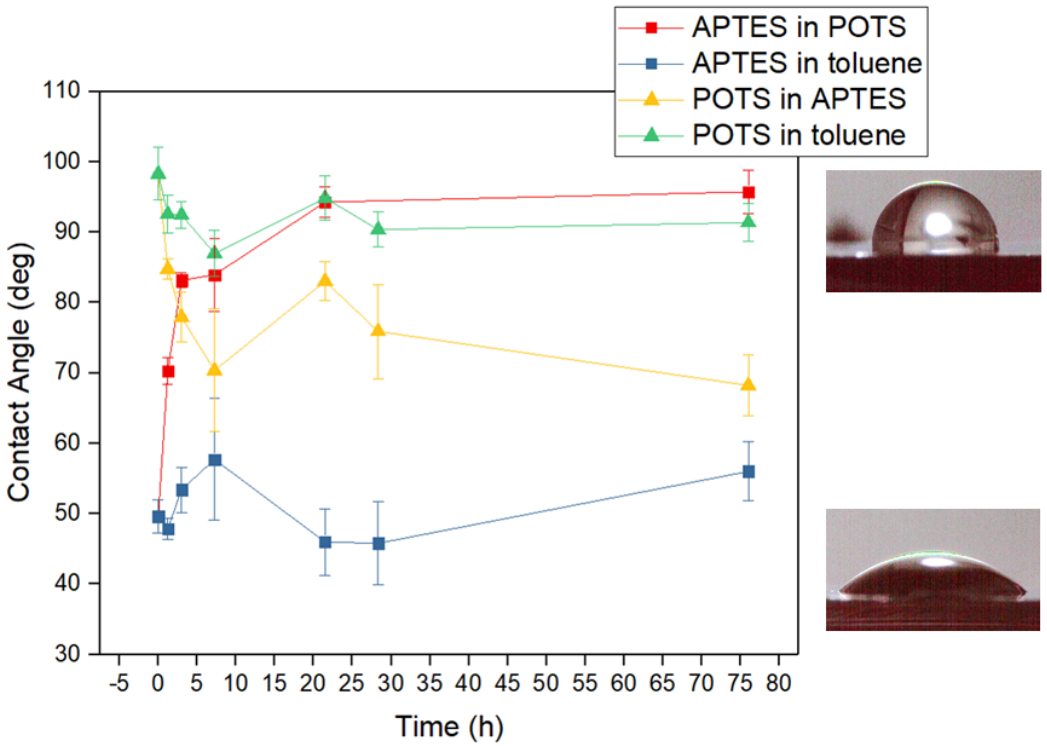


Figure 3.7: The change in contact angle of APTES functionalised substrates in POTS and vice versa over time. The inset shows water contact angle images of substrates coated with POTS (top) and APTES (bottom).

and inhibitive monolayers everywhere else on the tip. However, we found that the monolayers are able to diffuse into each other, thus rendering the passive monolayer less passive. Therefore, using chemical functionalisation of monolayers to localise picking up of particles on the AFM tip is not ideal. Improvements to this method will involve investigating an active monolayer that does not diffuse easily into the passive monolayer.

4

Coatings with conductive nano-filaments

Contents

4.1 Introduction 49
4.2 Aims of chapter 50
4.3 Creating high resolution tips 50
4.3.1 Coating, and switching in conductive AFM 51
4.3.2 Switching mechanism 52
4.3.3 Stability of filamentary probes 55
4.4 Single nanoparticle nanomanipulation 56
4.4.1 Dielectrophoresis - Theory 56
4.4.2 Materials and Methods 58
4.4.3 Results and discussion 59
4.5 Applications for high-resolution conductive AFM . . . 62
4.5.1 Kelvin probe microscopy - Theory 62
4.5.2 Materials and methods 65
4.5.3 Results and discussion 68
4.6 Chapter Summary 70

4.1 Introduction

We aim to improve upon the precision of attaching nanoparticles to the AFM tip from chemical methods seen in Chapter 3. In this chapter, we demonstrate a new type of electrical probe tip based on electrically reconfigurable coatings with high lateral resolution.

Some materials are known to be able to switch between a high resistance state (HRS) to a low resistance state (LRS). In this chapter, we explore two such materials, namely: germanium-antimony-tellurium (GST) and amorphous carbon.

The electrical resistance of GST can exhibit a decrease by over 2 orders of magnitude when switched from an amorphous to crystalline state in an AFM [189]. Similarly, amorphous carbon has been shown to exhibit field-induced threshold switching at the nanoscale from a HRS to LRS in the presence of high electric fields due to clustering of sp^2 sites within the sp^3 matrix [190]. Taking advantage of this property, we coat an AFM probe tip with either GST or amorphous carbon and induce switching locally at the tip apex to create an electrically high resolution AFM tip.

We show that by using this tip, we can (a) capture single gold nanoparticles and (b) enhance the existing geometrical resolution limits of tips. Extracts of this chapter were published in Nano Letters [191].

4.2 Aims of chapter

- Demonstrate an elegant method of fabricating high resolution conductive AFM probes
- Demonstrate its high resolution by (a) picking up of few to single gold nanoparticles on an AFM tip by dielectrophoresis and (b) enhancing the electrical resolution (due to geometrical limitations of the tip) of Kelvin probe force microscopy.

4.3 Creating high resolution tips

Figure 4.1 illustrates the concept of the high resolution tip. A regular AFM tip can be modified with a coating of switchable material that has a HRS and a LRS. By locally switching a region from HRS to LRS, the electric field can be confined to a region smaller than the dimensions of the probe tip.

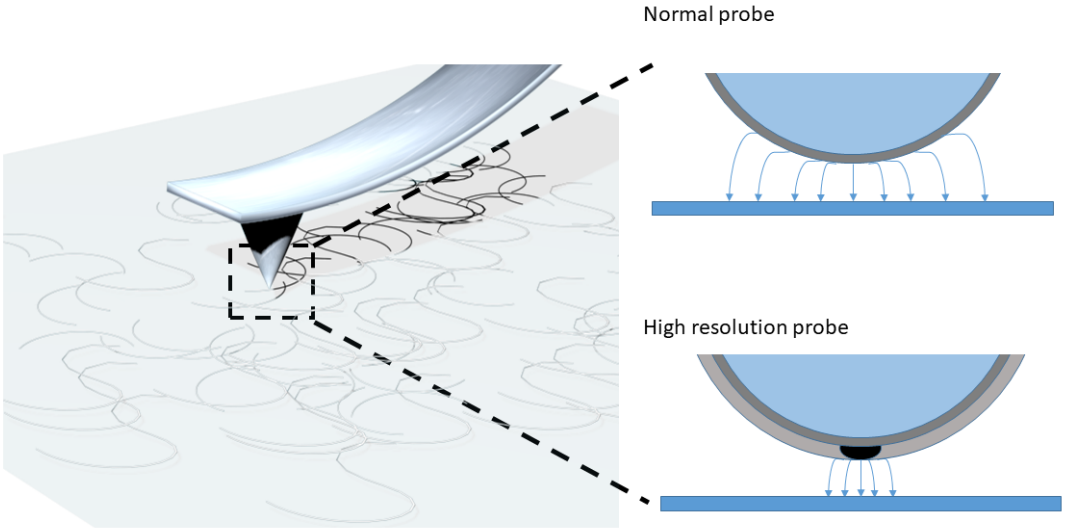


Figure 4.1: Schematic of an AFM tip illustrating how a conductive filament can enhance the resolution of electrical measurements. The high-resolution probe has a small volume of low resistance coating surrounded by the higher resistance coating. This confines the electric field to a region smaller than the dimensions of the probe tip, thus enhancing electrical resolution.

4.3.1 Coating, and switching in conductive AFM

GST is sputtered on platinum-coated tips with chromium as an adhesion layer with a Nordiko sputtering tool at 30 W, 5 mTorr, and 15 sccm of argon pressure and flow, respectively. Amorphous carbon is deposited by electron beam induced deposition (EBID). EBID is performed in a ZEISS Merlin SEM with an electron beam of 30 kV and 500 pA focused at the tip apex. The deposition thickness of the residual carbon (no precursor required) is monitored in situ. The use of EBID in a scanning electron microscope (SEM) allows high spatial accuracy in the deposition of amorphous carbon at the apex of the AFM tips.

After coating the tip with either amorphous carbon or GST, a conductive filament is locally created via conductive AFM. The modified tip is lowered into contact with a conducting substrate. A 510 kΩ resistor is placed in series to limit the current flow through the tip when the LRS is achieved. This protects the tip from high currents, which could melt and damage the coating. We monitor the I-V curve as the voltage between the tip and substrate is ramped up. One such switching curve is shown in Fig. 4.2(a). The resistance of the tip-sample contact

remains high until the threshold switching voltage is reached. The current measured suddenly increases at about 3 V. On the reverse voltage sweep, the current decreases linearly and the slope indicates a lower resistance compared to the slope during the forward voltage sweep. A subsequent low amplitude voltage sweep (i.e. 100 mV) is conducted to confirm that the tip-sample contact is now highly conductive.

This confirms that the switching of amorphous to conductive state is non-volatile. This non-volatility is crucial in ensuring high lateral resolution during subsequent electrical AFM measurements. We find that once switched, the probes remain in LRS for several days. The switching process is similar for both carbon and GST-coated tips. Carbon-coated tips can be advantageous over GST-coated ones as carbon is widely available and readily coated onto any commercially available tip.

Moreover, we are able to consistently create the conductive filaments at the tip apex instead of along the side walls. The highly conductive filament is created due to an electric field induced threshold switching. The electric field strength would be strongest between the substrate and the point on the tip that is closest to the substrate. Hence, at the threshold switching voltage, the conductive filament would be created at the region of highest electric field which would be at the tip apex, closest to the substrate.

4.3.2 Switching mechanism

Although the process to switch both carbon and GST is similar, we believe that the mechanism behind the electric field confinement is different.

GST

With GST, it is known that there are two main types of reversible switching mechanisms [192]. The first mechanism, known as ovonic threshold switching, occurs when a sufficiently high electric field is applied across the GST layer. When the threshold electric field is achieved, crystalline nanofilaments form (LRS), thus providing a conductive pathway. Around the conductive filament, the GST remains in an amorphous state (HRS). Once the resistivity drops, a second type of mechanism

known as ovonic memory switching occurs. This mechanism is induced by Joule heating due to current flow which can reversibly switch GST from the amorphous to crystalline state. The conductive filaments created in this work is a purely electronic process induced by high electric fields in the thin film GST, as only a single I-V spectroscopy is done to achieve threshold switching. This is similar to that reported by Yang et al. [189]. In contrast, repeated I-V spectroscopies resulted in Joule heating and an increase in the size of filaments [193], which would be detrimental for our application of creating electrically high-resolution AFM probes.

Carbon

For carbon, there are two possible mechanisms for the change in resistance. One possible mechanism is the clustering of sp^2 sites within the sp^3 matrix in the presence of high electric fields [190]. Alternatively, it could be due to migration of metallic ions from the substrate forming a metallic filament through the amorphous carbon (Similar to Ref. [194]).

We hypothesize that the switching from HRS to LRS of carbon in our experiments is due to reconfiguration of carbon rather than metallic filamentation. To test this hypothesis, we conducted the following four sets of experiments: (a) scaling behavior due to thickness of carbon, (b) different probe materials, (c) different substrates, and (d) switching with reverse voltage.

Referring to Fig. 4.2(b), we see that the switching voltage increases with coating thickness. This trend is not linear as was expected. This may be due to the thinness of coating used where any slight variations in coating thickness and accuracy in measuring the thickness can affect this result. Furthermore, in Fig. 4.2(c), we investigated how AFM tips of different materials affect the switching voltage (i.e., platinum, silicon, and diamond). Silicon and diamond are materials not known to undergo any kind of reconfiguration or phase change. Hence, we can conclude that the change in resistance is solely due to the amorphous carbon coating. We also observed threshold switching on platinum, indium tin oxide (ITO), and HOPG substrates (Fig. 4.2(d)), thus ruling out metallic filament formation.

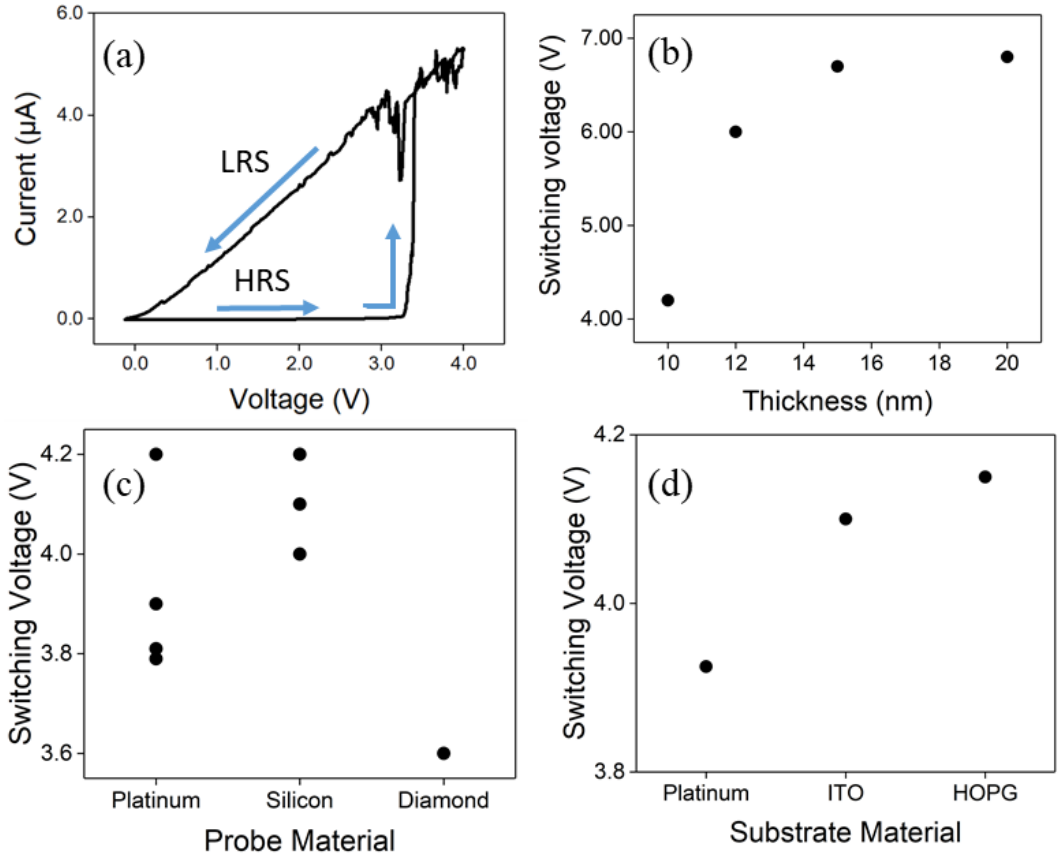


Figure 4.2: (a) Representative I-V curve measured when switching the carbon coating phase on the AFM tip. As the voltage is ramped up from 0 to 4 V, the sudden spike in current at about 3 V suggests a change from a high resistance state to a low resistance state. A linear line on the reverse ramp indicates that the phase change is non-volatile. (b) Switching voltage versus thickness of amorphous carbon coating. (c) Switching voltages of varied composition probes coated with 10 nm of amorphous carbon. (d) Switching voltages on different substrate materials using silicon probes coated with 10 nm of carbon.

Moreover, we also observed threshold switching even when the voltage bias is reversed. Since metallic filamentation is polarity dependent, we can conclude that the change from HRS to LRS is due to reconfiguration of carbon. Additionally, no significant metal signal was found by EDX in the carbon coating (Fig. 4.7(b)). The experiments described above suggest that reconfiguration of amorphous carbon is the mechanism behind the threshold switching behaviour and hence the creation of high-resolution electrical probes.

We note that a previous approach of fabricating electrically high-resolution tips via filamentation has been reported by Hong et al., where a conventional

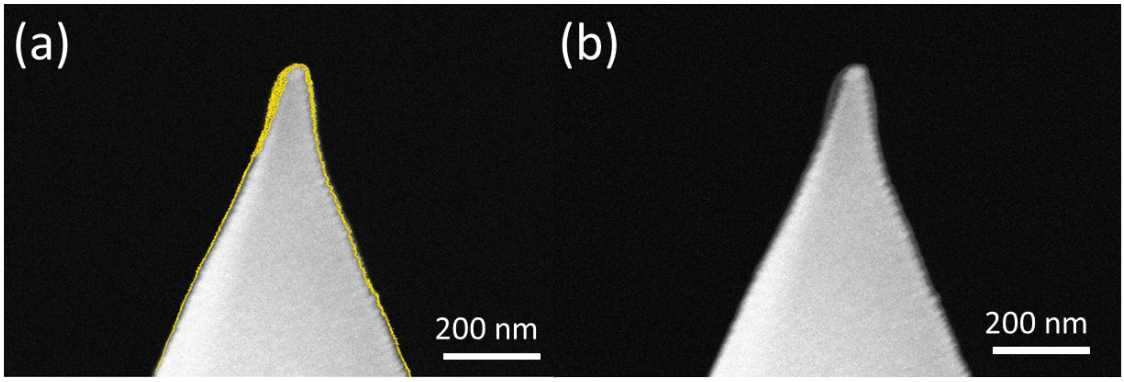


Figure 4.3: (a) SEM images taken of a carbon coated tip in the LRS 2 weeks after experiments, stored in ambient conditions. The yellow colour in (a) highlights the carbon coating. (b) shows the original SEM image of the same tip.

conductive AFM tip was coated with alumina followed by contacting a bottom metal (palladium) to form a local metal-insulator-metal junction [194]. A conductive pathway is formed through the alumina due to metal migration from the substrate. Our approach of coating with a reconfigurable material followed by switching offers several advantages. The phase change is intrinsic to the coating and is independent of the substrate or tip material as in the case with metallic filamentation described by Hong et al. This means that reconfiguration and measurement can be done in-situ. Moreover, the use of carbon as the active coating material offers the possibilities of functionalisation as well as being widely available and readily coated onto AFM tips.

4.3.3 Stability of filamentary probes

It is important that the high resolution probes are stable, at least over the period of time it takes to conduct the experiments. We have seen that the tip remains highly conductive from subsequent IV sweeps after switching of both carbon and GST coated tips. This supports the non-volatile switching behaviour as reported previously [189, 190]. Moreover, we took SEM images of a carbon coated tip, 2 weeks later, in the LRS after multiple frequency-modulated Kelvin probe force microscopy (FM-KPFM) scans and stored in ambient conditions (Fig. 4.3). Although the tip apex is blunt due to repeated scanning, the carbon coating remains intact.

4.4 Single nanoparticle nanomanipulation

By combining dielectrophoresis and our high resolution filamentary probe, we show that we can pick up nanoparticles with high precision. We consider high precision here if nanoparticles are picked up only at the tip apex.

Particles, including those which are dielectric, will experience a dielectrophoretic force when subjected to a non-uniform electric field [195]. By exploiting the sharp geometry of AFM tips, Leiterer et al. have used dielectrophoresis to attach silver nanoparticles to AFM tips for tip-enhanced Raman spectroscopy (TERS) [196]. However, regardless of the tip size used, nanoparticles on such probes adhere as clusters. This is due to the stray electric field that exists at the sidewalls. Single nanoparticle tips are the preferred geometry for a TERS probe as it excludes complex interactions between the many-nanoparticle systems. By using our high electrical resolution tip, we now demonstrate the ability to pick up single nanoparticles.

4.4.1 Dielectrophoresis - Theory

A dielectric particle in a non-uniform electric field would experience a dielectrophoretic force. This phenomenon is known as dielectrophresis (DEP) [195]. All particles, charged or neutral, would experience a dielectric force in the presence of electric fields. Figure 4.4(a) illustrates how a non-uniform electric field can be generated between a pin and plate electrode.

The time averaged DEP force acting on a spherical particle of radius R in a non-uniform time varying sinusoidal field is given by [197]:

$$\langle F_{DEP} \rangle = \pi \epsilon_0 \epsilon_m R^3 Re[CM^*] \nabla |\overrightarrow{E}_{rms}|^2 \tag{4.1}$$

where ϵ_0 and ϵ_m is the permittivity of vacuum and medium respectively. $\overrightarrow{E}_{rms}$ is the rms value of the electric field. CM is known as the Clausius-Mosotti factor given by:

$$\frac{\epsilon_p^* - \epsilon_m^*}{\epsilon_p^* + 2\epsilon_m^*} \tag{4.2}$$

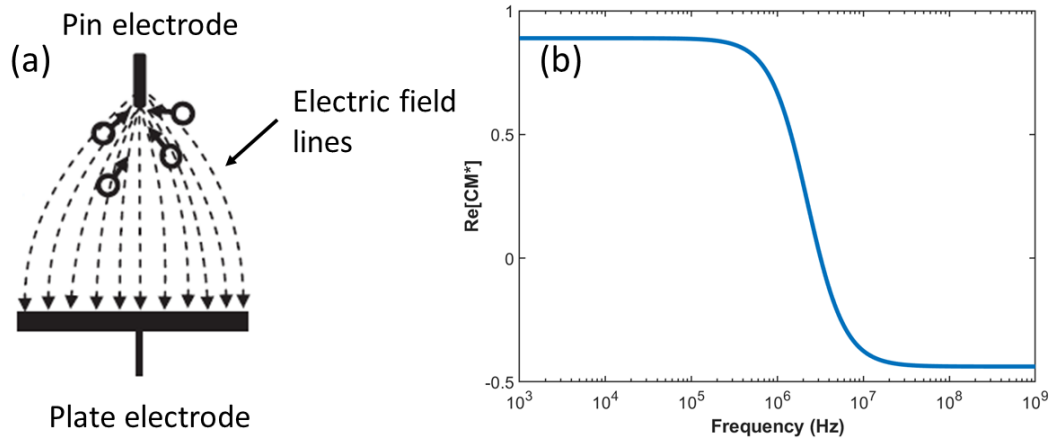


Figure 4.4: (a) Schematic describing dielectrophoresis. A non-uniform field is produced between the sharp and planar electrode. The particle will be attracted to or repelled from the sharp electrode in positive or negative DEP respectively. (b) Graph showing the dependence of frequency on Re[CM]. This determines whether positive or negative DEP occurs.

where subscripts p and m refer to particle and medium respectively. The direction of this force is determined by the real part of the CM factor. This determines whether the particle is directed along or against the field gradient. The real part of the CM factor is given by [197]:

$$Re[CM^*] = \left[\left(\frac{\omega^2\tau^2}{1+\omega^2\tau^2}\right)\left(\frac{\epsilon_p - \epsilon_m}{\epsilon_p + 2\epsilon_m}\right) + \left(\frac{1}{1+\omega^2\tau^2}\right)\left(\frac{\sigma_p - \sigma_m}{\sigma_p + 2\sigma_m}\right)\right] \tag{4.3}$$

where τ is known as the relaxation time for the interfacial charge given by:

$$\tau = \epsilon_0 \frac{\epsilon_p + 2\epsilon_m}{\sigma_p + 2\sigma_m} \tag{4.4}$$

From Eq. 4.1, we can see that the strength of this force depends on the medium and particles' electrical properties, particles' shape and size and the frequency of the applied electric field. This has enabled the manipulation of nanoparticles between two electrodes [198–200].

Moreover, the polarity of the dielectrophoretic force is determined by the particles' polarisability relative to that of the surrounding medium expressed by the CM

factor. If the CM factor is positive (particle more polarizable than the suspension medium), a time-averaged force pulls particles towards the region of strong electric field strength. This is known as positive DEP. Conversely, a negative CM factor would direct particles towards regions of weak electric field strength. The frequency at which positive DEP switches to negative DEP is known as the crossover frequency. Using this property, separation of nanoparticles can be achieved [201].

In order to attract particles to our AFM tip, we want to operate in the positive DEP regime. We use Eq. 4.3, to calculate the frequencies that we can apply to ensure positive DEP. For gold nanoparticles in a water suspension, the conductivity and permittivity is 4×10^{-4} S/m and 80 ϵ_0, respectively [202]. The conductivity of gold nanoparticles is 0.01 S/m as compared to 1×10^7 S/m for bulk gold as a result of the stabilising surface coating layer [203]. The result is plotted in Fig. 4.4(b). We can see that the crossover frequency is about 3.2 MHz. Hence any frequency lower than that will result in positive DEP.

4.4.2 Materials and Methods

Dielectrophoresis To Capture a Single Nanoparticle

We used the phase change material coated probes with a nanoscale conductive filament as one electrode and a planar platinum substrate as the other electrode. The tip is submerged into a colloidal solution of 20 nm gold nanoparticles. A voltage of 10 V peak-to-peak at 100 kHz was applied for 60 s. The distance between the AFM probe and substrate was set to 500 nm. After picking up a particle, the tip is removed, rinsed in DI water and blown dry with nitrogen gas. The tip is subsequently taken to an SEM to confirm that gold nanoparticles have been picked up.

TEM Characterization

Transmission electron microscopy was carried out in TEM and scanning TEM modes in conjunction with EDX spectroscopy maps for elemental confirmation and distribution. A JEOL GrandARM was used at 300 kV with an Oxford Instruments XMAX 100 EDX detector. The AFM tip devices were held at the optimum z-height

of the objective lens with a custom-fabricated clamping tip compatible with the JEOL quick-exchange holder [204].

4.4.3 Results and discussion

Figure 4.5(a) shows a schematic of the process of creating a nanoscale conductive filament and subsequently capturing a single nanoparticle. The conductive filament is depicted to follow a random path through the coating layer due to defect sites as well as its amorphous nature (i.e. no long range order) before threshold switching. This percolative formation of filamentry paths can be described according to general filamentary theory [205]. Despite the irregularly shaped filament, it does not hinder the picking up of nanoparticles as experimentally observed. Secondary electron microscope images were taken at different stages of the dielectrophoresis process. Fig. 4.5(b) shows the actual SEM image of a carbon-coated tip before switching, Fig. 4.5(c) after switching, and Fig. 4.5(d) after dielectrophoresis to pick up the nanoparticle.

We proceed to compare probes in which nanoscale conductive filaments have been created during switching and probes without this filamentation. Figure 4.6(a) shows a representative image of a reconfigured carbon tip after dielectrophoresis. A single nanoparticle is observed at the tip apex and no nanoparticles were observed along the tip cone. We show a large portion of the tip cone to emphasize the locality of using a filamentary probe due to confinement of electric fields. Figure 4.6(b) shows a carbon-coated tip but without reconfiguration, hence no conductive filaments were formed. After dielectrophoresis, clusters of nanoparticles were observed along the tip. Similarly, we observe clusters of nanoparticles picked up by a normal platinum tip (Fig. 4.6(c)). This is similar to that observed by Leiterer et al. when they used highly doped silicon tips to pick up silver nanoparticles [196].

In comparison, Fig. 4.6(d) and (e) shows the filamentary GST and carbon probes, respectively. We note that there appears to be two nanoparticles attached to the tip in Fig. 4.6(d). However, from the transmission electron microscope (TEM) images we see a large improvement in particle trapping resolution with switched GST and

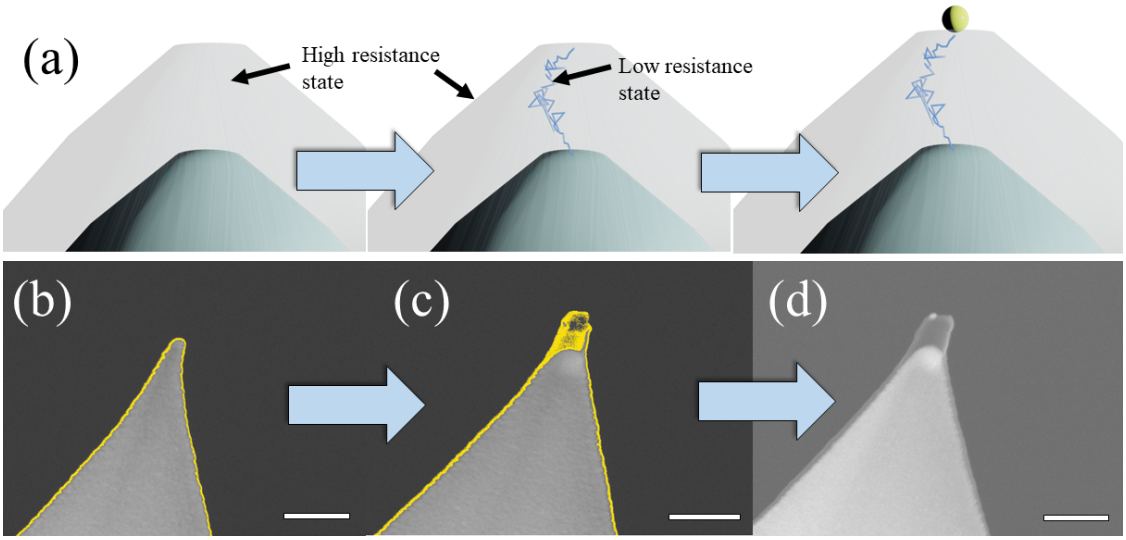


Figure 4.5: (a) Schematic showing the process of fabricating highresolution probes. The reconfigurable material is coated onto an AFM tip followed by switching a nanoscale conductive filament at the apex of the tip. The tip can then be used to pick up a nanoparticle through dielectrophoresis or to conduct high-resolution electrical measurements. (b) SEM images of a representative carbon-coated platinum tip before threshold switching, (c) after switching, and (d) after dielectrophoresis to pick up the 20 nm gold nanoparticle. The yellow color highlights the carbon coating. The scale bars are 200 nm.

carbon tips compared to a tip that has not undergone phase switching (Fig.4.6(b)). We have achieved single nanoparticle resolution in the case of filamentary carbon-coated tips (Fig. 4.6(e)). Moreover, we observe that some of the particles picked up appear to be slightly to the side. This is due to the tilt angle of the cantilever in the AFM, and possibly some substrate tilt, resulting in the tip touching the surface at a point slightly to the side. The conductive filaments are thus created along that point as it is closest to the substrate and experiences the highest electric field.

Additionally, Fig. 4.7(a) and 4.7(b) show the EDX images of the GST-coated and carbon-coated tips respectively. From these images, we can verify that the coating is GST and carbon. Moreover, we see that the particles picked up is indeed gold.

The fact that we can pick up few/single nanoparticles highly localised at the tip apex provides good evidence of the formation of conductive filaments at the apex.

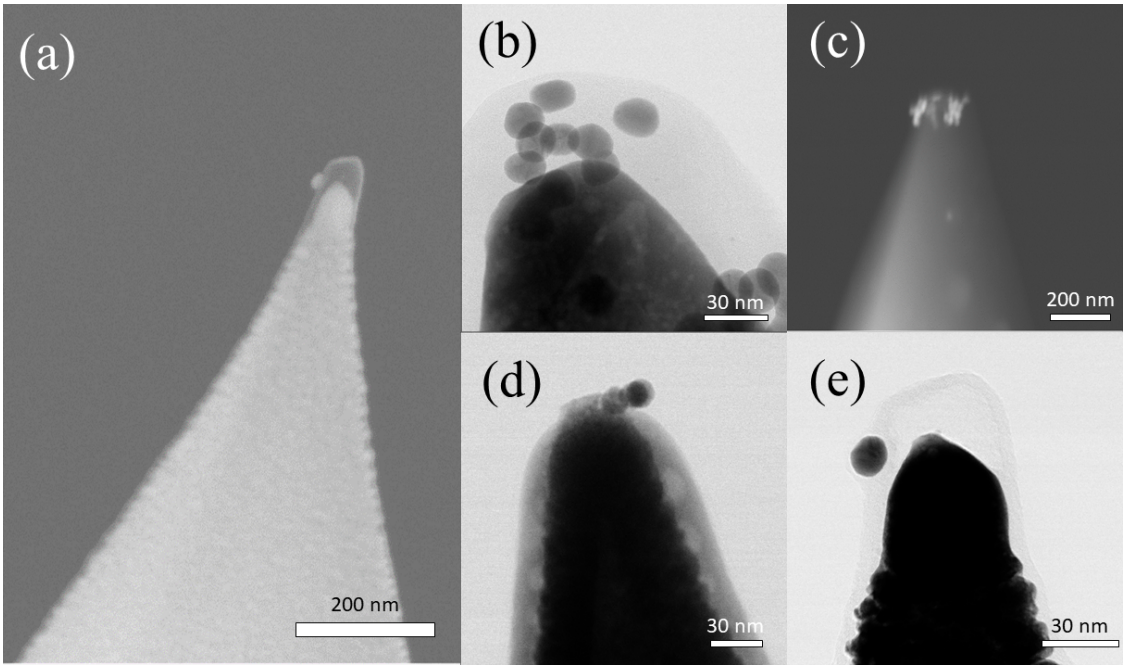
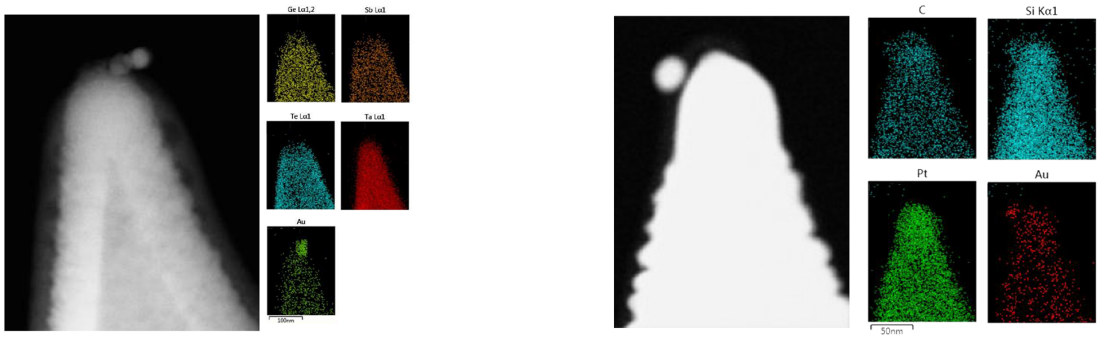


Figure 4.6: Images compare the effectiveness of probes for capturing nanoparticles using electric fields with and without conductive filamentation. (a) An SEM (back scattered electron) image of a representative carbon-coated platinum tip after dielectrophoresis to pick up a single gold nanoparticle. A large portion of the tip cone illustrates the locality of the electric field resulting in single nanoparticle capturing only at the apex. (b) Carbon-coated tip without creation of a nanoscale conductive filament, (c) Pt tip without a coating, (d) filamentary GST tip, and (e) filamentary carbon-coated tip picks a single Au nanoparticle. Images are a compilation collected by SEM and TEM, thus the contrast reversal.



(a) **(b)**

Figure 4.7: (a) STEM high-angle annular dark field image (left) and corresponding EDX maps of a representative switched GST tip after picking up gold nanoparticles from a single contact point on the apex of the tip. (b) STEM image and corresponding EDX maps of a representative switched carbon tip after picking up a 20 nm gold nanoparticle. EDX confirms the nanoparticle is indeed gold.

4.5 Applications for high-resolution conductive AFM

Kelvin probe force microscopy (KPFM) is a variant of noncontact mode AFM that measures the contact potential difference (CPD) between the tip and sample. In this way, the work function of the sample can be calculated and mapped out with nanometer-scale precision. KPFM is used in the study of organic materials and device [206, 207] , heterostructures [208] and biological materials [209, 210].

4.5.1 Kelvin probe microscopy - Theory

The basic principle in KPFM involves applying an alternating current (AC) voltage, U_{AC} to the cantilever and tracking its response. By additionally applying a direct current (DC) voltage, U_{DC}, to the tip, the tip-sample electrostatic force will be minimised when this applied voltage is equal to the CPD (i.e. $U_{DC} = U_{CPD}$). There are two methods to track the response of the cantilever: Amplitude modulation (AM) and frequency modulation (FM). KPFM is commonly carried out in AM mode due to ease of implementation. On the other hand, FM mode enables better resolution than AM mode due to improved tip-sample sensitivity.

The tip-sample electrostatic force can be calculated by considering the capacitance C of the tip-sample gap. Considering the capacitor's energy $W = \frac{1}{2}C(\Delta U)^2$, the electrostatic force is given as [211]:

$$F_E = \frac{1}{2}\frac{\partial C}{\partial z}(\Delta U)^2 \tag{4.5}$$

where z is the tip-sample distance and the potential difference between and sample is $\Delta U = U_{ext} - U_{CPD}$. U_{ext} is the sum of all external voltages applied to the tip or sample. In our experiments, we ground the sample and apply both an AC and DC voltage to the tip. This is represented as $U_{ext} = U_{DC} + U_{AC}\sin(\omega_E t)$. Subtituting this into Eq. 4.5, we see that the electrostatic force can be separated into a static and two dynamic components given by:

$$F_{ext} = F_{DC} + F_{\omega} + F_{2\omega} \tag{4.6}$$

$$= \frac{1}{2}\frac{\partial C}{\partial z}\left[\left(U_{DC} - U_{CPD}\right)^2 + \frac{U_{AC}^2}{2}\right] \tag{4.7}$$

$$+ \frac{\partial C}{\partial z}\left(U_{DC} - U_{CPD}\right)U_{AC}\sin(\omega_E t) \tag{4.8}$$

$$- \frac{1}{4}\frac{\partial C}{\partial z}U_{AC}^2\cos(2\omega_E t) \tag{4.9}$$

Equation 4.8 is the fundamental equation describing AM-KPFM. The cantilever response at ω_E is monitored by means of a lock-in amplifier. When $U_{DC} = U_{CPD}$, the amplitude response at ω_E vanishes. The feedback loop will minimise the response amplitude by adjusting U_{DC} accordingly. By recording U_{DC}, we can have a measure of CPD.

The amplitude of the electrostatic force is proportional to the gradient of the capacitance (Eq. 4.8). Hence, the large surface area of the tip cone and the cantilever can contribute significantly to the gradient in capacitance [212]. As the surface potential is averaged over a larger area, the lateral resolution is decreased.

In order to reduce the effect of long-ranged electrostatic interaction due to the tip-cone and cantilever, force gradient detection can be used [213, 214]. An AC bias causes both a change in the electrostatic force (Eq. 4.6) and angular resonance frequency, ω_0. The angular frequency can shift due to the presence of a tip-sample force, F_{TS}. The modified angular resonance frequency can be described by an effective spring constant k_{eff}, and is given by:

$$\omega_0^{'} \approx \sqrt{\frac{k_{eff}}{m}} \tag{4.10}$$

$$= \sqrt{\frac{1}{m}\left(k - \frac{\partial F_{ts}}{\partial z}\right)} \tag{4.11}$$

where k is the undisturbed spring constant of the cantilever. The magnitude of this change in frequency is proportional to electrostatic force gradient and hence to

the second derivative of the capacitance, C''. As C'' is more sensitive to the local tip-sample interactions, FM detection leads to superior lateral resolution [215].

The change in frequency can be monitored by means of a phase-locked loop. Alternatively, another AC electrical signal can be applied and mixed with the mechanical oscillation of the cantilever, ω_m. In this case, the capacitance gradient will also oscillate with frequency ω_m. Hence, we can write the capacitance gradient as a Fourier series,

$$\frac{\partial C}{\partial z}\Big(t\Big) = \sum_{n=0}^{\infty} a_n \cos(n\omega_m t) \tag{4.12}$$

Similarly, by substituting Eq. 4.12 into Eq. 4.5, we can derive the different components of the electrostatic force:

$$F_{\omega_E} = \frac{a_0}{2}\Big(U_{DC} - U_{CPD}\Big)U_{AC}\sin(\omega_E t) \tag{4.13}$$

$$F_{2\omega_E} = \frac{a_0}{8}U_{AC}^2\cos(2\omega_E t) \tag{4.14}$$

$$\begin{aligned} F_{\omega_m \pm \omega_E} = {} & \frac{1}{2}a_1\Big(U_{DC} - U_{CPD}\Big)U_{AC} \\ & \cdot \left[\sin\Big(\big(\omega_E - \omega_m\big)t\Big) + sin\Big(\big(\omega_E + \omega_m\big)\Big)\right] \end{aligned} \tag{4.15}$$

$$\begin{aligned} F_{\omega_m \pm 2\omega_E} = {} & -\frac{1}{8}a_1 U_{AC}^2 \\ & \cdot \left[\cos\Big(\big(2\omega_E - \omega_m\big)t\Big) + sin\Big(\big(2\omega_E + \omega_m\big)t\Big)\right] \end{aligned} \tag{4.16}$$

We can see that Eq. 4.13 and 4.14 corresponds to Eq. 4.8 and 4.9 in AM-KPFM. Equation 4.15 is the fundamental equation in FM-KPFM. From Eq. 4.15 and 4.16, we see that electrostatic signals can also be detected at the sidebands of the mechanical osciallation, ω_m. Since Eq. 4.15 also contains the $(U_{DC} - U_{CPD})$ term similar to Eq. 4.13, the monitored sideband amplitudes can be minimised by adjusting U_{DC} accordingly through the feedback loop.

In the subsequent sections, we demonstrate how our high resolution electrical probe shows an improved resolution in both AM- and FM-KPFM methods. We take

into consideration that FM-KPFM is more sensitive to tip-surface interactions and that our filamentry probe technique is a local tip-apex phenomena. We show that we can achieve a spatial resolution beyond the geometrical limitations of commercial platinum probes (i.e., an improvement of ∼48%).

4.5.2 Materials and methods

EVA/MWCNT solution preparation

Multiwalled carbon nanotube and ethylene vinyl acetate copolymer composite (EVA/MWCNT) solution was prepared as described by Mazzotta et al. [216]. 5 mg of Ethylene-Vinyl Acetate pellets (ELVAX 150, Dupont, 32% by weight vinyl acetate comonomer content) were dissolved in 10 mL of chlorobenzene (ACROS Organics, ACS reagent grade) by stirring at room temperature for >24h. 1 mg of Nanocyl MWCNTs (Nanocyl, Belgium) were dispersed in the solution by mixing with an ultrasonic probe for 10 min, breaking up CNTs clusters and allowing the polymer to wrap individual CNTs. The mixture was then centrifuged at 10,000 g for 8 min to remove the non-solubilized nanotubes and other impurities. The supernatant, containing the polymer-wrapped CNTs, was then collected and added to 20 mL of toluene (Sigma-Aldrich, puriss. p.a. grade), then heated overnight at 60^{o}C to induce the aggregation of the polymer-wrapped CNTs while the excess EVA polymer dissolved. The mixture was then centrifuged at 16,000 g for 4 min and the precipitate, consisting of pellets of EVA-wrapped tubes, was collected and dispersed in 50 mL of chloroform (Acros Organic, for HPCL grade, stabilized with 25 ppm amylene). The solution was then treated with an ultrasonic probe for 2 min at ∼40 W output power.

Sample preparation

EVA/MWCNT was deposited with a custom-made open science hardware spray coater (http://afmd.github.io/LANDS). ITO substrates (20 Ohm/sq, Thin Film Devices Inc, USA) were cleaned for 10 minutes in a sonication bath at 55^{o}C of a 2.5% solution of Hellmanex in DI water, followed by DI water, acetone and 2-propanol.

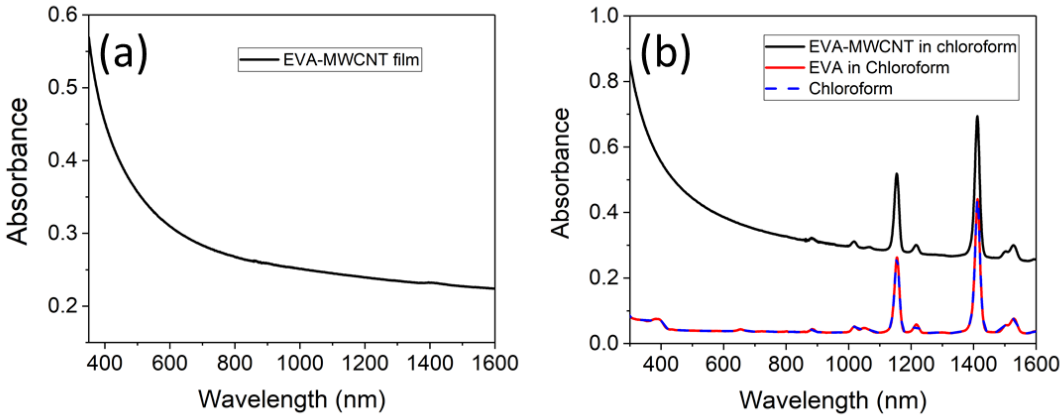


Figure 4.8: (a) Absorption spectra of the EVA-MWCNT film. (b) Absorption spectra of chloroform, EVA in chloroform and EVA-MWCNT in chloroform.

Substrates were then dried with a stream of compressed dry air, treated for 10 minutes in a UV-Ozone cleaner and attached to the spray coater bed applying Kapton tape on their edges. The bed temperature was kept at 100^{o}C for the whole spraying process. 1 mL of the solution prepared according to the previous section was further diluted by adding 49 mL of chloroform, loaded in a syringe and delivered to the nozzle at a rate of 4 mL/min, where a 3 bar compressed air stream atomized the solution. The nozzle was placed at 45 mm height from the bed, and rastered the substrates at a speed of 200 mm/s until the whole content of the syringe was delivered.

We confirm the presence of CNTs by measuring its absorption spectra (Fig. 4.8). Fig. 4.8(a) shows the absorption spectra of the EVA-MWCNT film. The EVA is transparent in the whole visible spectrum. Fig. 4.8(b) shows the absorption spectra of chloroform, EVA in chloroform and EVA-MWCNT in chloroform. The absorption of pure chloroform overlaps perfectly with the EVA-chloroform spectrum. The absorption of CNTs is a continuous spectrum with no peaks as MWCNTs have multiple shells and offers a continuum of available states. Therefore, no sharp features are visible with the exclusion of the peaks from the solvent that they are dispersed in (i.e. chloroform).

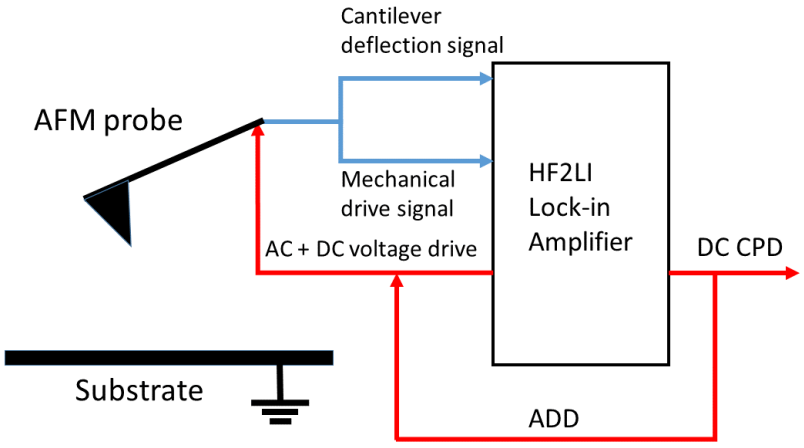


Figure 4.9: Schematic of the set up for FM-KPFM.

KPFM Characterisation

KPFM measurements were carried out on an Asylum Research MFP3D AFM. A variety of probes were used as is or coated with GST or carbon. These include platinum-coated (TAP150E-G), silicon-coated (TAP300-G), and diamond-coated (AIO-DD) probes. We used 5 different Pt tips, 5 GST coated tips, and 10 carbon coated tips. The typical tip radius is 25 nm. The topography feedback was performed in AM at the resonance frequency of the cantilever and the oscillation amplitude was kept to about 40 nm. To perform FM-KPFM, we used an external lock-in amplifier (Zurich Instruments, HF2LI). The FM-KPFM method used is the FM sideband method as described by Axt et al.[212]. We electrically excite the cantilever at ω_E = 2.5 kHz with a driving voltage of 3 V and demodulate at the sidebands $\omega_m + \omega_E$, where ω_m is the frequency of mechanical oscillations. A schematic of the set up can be seen in Fig. 4.9. For the dual-pass AM-KPFM, the topography and CPD measurements are completely decoupled. In the first pass, the topographic information is captured in tapping mode. During the second pass, the mechanical excitation of the cantilever is turned off and the tip follows the topography as imaged in the first pass at a defined lift height of 20 nm above the surface while measuring the CPD. All scans were conducted at 0.5 Hz and repeated multiple times.

4.5.3 Results and discussion

Figure 4.11 panels a – c and d – f are representative topography and CPD data collected with platinum tips in AM- and FM-KPFM, respectively. In 2-pass AM- and FM-KPFM, the full width half-maximum (fwhm) of the CPD line cut of a carbon nanotube in Fig. 4.11(b), (e) with a platinum tip is 82.3 and 68.5 nm, respectively. In AM-KPFM, although the topography is clearly observed, there is little contrast in the potential map. In FM-KPFM, the lateral resolution compared to AM-KPFM is drastically improved. This is because in FM-KPFM, the feedback loop is based on the force gradient. By using the force gradient instead of the force as the feedback mechanism, long-range electrostatic interactions of the cantilever and tip cone can be reduced. Thus, the tip-sample electrostatic interactions measured are mainly contributed by the tip-substrate interaction (i.e., more tip-sensitive technique) [214]. This is particularly useful in the case of our high-resolution probe as the tip modification is localized at the tip. We observed that in both AM- and FM-KPFM with the platinum tip, the fwhm of the CPD signal is greater than the fwhm of the topography signal.

In AM-KPFM with the platinum tip, the CPD fwhm is 1.70 times that of the topography fwhm. In FM-KPFM, the fwhm of the CPD is 1.37 times that of the topography. We then conducted the same experiments with the switched GST and reconfigured carbon-coated tips. Figure 4.11 panels g-l and m-r summarizes the KPFM results of switched GST and carbon tips, respectively. The resolution obtained in the CPD images are improved in both AM- and FM-KPFM compared to when an uncoated platinum tip is used. The fwhm of the CPD in AM-KPFM for the GST (carbon) tips improved by 25% (11%) from 82.3 to 64.1 nm (73.2 nm) and the fwhm in FM-KPFM is improved by 26% (48%) from 68.5 to 47.0 nm (35.8 nm). With the switched GST (carbon) tip, the fwhm of the CPD is 0.80 (1.35) and 0.65 (0.48) times the fwhm of the topography in AM- and FM-KPFM respectively. This results in the ability to resolve below the geometrical limits of the platinum tip.

We note that the nanotubes appear to range from 7 to 20 nm in diameter. An SEM image (Fig. 4.10) shows that the nanotubes are of consistent diameter but

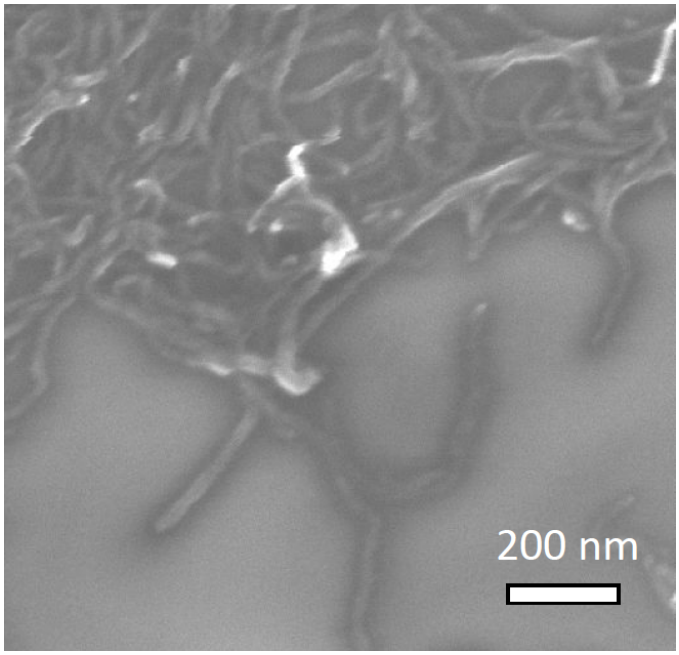


Figure 4.10: SEM image of CNTs.

may be agglomerated and overlapping in some areas. Hence, they appear to be thicker in some areas in the AFM images. FWHM cross sections were taken across sections where single nanotubes are observed. The cross sections we compared are across the same line to ensure fairness in comparison.

The topographical resolution is similar for both AM- and FM-KPFM. However, it is observed that the topographical resolution is consistently slightly better for the platinum tips compared to the carbon tips. To understand why this is the case, we observe the tips in an SEM before and after reconfiguring of the amorphous carbon (Fig. 4.5(b,c)). It can be seen that there is a significant change in shape and volume of the carbon at the apex. The tip radius increases after switching thus resulting in a poorer topographical resolution. We do not have a good explanation for this dramatic deformation in carbon. However, the thickness-dependent data (Fig. 4.2(b)) supports that the switching behaviour observed was due to the carbon coating rather than any other mechanism.

No significant change in tip-shape was observed with the switched GST tips. Despite the fact that the tip radius is larger in the carbon tips compared to the Pt tips, the resolution of the CPD images taken with the carbon tips is higher than

that of the Pt tips. In Fig. 4.11(q), we see that the fwhm of the CPD is even smaller than that of the topography. This is further evidence that carbon filamentation results in enhanced resolution of electrical AFM measurements. We observe that the CPD values differ between the platinum, GST and carbon tips. This is due to the differences in the work functions of the coating material at the apex. Moreover, the different phases of GST and carbon at the apex also affects the CPD measured. Therefore, these results should only be taken in a qualitative manner. Quantitative results may be analysed using a similar method suggested by Keith et al. [217].

4.6 Chapter Summary

In summary, we have demonstrated a readily available method for manufacturing high-resolution electrical AFM probes with nanoscale precision not attainable by standard probes using controlled phase switching of GST and amorphous carbon at the nanoscale. Virtually any probe can be turned into a high-resolution probe in-situ with this method. This will benefit all electrical AFM techniques. Moreover, as sputter deposition is used, mass production of GST probes can be achieved. We confirmed the presence of conductive filamentation by observing IV curves during switching and by successful implementation of two applications. Furthermore, we demonstrated the ability to pick up a single nanoparticle at the apex through the use of dielectrophoresis at ambient conditions and high resolution AM- and FM-KPM on carbon nanotube samples.

Methods attempted to place these nanoparticles after picking them up are briefly discussed in Appx. A.

Author Contributions

The CNT samples were prepared by Giulio Mazzotta (Department of Physics, Oxford). TEM was done together with the help of Judy Kim (Department of Materials, Oxford). Preparing the high resolution probes, KPFM set-up and measurements, and picking up of nanoparticles were performed by me.

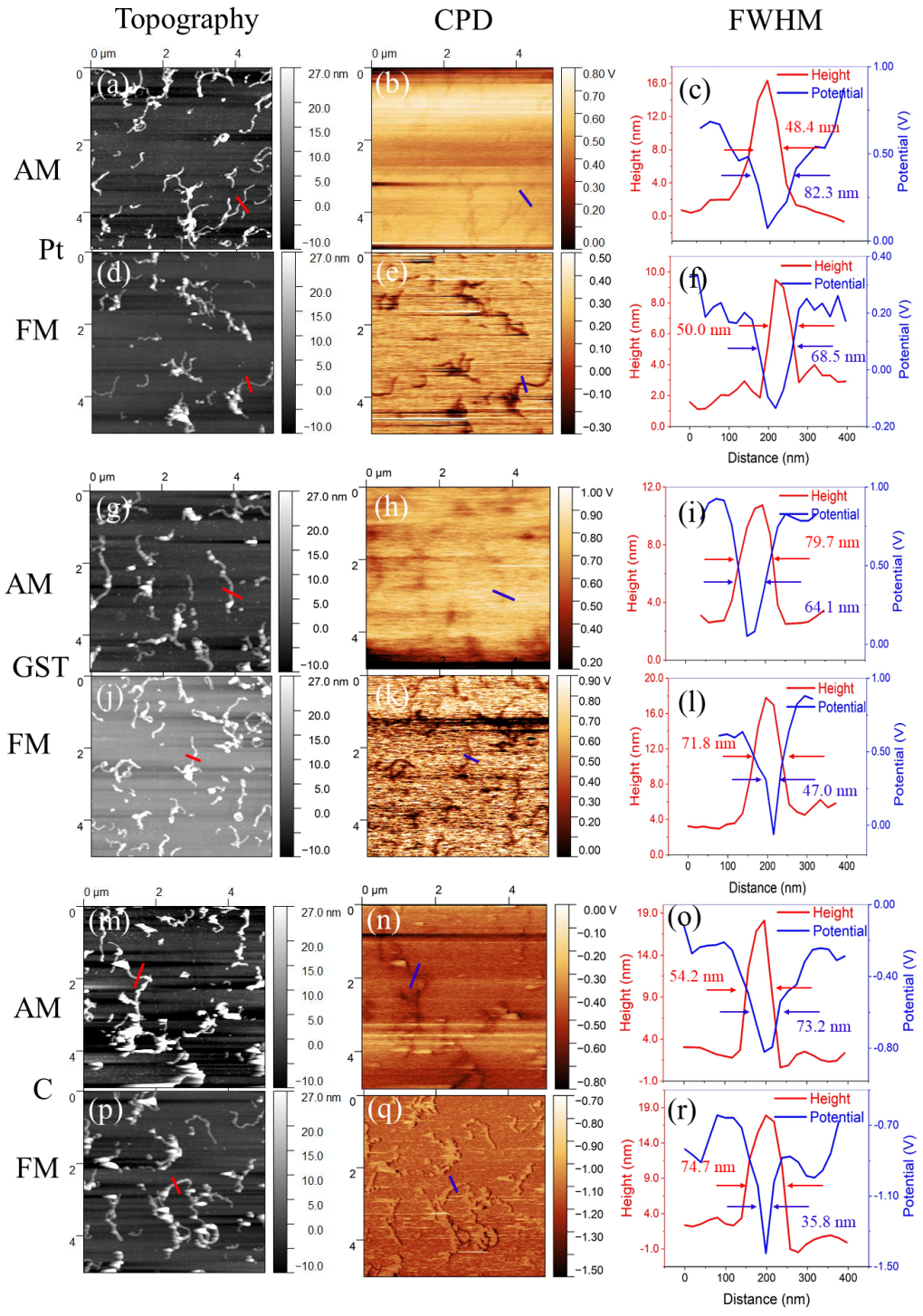


Figure 4.11: Topography, CPD, and the corresponding line sections of scans conducted with (a-f) platinum tips, (g-l) GST, and (m-r) carbon tips with AM- and FM-KPFM on 10 nm diameter carbon nanotubes spray-coated on ITO-substrates.

5 Hollow cantilevers

Contents

5.1 Introduction 73
5.2 Aims of chapter 75
5.3 FluidFM Set-up 75
5.4 Pick and place of 1 μm particles 76
5.4.1 Materials and methods 76
5.4.2 Results and discussion 76
5.4.3 In-situ monitoring 78
5.4.4 Exploring pick and place in air 78
5.5 Nanoprinting 81
5.5.1 Nanoparticle inks 81
5.5.2 Printing quantum dots onto micro- and nano- structures 88
5.5.3 Alignment to structures 91
5.5.4 In-situ monitoring and troubleshooting 94
5.6 Chapter summary 95

5.1 Introduction

The fluidic force microscope or FluidFM combines conventional AFM with microfluidics. The main feature of this tool is the microchanneled AFM cantilever that is connected to a refillable liquid reservoir. This forms a closed and continuous microfluidic circuit. This is in contrast to its predecessors such as dip pen nanolithography and the nanoscale dispensing (NADIS) technique [148, 156]. With

a closed fluidic circuit, solvent evaporation is minimised and less of a concern. Compared to open channels, the closed channels allows for longer experiment times in air and also the possibility to conduct experiments in a liquid medium. Moreover, a pressure controller can be connected to the reservoir enabling the AFM tip to function as a nanopipette for aspiration or dispensing. Furthermore, the nanopippette also benefits from the highly accurate positioning of the AFM system. These features such as the ability to control the pressure to aspirate or dispense, the ability to go to a precise location as well imaging capabilities from the AFM makes this a promising candidate to manipulate particles at the micro- and nano-scale.

As mentioned in the previous chapter (Ch. 4), it was difficult to remove a particle once it has been picked up with a normal AFM tip. However, fluidFM overcomes this problem with its ability to apply an underpressure for aspiration and overpressure for dispensing.

Indeed, the fluidFM has been used for the manipulation of micro-objects. The targeted object is captured by applying an underpressure, transferred to the desired location and released by applying an overpressure. The pressure can be tuned to enable precise and gentle manipulation. An example would be the manipulation of cells demonstrated in Ref. [218, 219].

Besides cells, colloidal particles have been picked up for colloidal force microscopy where single colloid interaction with a substrate is studied in a liquid environment [220]. This technique enables easily exchangeable colloids for rapid variation of different functionalised colloids within the same experiment. The size of colloids that can be picked up depends on the aperture size. Tipless cantilevers with aperture sizes 10 μm and 2 μm were used to pick up 50 μm and 3 μm particles respectively. By being able to control the pressure, it provides a means to dislodge the particles from the AFM tip. The vertical force, F_v, applied on the particle attached depends on the aperture size of diameter, d_0 and pressure, p applied as given by:

$$F_v = \pi \left(\frac{d_0}{2}\right)^2 p \tag{5.1}$$

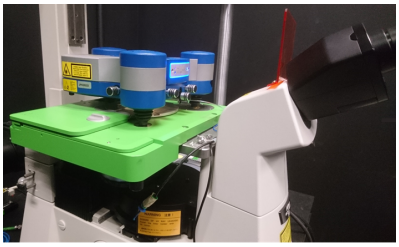
In order to manipulate smaller particles, we consider the 300 nm aperture and a typical suction pressure, p of 800 mbar. The force F_v on the particle is about 6 nN. The previous work by Pablo et al. focuses on micron sized particles, with the smallest being 3 μm, for force spectroscopy purposes [220]. In this chapter, we aim to scale this down with a focus on precise placement on a substrate, rather than simply releasing the particle in solution.

5.2 Aims of chapter

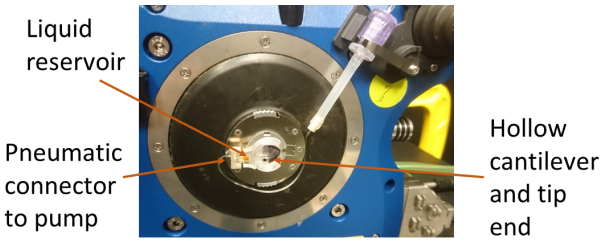
- Demonstrate the ability to pick and place 1 μm particles in a liquid medium.
- Show that different types of nanoparticles can be printed with this technique.
- Develop the technique by demonstrating the capability to image, align and monitor the deposition of nanoparticles in-situ.

5.3 FluidFM Set-up

The main components in the fluidFM set-up are the AFM scanning head, pressure controller and hollow cantilever probe. The AFM scanning head used in this work is the JPK nanowizard 3. The AFM is mounted on an inverted microscope which can be used to align the probe and substrate (Fig. 5.1(a)). The probes are made by fusing two silicon nitride wafers together, producing the microchannel inside. The top side of the cantilever is coated with gold to obtain a good reflected signal. More details about the fabrication process can be found in other articles [221, 222]. There are various probe designs such as a tipless cantilever with an opening at the end or cantilevers with tips. The apertures for cantilevers with tips can be at the side or at the apex of the tip. The height of the microchannel ranges from 0.5 μm to 1.5 μm. The pressure controller is able to provide a constant pressure in the range of -800 mbar to +1000 mbar with 1 mbar precision. The fluid of interest (10 μL) is loaded into the reservoir by means of a micropippete. The controller is connected to the reservoir with tubing and a pneumatic connector (Fig. 5.1(b)).



(a)



(b)

Figure 5.1: (a) FluidFM set up consisting of the AFM on top of an inverted microscope. (b) The probe is connected to an external pump via the pneumatic connector.

After filling the reservoir with fluid, an overpressure of 1000 mbar is applied to push the fluid into the hollow cantilever. In order to determine when the cantilever has been filled, we can monitor the real time difference image as well as the vertical deflection of the cantilever. In figure 5.2(a) and (b), we see the unfilled cantilever and its difference image respectively. Figure 5.2(c) and (d) shows the filled cantilever and its difference image respectively. It is difficult to rely on the optical image alone to see when the fluid has entered the cantilever. Hence, we use the difference image to make this change more obvious (Fig. 5.2(b) and (d)).

5.4 Pick and place of 1 μm particles

5.4.1 Materials and methods

FluidFM probes with an aperture opening of 300 nm in diameter were used in this set of experiments. Silica particles of 1 μm diameter were used (Sigma). The microparticles were diluted in DI water and allowed to settle to the bottom of a glass petri dish. The AFM pick and place experiments were done in this water medium. A suction pressure of -800 mbar was used to pick up the particle and +100 mbar was used to place them after positioning with the AFM.

5.4.2 Results and discussion

Pick and place by applying under- and over-pressure

Figure 5.3 shows the optical image before and after manipulation respectively. Particles outside the boxed region are picked up by applying a negative pressure of

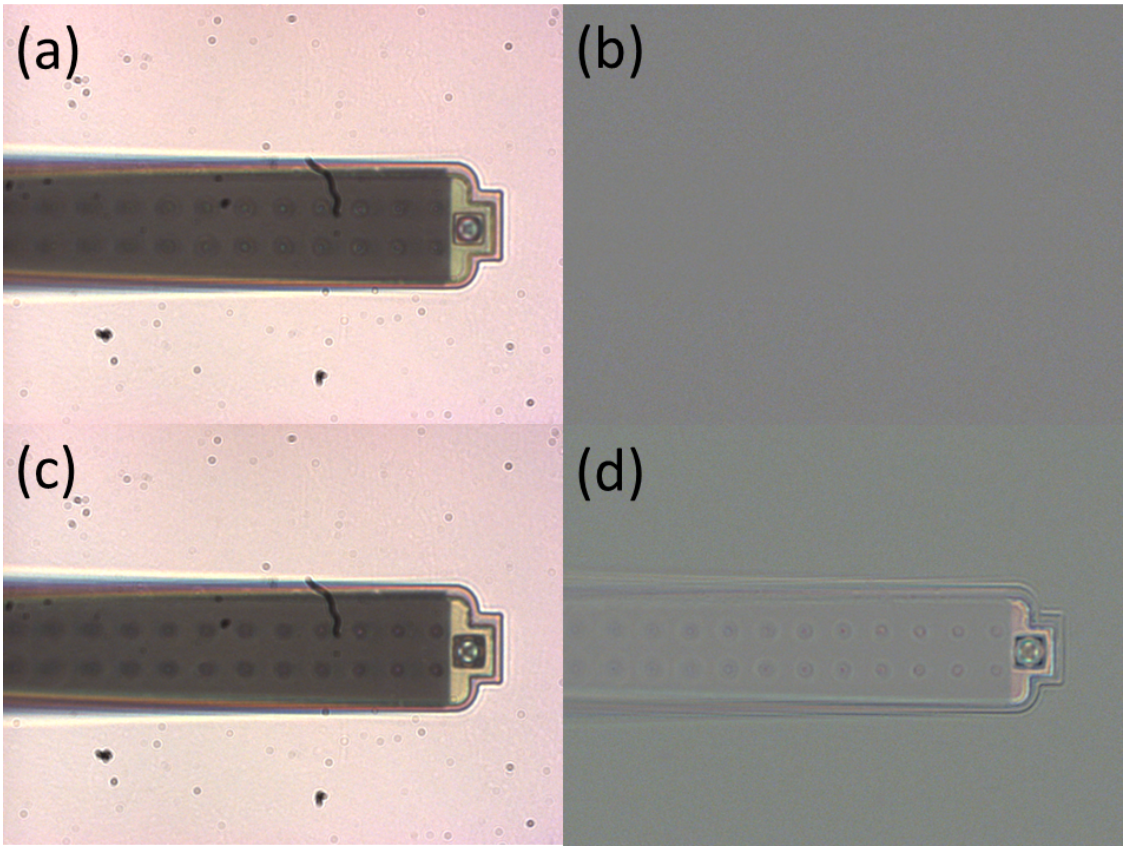


Figure 5.2: (a) Optical image and (b) difference image of tip before filling. (c) optical image and (d) difference image of tip after filling. The contrast is much easier to see in the difference image.

-800 mbar. The tip is then retracted off the surface and moved into the region of interest before coming into contact again at the desired position. An overpressure of +100 mbar is applied to gently release the particle. The tip is withdrawn at the same time and the particle is adhered on the surface by Van der Waals forces. When an overpressure larger than 100 mbar is applied, the particle tends to be pushed out with excess force and float away instead of adhering to the targeted location. The smallest commercially available aperture size is 300 nm. This limits the ability to pick and place particles that are smaller than 300 nm. It is possible to design smaller aperture sizes [223], however it remains a challenge to manipulate smaller particles. The force generated by the pump through a smaller aperture scales with the square of aperture's diameter (Eq. 5.1). Hence, a much larger suction force is required to overcome brownian motion.

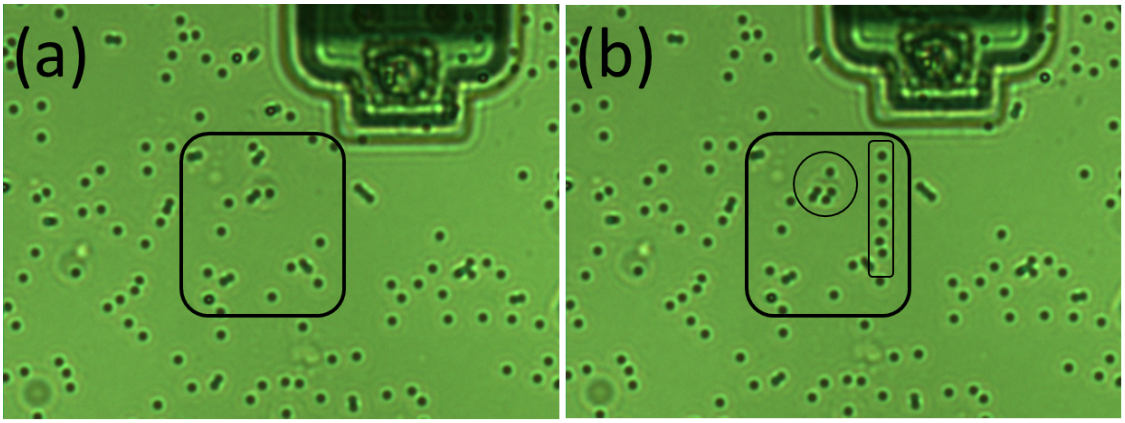


Figure 5.3: Optical image of the substrate (a) before and (b) after pick and place operation. The black boxes outline the region of interests.

5.4.3 In-situ monitoring

It is usually difficult to see optically if we have picked up a particle. However, we can determine that by monitoring it's force curve. Figure 5.4 shows the force curve before and after picking up a 1 μm particle. We note that the z-piezo distance is shifted by about 1 μm, which is the size of the particle picked up. The shift is observed to be slightly less than 1 μm due to the likelihood that the particle has partially entered the aperture which ensures a good seal.

5.4.4 Exploring pick and place in air

We have demonstrated the ability to pick up and place 1 μm particles by applying under- and over-pressures with a hollow cantilever in a liquid environment. Manipulation in liquids reduce the adhesion forces between the particle and manipulator/substrate [224]. This makes it easier to pick a particle from a substrate as well as to remove it from the AFM tip. However, if we are required to dry the substrate, drying artifacts will disrupt the arrangement of particles that are already placed. Hence we explore the feasibility of the same pick and place procedure in air.

However, we were unable to pick up any particles in air. This is likely due to the much larger capillary forces present in an air environment. Figure 5.5 shows a box plot of the adhesion of the probe tip while applying different pressures in air and water on a quartz substrate. Each data point is made up of adhesion

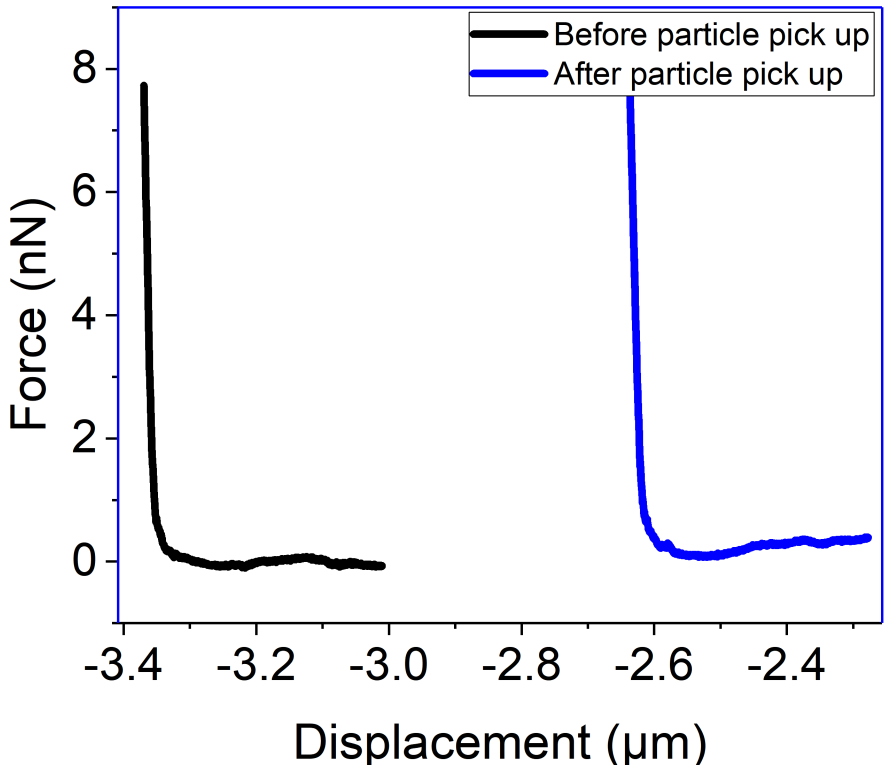


Figure 5.4: Force curves before and after picking up a 1 μm particle.

values from 20 retract force curves. As expected, adhesion values are smaller when an overpressure is applied and larger when an underpressure is applied compared to when no pressure is applied. It is also clear that the adhesion in liquid is at least 1 order of magnitude less than the adhesion in air. We note that the trend does not follow Eq. 5.1 since that equation assumes a good seal of the aperture which is impossible to achieve with a flat substrate compared to a spherical particle. Moreover, the variability in the data can be attributed to the irregular shape of the tip. Nonetheless, the general trend still holds. This liquid environment requirement brings about some limitations for applications. For example, placing particles on functional devices for subsequent measurements to be done in air would require drying of the solvent. This introduces unwanted drying artifacts, such as the coffee-ring and marongoni flow effect, which displaces the already positioned particles. Future work in this direction to overcome drying artifacts could be along the lines

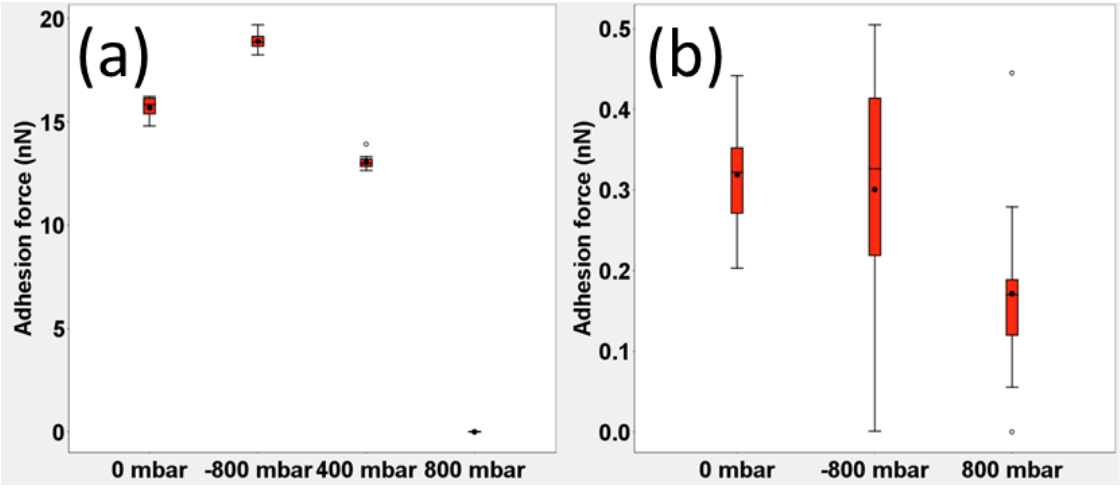


Figure 5.5: Adhesion measured with fluidFM tips in (a) air and (b) water while varying pressure applied. Higher adhesion is generally observed when negative pressures are applied and vice versa. Variability is due to the irregular shaped tip. Adhesion in water is greatly reduced.

of critical point drying, where the solvent is removed at the critical point where there will be negligible surface tension gradient to induce drying artifacts. This is similar to how MEMs devices are prepared. Surface funtionalisations can also be explored too to enhance the adhesion of the particles to the substrate.

Manipulating particles in air would solve a lot of the problems we face in liquid. However, there are a few considerations we should be aware of when working in air. Capillary forces will be present which makes it more difficult to remove particles from surfaces. This capillary force however can be used to our advantage if we are able to control it. The gripping force can be modulated by manipulating the contact angle and thus the meniscus geometry. Various ways to control the geometry have been demonstrated. These include electrowetting [225], by wetting a rod through penetration through a liquid tube [226] and direct control of pressure inside a thin tube [227]. Previous works using capillary force for pick and place are for millimeter or micron sized particles.

Alternatively, filling the hollow cantilever with nanoparticle inks and printing them out directly will enable us to work in air. The fluidFM system allows us to control the volume of liquid dispensed with attoliter accuracy [165]. Hence, the

amount of particles per droplet can be controlled statistically by selecting a suitable particle concentration. This printing technique is investigated in the next section.

5.5 Nanoprinting

FluidFM probes have been used for printing a wide variety of inks. Live cell patterns with different geometries have been patterned covering micrometer and millimeter-centimeter scale areas [228]. Poly-l-lysine (PLL) molecules have also been deposited with this method for guiding cell growth. In these mentioned biological applications, the resolution of printing required is usually in the range of millimters to micrometers.

Due to the functionality of the AFM, the printing method can be used to construct 3D patterns by using layer-by-layer deposition technique [229]. The technique is also able to achieve nanometer scale resolution. Gruter et al. has patterned gold nanoparticles in a liquid medium [230]. By controlling the ionic strength of the liquid environment, they have shown that they are able to control the resulting deposited particle density. They use these deposited particles to form metallic interconnects.

This section aims to showcase the printing method as a means to control the position of nanoparticles placed on a substrate with sub-micron precision. We work towards developing the technique with unique optical applications in mind. We aim to place photo-emitters directly on top of photonic nanostructures. This would have been difficult to achieve using other conventional fabrication techniques. Before achieving this goal, we explore the feasibility and resolution limits of this technique by working with various nanoparticle and fluorescent inks. Moreover, we investigated ways to monitor the deposition process in-situ.

5.5.1 Nanoparticle inks

Choosing the right nanoparticle ink to work with is important. It is an experimental rule of thumb that the particle size should be smaller than 1/10 (and ideally smaller than 1/50) of the nozzle diameter to avoid clogging of the nozzle and prematurely stopping the deposition process [231]. The solvent should also not be too volatile

such that evaporation in the microchannel becomes a problem. The nanoparticles should also be stable in solution and not agglomerate which would also cause clogging issues. Dispersion stability is usually controlled by using surfactants that adsorb on the particle surface. We chose to work with gold nanoparticle inks, fluorescent dyes and quantum dots due to the many possible applications and functionality of these particles. Gold nanoparticles also provide good contrast in SEM which helps greatly for visualisation in the initial studies. Fluorescent dyes and quantum dots can be observed optically with fluorescent imaging, giving a quick indication of whether any particles have been deposited. Moreover, they have various photonic applications. One such example will be discuss in the subsequent sections.

Rhodamine B dye

We started out with using Rhodamine B (RhodB) fluorescent dye. RhodB is often used as a staining dye in biology and have applications in fluorescent microscopy [232]. We chose to start with this ink as they are made up of fluorescent molecules in water. The molecules are much smaller than the nozzle size and hence is less likely to clog the tip. The fluorescence also provide us with an alternative way to visualise the fluid in the microchannel, cantilever and substrate.

We show that we can control the drop size by adjusting the overpressure applied (refer to Fig. 5.6). At 200 mbar of overpressure, we get a droplet size that is about 800 nm in diameter. The smallest feature size we achieve is about 400 nm in diameter. This limitation is due to the size of the 300 nm nozzle and the surface wetting properties. On closer AFM inspection of the droplets, we notice a volcano-shaped structure, with a sharp peak, in the dye deposited (Fig. 5.7). This occurs with ultrasmall droplets and a high ink concentration. The high evaporation rate of ultrasmall droplets works against surface tension and hinders the relaxation of the droplets. Hence, the final geometry of the dried droplet is determined by both the tip and droplet's geometry leading to the sharp peak observed (Fig. 5.7(e)) [233]. For larger drops, we do not observe the sharp peak structure (Fig. 5.8).

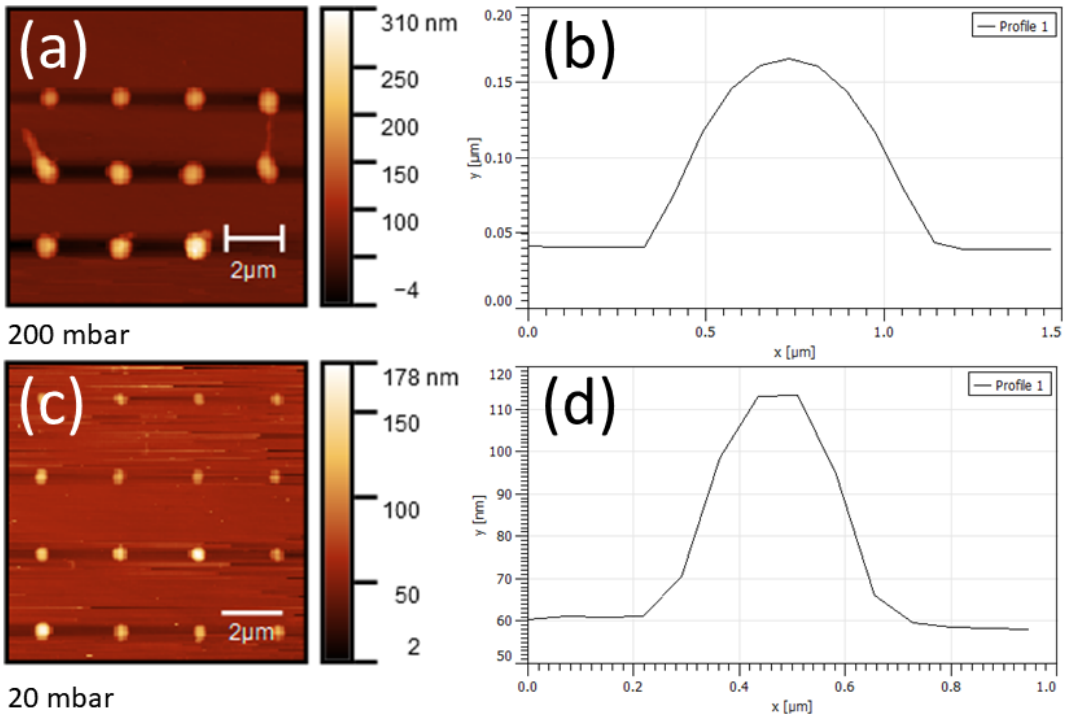


Figure 5.6: (a) AFM image and (b) corresponding line section of rhodamine B dye deposited with 200 mbar overpressure. (c) AFM image and (d) corresponding line section of rhodamine B dye deposited with 20 mbar overpressure. Deposition droplet size can be controlled by varying overpressure.

Gold nanoparticles

We also tried depositing gold nanoparticles. The number of particles per droplet depends on the concentration of gold particles as well as the droplet size.

We can estimate the rough volume deposited by assuming a spherical dome cap shape; $V = \frac{1}{3}\pi h^2(3r-h)$, where r is the radius and h is the height of the dome. Using Fig. 5.6 as an estimate, we can estimate a volume in the femtoliter range [234]. Hence, we can achieve single or few particles per droplet by adjusting the concentration. We use AuNP solution with a concentration of 10^{11} particles/ml. Other factors that can affect droplet size includes surface contact time and surface wetting properties.

Figure 5.9 shows the gold nanoparticle droplets on a clean gold coated surface. We see that the droplet size is much larger than the nozzle size as the solution wets the hydrophilic gold surface. We observe more particles per droplet and they are concentrated in the central region of the droplet.

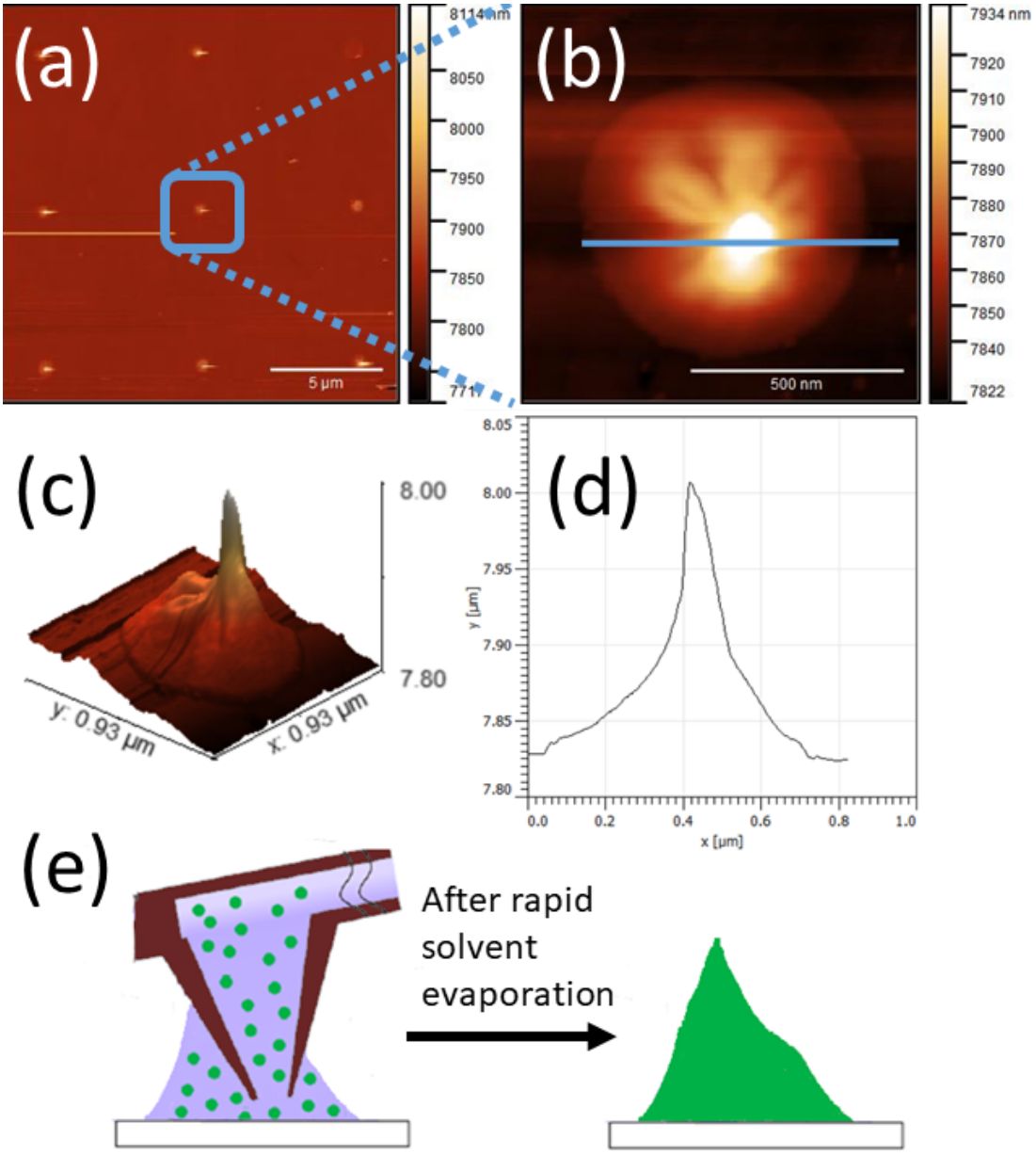


Figure 5.7: (a) AFM image of the overall region. (b) zoomed in image on one of the dye droplets showing the volcano shaped structure. (c) 3D view of the volcano-shaped structure and (d) corresponding linere cross-section. (e) Schematic showing how the final geometry is determined by the droplet wrapping around the tip in fast evaporating droplets.

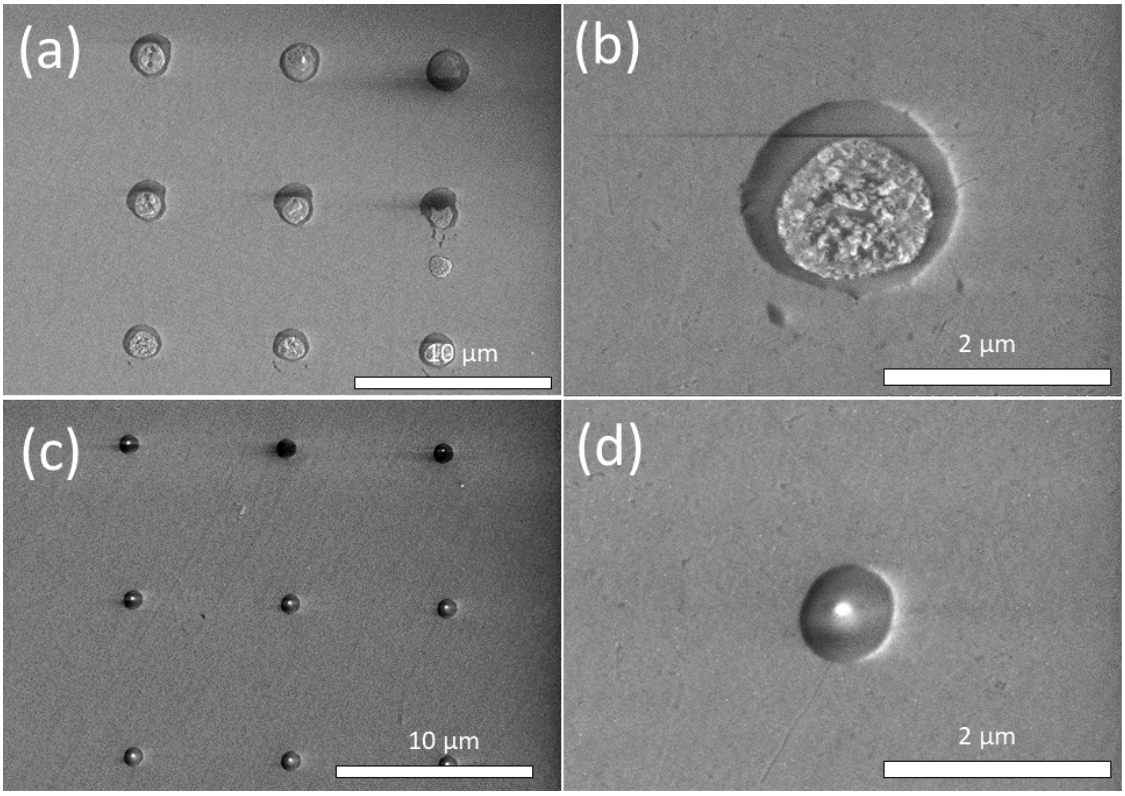


Figure 5.8: (a) SEM image of overall region and (b) zoomed in region of larger dye droplets. (c) SEM image of overall regions and (d) zoomed in region of smaller dye droplets exhibiting the volcano shaped structure.

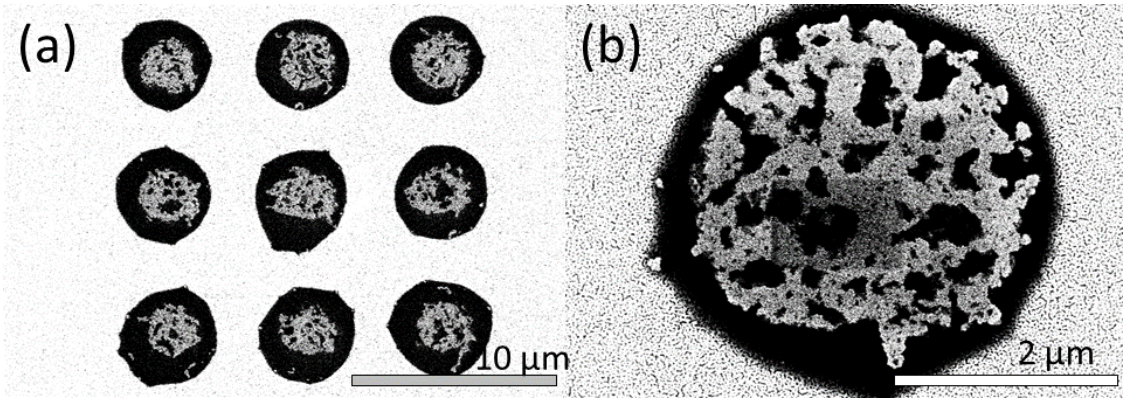


Figure 5.9: (a) AuNP droplet on gold coated substrate. Large drop due to the wettability of the substrate.

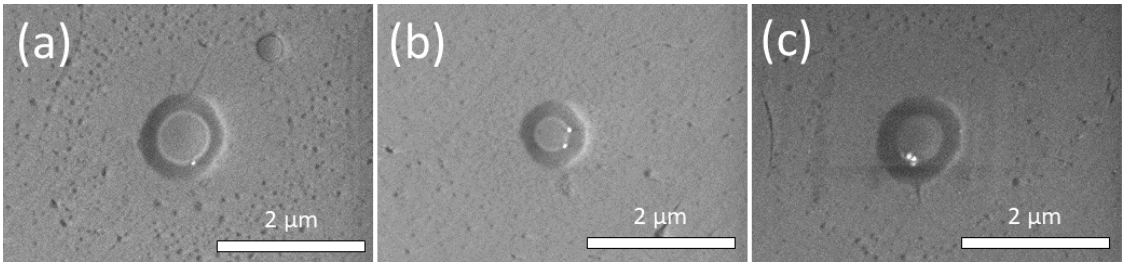


Figure 5.10: (a-c) Various examples of droplets with few to single AuNP per droplet on quartz.

Figure 5.10 shows gold nanoparticle droplets on quartz. The smallest droplet size we can achieve on quartz is about 500 nm. The droplets obtained on quartz is generally smaller due to a it being less hydrophilic than a clean gold substrate. Using a concentration of about 10^{11} particles/ml, we see that there are few to single gold nanoparticles confined within the 500 nm region of the droplet.

Quantum dots

Quantum dots are semiconductor nanoparticles. Due to their small size, electrons and holes are tightly confined, leading to discrete energy states, similar to atoms. When quantum dots are excited by UV light, an electron in the quantum dot can be excited to a higher energy state. When it drops back into a lower energy state, its energy can be released in the form of emitted light. The wavelength of this emitted light is dependent on the size and shape of the quantum dot. Larger quantum dots emit longer wavelengths, while smaller quantum dots emit shorter wavelengths. Quantum dots have found a wide range of applications such as LEDs [235], photonic applications [236] and medical imaging [237].

Quantum dots are attractive for photonic applications due to the ease of tuning their spectral position of emission and absorption by tuning particle size. In contrast to organic dyes, their absorption increases at shorter wavelengths and have a narrow emission band that is mostly symmetric, thus avoiding cross talk [238].

The precise placement of quantum dots is often required to realise many optical applications. For example, the use of QDs as emitters to demonstrate the highly directional antennas for light [239].

Table 5.1: Comments on printing of different types of QDs in various solutions.

Quantum Dot Inks		
Quantum Dot	Solvent	Comments
Copper Indium Sulphite/Zinc Sulphite	Hexane	Hexane evaporates too quickly.
Copper Indium Sulphite/Zinc Sulphite	Hexanol	Dimmer due to ligand exchange.
Cadmium Telluride	Water	Oxides resulting in blue-shift of spectrum.
Cadmium Selenide/Zinc Sulphite	Water	Relatively bright and emits at the expected wavelength.

We have tried printing various QD inks with various success rates. We take into consideration various ink parameters such as solvent volatility and particle stability, among others. The results are summarised in Table 5.1.

QDs are commonly available in organic solvents like toluene and hexane. However, due to their high volatility, evaporation from the microchannel becomes an issue. When the solvent quickly evaporates, air bubbles become trapped in the channel and clogs it. Printing of highly volatile solvents is possible, however the experiment has to be done within a shorter period of time before a significant amount of solvent in the microchannel starts to evaporate. Therefore, we carried out a phase transfer method (prepared according to Ref. [240]) to change the solvent from hexane to hexanol which is a much less volatile solvent. However, that resulted in dimmer emission. We hypothesize that this is due to the ligand exchange process. We also tried with Cadmium Telluride (CdTe) QDs in water (PlasmaChem). The QDs are stable in water and remains bright after deposition. However, we noticed a blue-shift in the spectrum (Fig. 5.11). We only observed this on the small droplets. The emission is at the expected wavelength in a dropcasted solution (both wet and dried). We believe that the blue-shift is due to oxidation of CdTe as tellerium based QDs are prone to oxidation [241]. The oxidation process is sped up especially in the small droplets due to their high surface to volume ratio

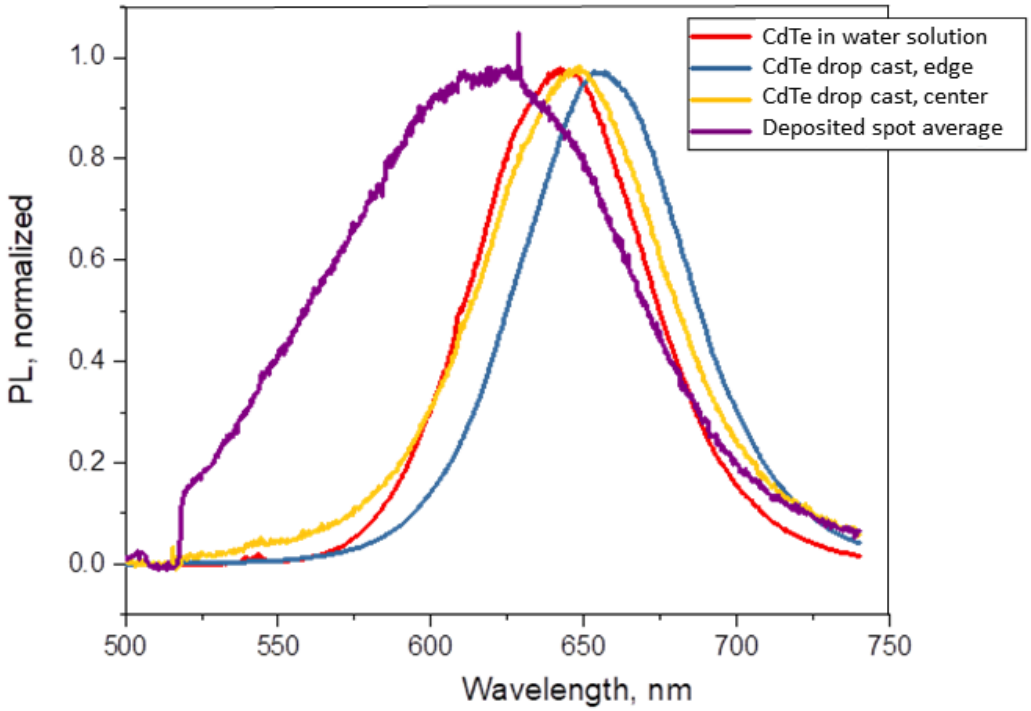


Figure 5.11: Spectrum of CdTe in water solution, the center and edge of a dried dropcasted solution and a spot deposited using FluidFM probes.

resulting in a lot of exposed area for oxidation. In order to reduce the problem of oxidation, QDs can be capped with a core shell layer. We use CdSe QD with a core shell of ZnS (prepared according to Ref. [242]). The core shell acts as a protective coating preventing the QDs from being oxidised [243]. CdSe/ZnS QDs is stable in water, is relatively bright and emits at the desired wavelength without any blue-shifting due to oxidation. Due to these desirable properties, we mainly focus on the use of CdSe/ZnS for our subsequent applications.

5.5.2 Printing quantum dots onto micro- and nano- structures

Micro array for microLED applications

Quantum dot based light-emitting diodes (LEDs) are highly desirable due to the flexibility of colour tuning by controlling QD core size, high colour purity, narrow emission bandwidth and high brightness [244, 245]. An important step for creating

high resolution microLEDs for applications such as augmented reality require precise positioning and patterning techniques of quantum dots. Kim et al. has demonstrated the filling of solid patterns (e.g. 30 x 30 μm squares) using electrohydrodynamic inkjet printing. They are able to reduce the size to circular deposits of several microns (4 μm) using a pulsed drop-on-demand mode [246]. E-beam patterning of QDs is another method used to achieve arrays of patterns ranging from 1 to 10 μm [247]. Moreover, using two-photon lithography, Mayer et al. has shown that lines up to 75 nm in width can be written [248].

Using the fluidFM technique to print QDs, we show that we can align and print QDs into an array structure which can be used for microLED fabrication. The advantage of this technique is the ease of conducting the experiment in ambient environment without the need for vacuum processes or submerging the substrate in photoresist which would be practically difficult for LED circuits.

Figure 5.12 shows the results of QDs being printed into an array structure that is fabricated with e-beam lithography. Figure 5.12(b) shows the corresponding optical image with the region that is filled highlighted by the black box. The AFM image and line section indicates that the well is fully filled. The array has wells of 2 μm in diameter and a pitch of 4 μm. The alignment is done optically.

Printing quantum dots on nanoantenna pillars

Optical antennas convert propagating optical radiation into localised energy and vice versa. They enable the control of light at the nanoscale and have applications in enhancing the efficiency of photodetection [249], light emission [250] and sensing [251]. Optical antennas can be made out of metallic or dielectric resonant nanostructures. Dielectric antennas are advantageous over plasmonic counterparts due to their low-loss and ability to support both electric-like and magnetic-like Mie modes. The interaction of these modes allow the tailoring of directional radiation patterns. Mie resonances in the dielectric nanoantenna are able to increase the local density of electromagnetic states thus enchancing light emission via the Purcell effect [252].

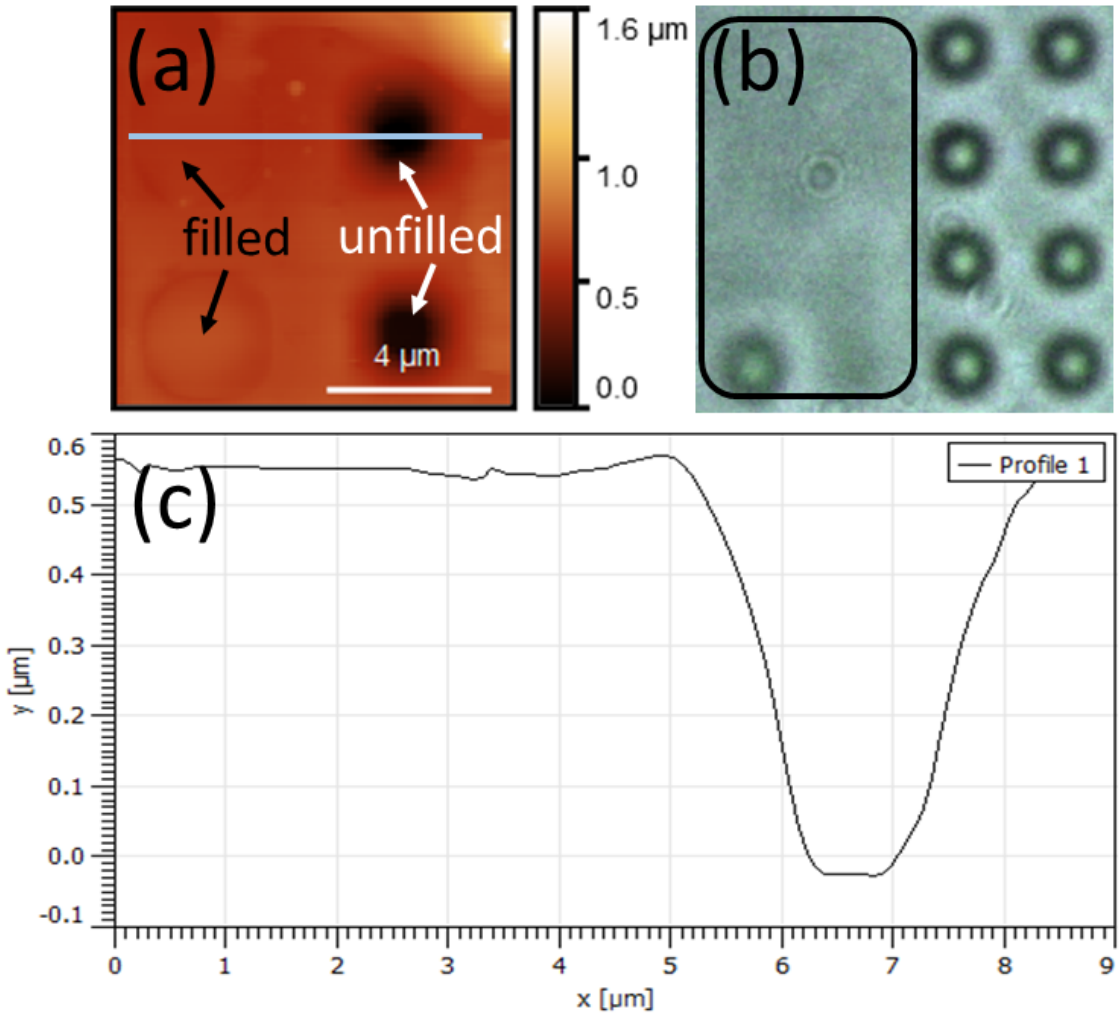


Figure 5.12: (a) AFM image showing that the well is completely filled. Its corresponding (b) optical image and (c) line section.

Placing emitters onto these antenna structure is difficult yet required to experimentally characterise the emission and directionality of an antenna design. Quantum dots can be directly patterned precisely with the use of extreme UV and electron beam lithography [253, 254]. However, exposure to UV causes the photoluminescence quantum yield to decrease by 20-50% [253]. Single QD positioning with a combination of electron beam lithography and chemical functionalisation have been achieved by Curto et al. [239].

In this section, we show that we can reliably use a cytosurge tip to place a droplet of QD emitters on top of nanoantenna pillars in ambient conditions (fabricated by electron beam lithography according to Ref.[255]). Placing emitters on top

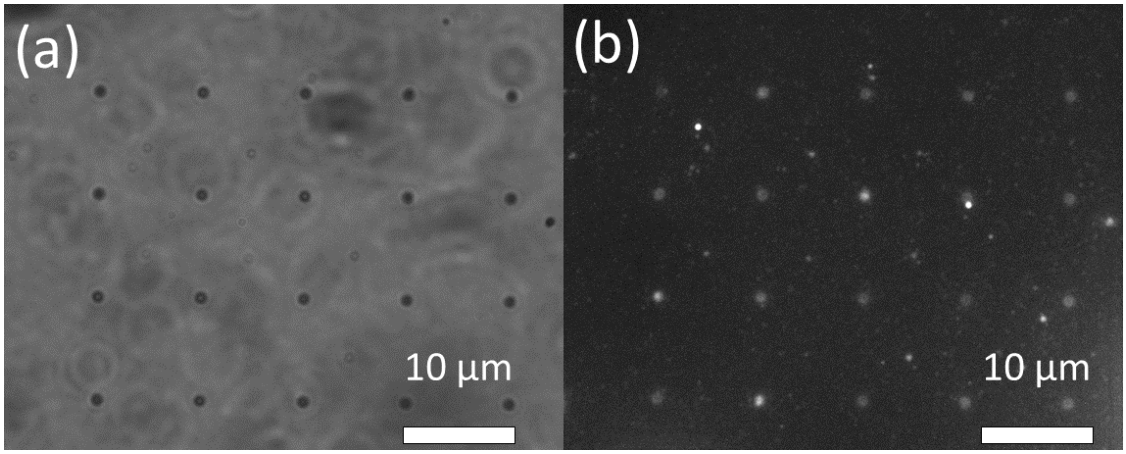


Figure 5.13: (a) Optical image and (b) photoluminescence image of an array of nanoantenna pillars with QDs printed on them.

of such pillar structures is challenging with conventional lithography techniques. Moreover, it would be impractical to use the push and pull techniques of AFM particle manipulation. Although this technique does not achieve single QD precision, it avoids the use of vacuum processes, multiple alignment steps and complicated lift-off processes. It also prevents photobleaching of the QDs when exposed to UV or electron beams and allows the use of variety of quantum dots that might be sensitive to beam exposure.

Figure 5.13 shows the optical and photoluminescence image of the array of nanoantenna pillars filled with QDs. We can see that the QDs are well aligned over tens of micrometers.

To verify the precision, we took AFM images of the nanoantennas after deposition. Figure 5.14 shows AFM images of nanoantennas before and after QD deposition. We see that the deposition is well localised within the antenna structure. The well-shaped structure of the antenna also prevents the spreading of the QDs on the surface (i.e. it provides a means to localised the deposited ink).

5.5.3 Alignment to structures

For structures large enough to see under the microscope, optical alignment of the tip and the structure can be done. However, for sub-micron structures such as the nanoantennas seen in the previous section, the ability to image the

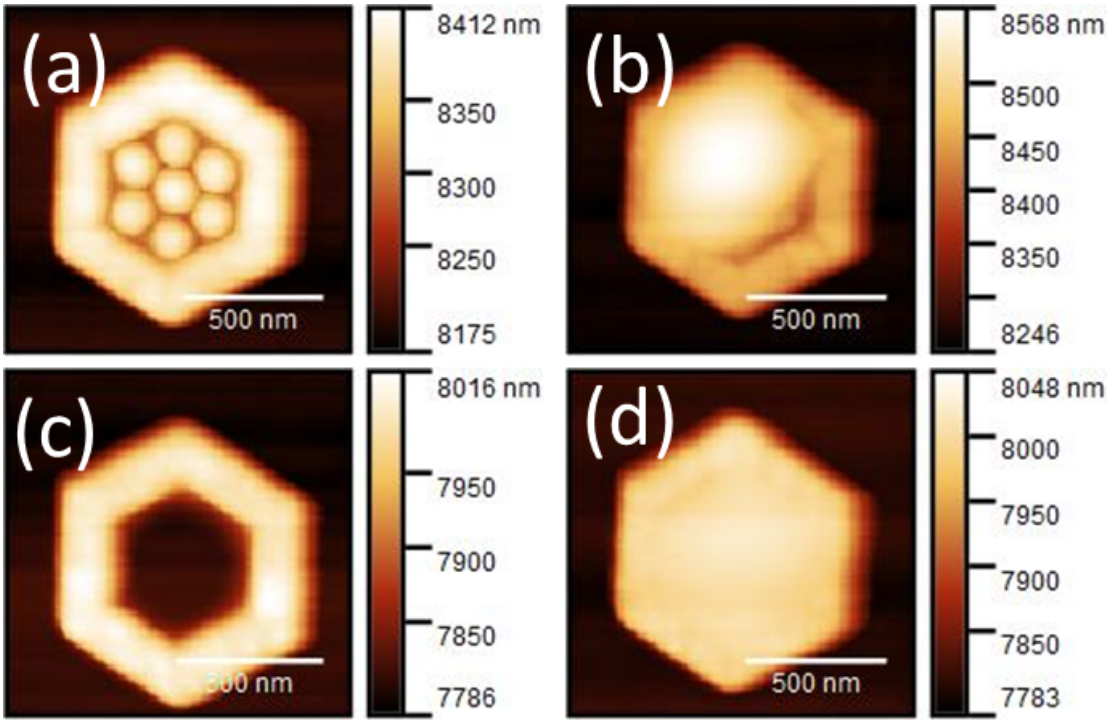


Figure 5.14: AFM images of two different types of antenna structures. (a) and (c) shows the antenna before QD deposition while (b) and (d) shows the corresponding image after QD deposition.

structures beforehand would result in higher precision when depositing. With these hollow cantilevers, we are unable to use the usual tapping mode or contact mode. Since the tip has an aperture at the end that is filled with liquid, any contact or intermittent contact with the substrate will result in deposition of the fluid. Therefore, we investigate the use of non-contact imaging methods in-situ with these hollow cantilevers.

We coat the cantilever with gold and apply a bias between the cantilever and the substrate. In figure 5.15, we compare the force curves when a voltage is applied between the probe and substrate. We applied a 5V bias on gold substrate and a 10V bias on quartz. We see from the vertical deflection force curves that there is an attractive force experienced by the cantilever as the tip approaches the surface due to the bias applied. In the amplitude force curves, we see that we get a better slope contrast with bias applied compared to without a bias applied. The large decrease observed in the amplitude when no bias is applied indicates that a snap-in has

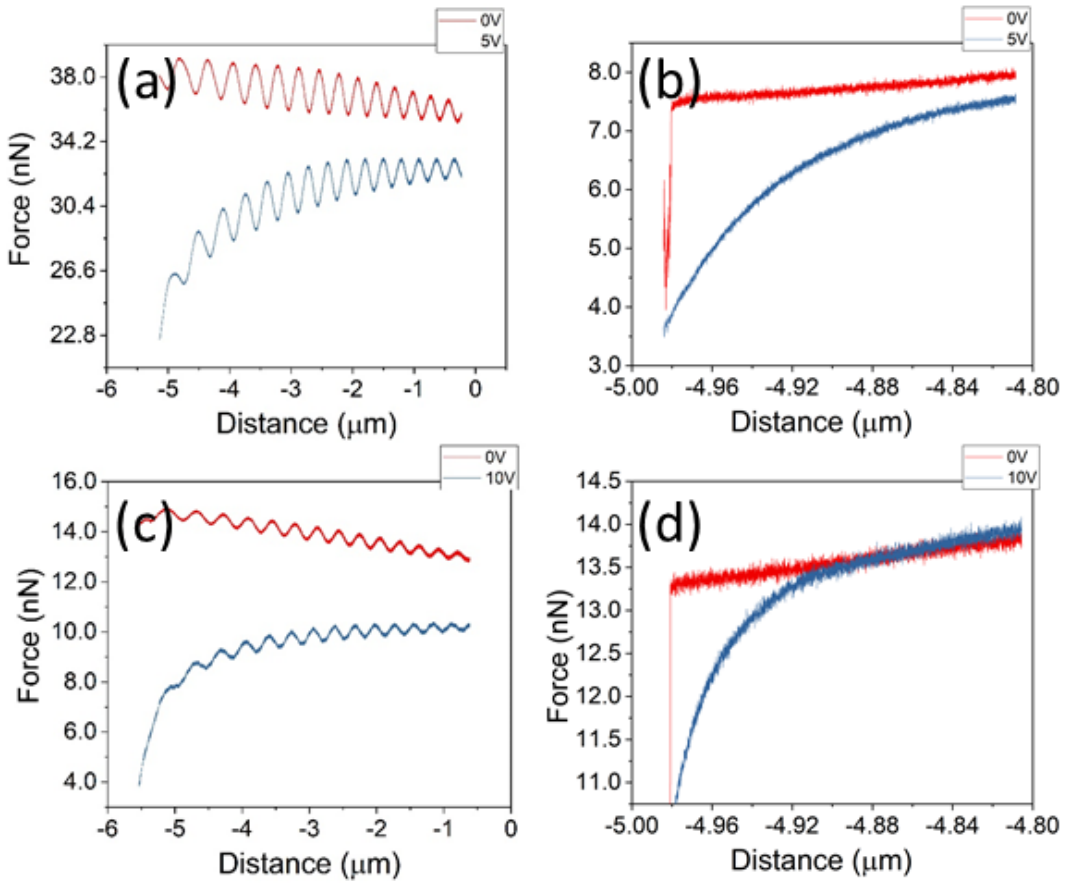


Figure 5.15: (a) Vertical deflection on Au substrate. (b) Amplitude on Au substrate. (c) Vertical deflection on Quartz substrate. (d) Amplitude on quartz substrate.

occurred. This occurs when the tip with a liquid droplet at the aperture contacts the surface resulting in snap-in, which is what we wish to avoid to prevent deposition while imaging. We see the change in slope contrast when applying a bias on both gold and quartz substrate. This means that we can do non-contact imaging on quartz by biasing the tip and relying on surface charge of the quartz.

Figure 5.16 shows the AFM image of the nanoantenna array taken using a filled fluidFM probe in non-contact mode. No deposition was observed in this non-contact mode. The double image observed is due to the irregular shape of the aperture at the tip.

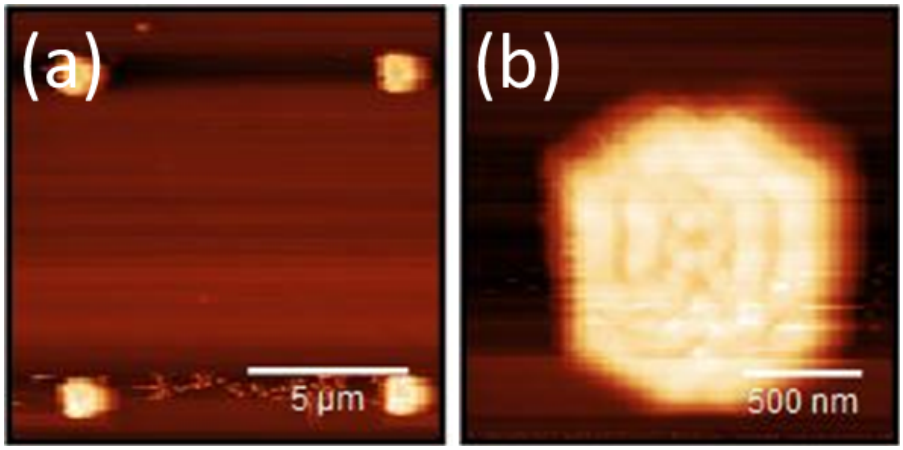


Figure 5.16: (a) AFM image of a region of nanoantennas taken with a filled fluidFM probe in non-contact mode to and (b) its corresponding zoomed in image.

5.5.4 In-situ monitoring and troubleshooting

Is the probe clogged?

The hollow cantilever and aperture is prone to being clogged with extended usage, especially when depositing nanoparticle solutions. It is advisable to use particles with diameters that are at least 10 times smaller than the aperture size (i.e. 300 nm). Hence, it is crucial that we have a method to determine if the probe is working as intended and whether anything has been deposited.

By observing the vertical deflection of the cantilever as a function of z-piezo distance or pressure applied, we can determine whether the probe is clogged or not. Figure 5.17 shows the case of a new probe and how its vertical deflection changes with different applied pressures from 0 mbar to 800 mbar to -800 mbar and back to 0 mbar with intervals of 200 mbar. There will be little to no response in vertical deflection to pressure if the aperture is clogged. This signature behaviour can be observed in both air and liquid medium. Hence, monitoring the vertical deflection while applying various pressures can be a useful way to determine if the probe is clogged or not.

Is anything printed?

It can be difficult to observe optically whether anything has been printed. Hence, it is important that we have an in-situ method to determine whether we have ejected fluid from the aperture to the substrate. This can be done by monitoring

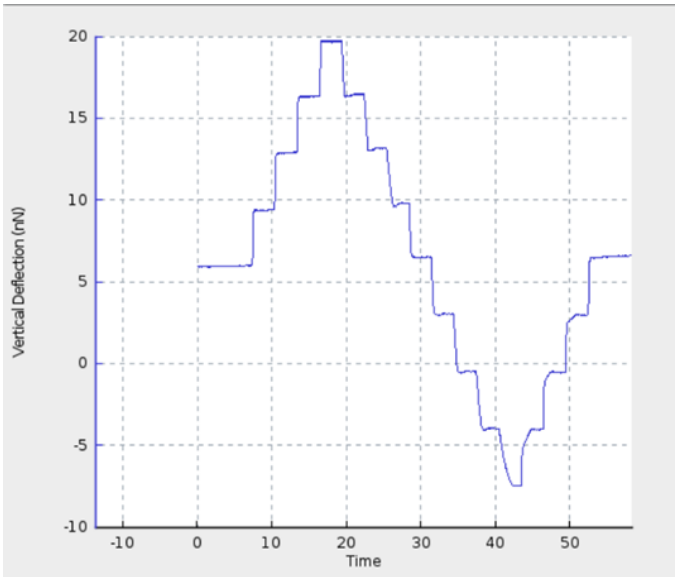


Figure 5.17: Vertical deflection of the cantilever vs time. The pressure applied to the reservoir is adjusted every 3s from 0 mbar to 800 mbar in increments and decrements of 200 mbar.

the force curve simultaneously as we deposit. When fluid is successfully deposited, we consistently observe a clear difference in the retract curve, compared to when nothing is deposited. It appears that the tip is pulling out of a compliant object. We believe that the solvent has mostly evaporated in this case as we would expect to see a large capillary force if tip is pulling out of the solvent. In cases where we deposit a large drop of fluid, we observe a significantly larger adhesion then when no fluid is deposited. In any case, we can determine if fluid has been deposited, even very tiny amounts, by monitoring the retract curves.

5.6 Chapter summary

In this chapter, I show that we can manipulate micro- and nano-particles through the use of hollow cantilever probes. We have successfully picked up and placed 1 μm particles in water. However, evaporation of the water causes drying artifacts which disrupts the position of the particles after placement. To overcome this issue, we explored the option of filling the cantilever with nanoparticle solutions and directly printing them out in air. I show that we can create sub-micron sized droplets and align this droplet directly on top of a micrometer array structure and

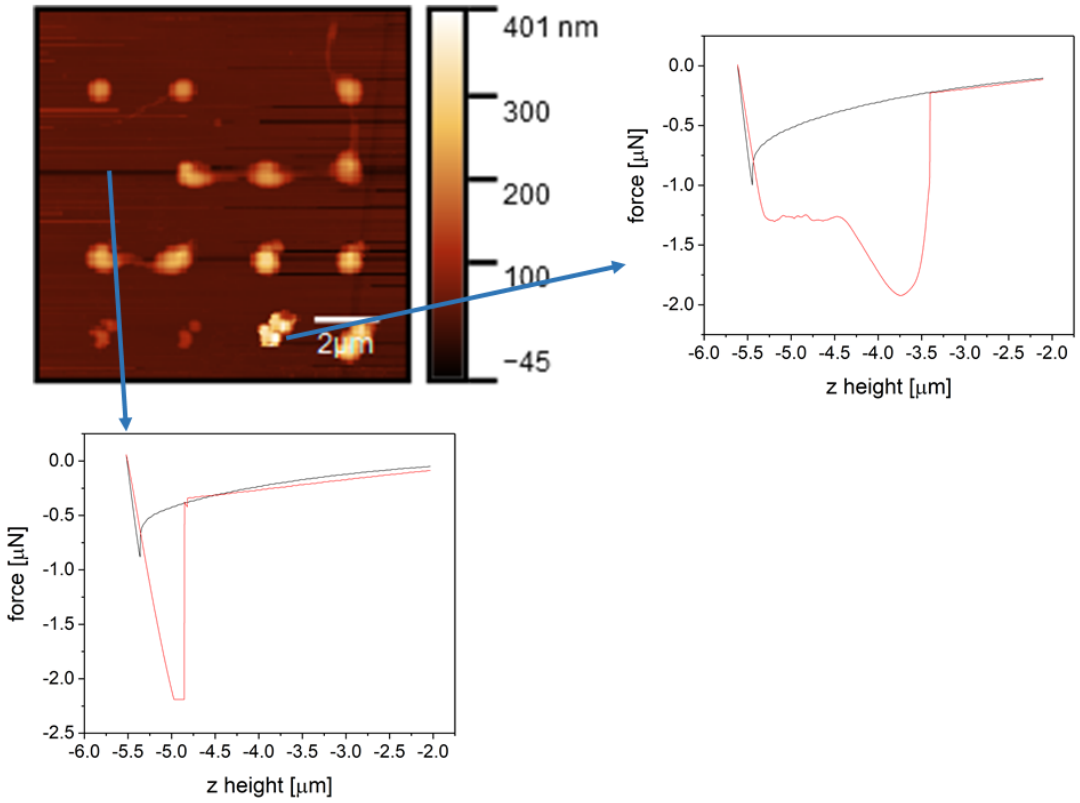


Figure 5.18: This figure shows an array where some dots are deposited, while others are not. We notice a clear difference in the retract curves.

sub-micrometer nanoantenna pillar structure. Furthermore, by observing the force curves, we can know if we have successfully picked up a particle or deposited a drop in real time. This is especially crucial when working with sub-micron particles or droplets that are difficult to visualise optically. We have developed a technique to position particles precisely on sub-micron pillar structures as well as monitor its process in-situ. This technique allows us to study the interaction of various types of optically active nanoparticles with photonic structures.

Author Contributions

Preliminary experiments on microparticle pick-and-place were conducted in Cytosurge, Zurich with the support of Pablo Dörig and Paul Monnier. The quantum dot inks were prepared by Darren Neo (Institute of Materials Research and Engineering, A*STAR). The nanoantennas were provided by Ding Lu (Institute of Materials

Research and Engineering, A*STAR). The particle manipulation, printing and in-situ monitoring ideas and experiments were conducted by me.

6

Tipless cantilevers for picking up EGaIn droplets

Contents

6.1 Introduction 100
6.2 Aims of chapter 100
6.3 Background 101
6.3.1 EGaIn and its manipulation techniques 101
6.3.2 EGaIn as a technique to make molecular junctions . . . 102
6.4 Materials and Methods 103
6.4.1 Creating EGaIn droplet probes 103
6.4.2 Substrate preparation 105
6.4.3 Self-assembly 105
6.5 Characterisation of EGaIn droplet probes 105
6.5.1 Surface roughness of picked-up EGaIn droplet 105
6.5.2 Contact mechanics of EGaIn droplets 107
6.5.3 Crack formation in millimetric-sized droplet 112
6.5.4 The effect of oxide for electrical measurements 113
6.6 Benchmarking on alkanethiol SAMs 114
6.6.1 Stability of droplet probe 117
6.7 Chapter Summary 117

6.1 Introduction

In this chapter, we show that we can manipulate a liquid metal (i.e. eutectic Gallium-Indium (EGaIn)) microparticles/droplets [1] in an AFM. As the particles we work with here are in the micrometer scale, we can monitor its manipulation optically without the need for indirect in-situ monitoring techniques that we have discussed in Chapter 5.

We fabricate EGaIn microdroplets which can be picked up and removed at will with the use of a tipless AFM cantilever. We show that these microparticles are smooth at the nanoscale. The use of AFM enables nanometer scale precision in the three spatial dimensions. Furthermore, it allows precise control over the force applied. Moreover, the behaviour of the wetting properties of the droplet, and hence the contact area, can be tuned by changing its environment (e.g. air, ethanol). We demonstrate an application of EGaIn droplet probes in molecular electronics by making small, well-defined (typically $\sim$4 – 12 μm^2) molecular contacts on SAMs. Extracts of this chapter will be published in a journal paper.

6.2 Aims of chapter

- Showcase a technique to create smooth and spherical EGaIn particles which can be picked up and released by an AFM cantilever at will.

- Shed light on the contact mechanics and physical properties of EGaIn particles during manipulation.

- Demonstrate that these probes have applications in the study of molecular behaviour.

[1] We will use both EGaIn microparticles and droplets interchangeably. This is to emphasize that the EGaIn particles are liquid. It is also more natural to refer to them as droplets when discussing wetting properties.

6.3 Background

6.3.1 EGaIn and its manipulation techniques

EGaIn is an electrically conductive liquid metal alloy of Gallium and Indium (approximately 15% In and 85% Ga) with a melting point of 15°C. It is non-toxic, has high electrical and thermal conductivity and deformability [256]. The manipulation of its geometry, precise positioning and alignment of EGaIn onto substrates is of significant interest to create functional electrical and optical components that are stretchable, soft and deformable [257]. As such, EGaIn has broad applications in flexible and self-healing electronics [258–260], plasmonics [261, 262], 2D-materials synthesis [263], and molecular electronics [264]. Although a fluid at room temperature, it behaves like an elastic solid at low surface stresses but flows readily when enough surface stress is applied. This interesting behaviour is mainly due to a thin ($\sim$ 1 nm) layer of oxide skin that is composed mainly of gallium oxide [265]. This oxide skin confines the liquid gallium-indium alloy beneath it. Moreover, the oxide skin lowers the surface tension of the metal [266] and also enables EGaIn to be moulded into various well-defined geometric shapes such as spherical micro and nanoparticles [267, 268], nanorice [269], nanorods [269] and conical shapes [270]. The geometry of EGaIn determines its efficiency and function in the various applications. For example, EGaIn nanorice shows enhanced photothermal conversion efficiency compared to nanosphere and nanorod structures [269].

Besides manipulation of its geometry, precise positioning and alignment of particles onto substrates is of significant interest. With the addition of magnetic nanoparticles, gallium and EGaIn alloys can be manipulated using magnetic fields [271–273]. EGaIn can also be patterned onto substrates based on pre-defined structures from lithography. For example, line traces of EGaIn with micrometer sized line width and sub-micrometer depth have been patterned via an imprinting technique using polymer molds (e.g. polydimethylsiloxane, PDMS) [274]. Similarly, EGaIn can also be injected into microchannels [264, 275, 276]. These lines can serve as conducting wires for soft matter electronics. Patterning and manipulating the

shape of EGaIn is not limited to planar substrates. Ladd et al. used 3D printing of EGaIn to directly fabricate free-standing microstructures such as towers and bridges made of EGaIn [277]. Many of these techniques to manipulate liquid metal are in the millimetre or micrometer scale with no counterpart at the nanometer scale.

6.3.2 EGaIn as a technique to make molecular junctions

The study and understanding of molecular electronics is largely driven by the need to find ways to improve and shrink current electronic technologies. In general, the field involves advances in synthesis of molecules with functional electronic properties and methods to make electrical contact to molecules. This can be either integrated in a device or in a conductive probe set-up. The reliability and reproducibility of electronic transport measurements through molecular junctions is heavily dependent on the methods used to contact the molecules. The challenge lies in making reproducible contacts between the electrode and the molecule, and the ability to measure the contact area to determine the current density.

Generally, contact techniques can be classified into single-molecule and ensemble contacts. For single-molecule contact, the break junction technique is commonly used. It was demonstrated by Tao et al. using the scanning tunnelling microscope (STM) [278, 279]. In STM, the current is used as a feedback signal to control the tip position as well as to measure the electronic properties of the molecule. This convolution makes the position of the probe with respect to the molecules ambiguous, which may result in the penetration of the tip into the self-assembled molecular monolayer. In comparison, the AFM uses force feedback, hence the tip position and electronic transport can be measured independently as demonstrated by Wold et al. [280]. For ensemble contacts, we contact many molecules, self-assembled onto a surface, simultaneously. As a result, we lose single-molecule effects but gain reproducibility. Evaporating metallic electrodes onto the monolayer is one way to contact a large number of molecules. However, in this process the metal evaporated often penetrates the monolayer, thus creating metallic filaments and causing short circuits. This results in very low yields [281, 282]. Sandwiching electrically conducting polymers

in between the metal and SAM prevents the formation of metallic filaments [283, 284]. However, high temperatures are also required to anneal most polymers which could damage the SAMs. Moreover, liquid metals such as Mercury and EGaIn have been used to create soft contacts [285, 286]. EGaIn has the added advantage of being non-toxic as well as having a thin native oxide shell that reduces shorting of molecular junctions, hence improving the yield [287]. Conical tips can be made using EGaIn in a syringe and a micromanipulator with diameters ranging typically from 10 to 100 µm. However, the lack of force control and rough surface of the EGaIn top electrode introduces uncertainty in the contact area [288].

In addition, the native oxide reduces the electrical coupling between the molecule and the electrode compared to a direct molecule/metal interface. This is appealing as it enables functional transport in the molecule. This technique does not broaden the molecules' energy structure, thus allowing charge carriers to have a sufficient lifetime in the molecules for proton-electron interaction, ion migration, etc. [289, 290]. However, in the single/few-molecule regime, it is challenging to produce weakly-coupled junctions. In break junctions, one of the electrodes would have to be mechanically adjusted to a position where the coupling is reduced. There is currently no equivalent to the EGaIn technique producing stable, weakly coupled junctions in the single or few molecule regime. We propose using these EGaIn microdroplet probes as a controllable way to form mechanically and electrically stable junctions with few molecules.

6.4 Materials and Methods

6.4.1 Creating EGaIn droplet probes

We prepare EGaIn microdroplets from the bulk EGaIn by ultrasonication. The EGaIn droplet sizes can be controlled depending on the ultrasonication time [291]. 0.18 g of EGaIn is sonicated in 0.75 ml of ethanol for ∼30 min forming a greyish emulsion. The oscillating shear forces during ultrasonication generate polydisperse droplets that range from sub-micron to tens of microns in diameters. Ultrasonication causes the thin oxide envelope of the EGaIn to fracture and the liquid metal to

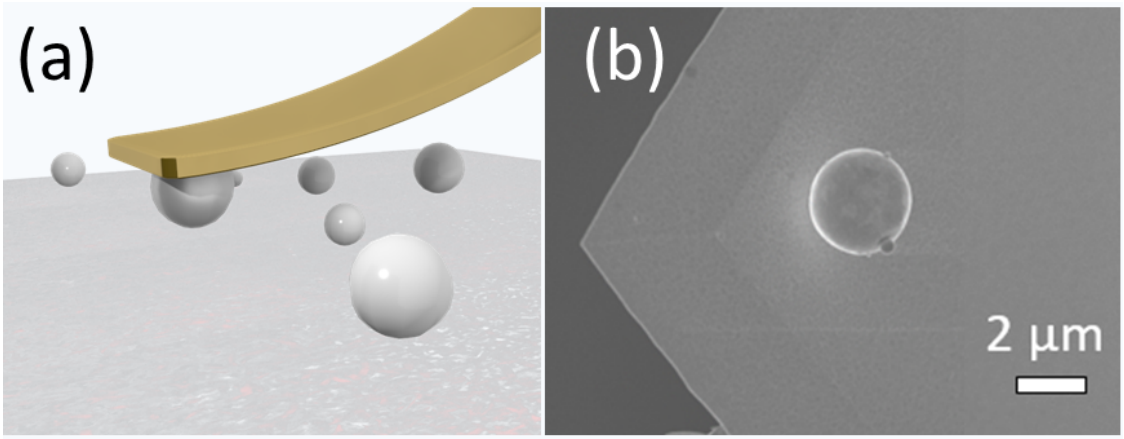


Figure 6.1: (a) Schematic of an AFM cantilever and EGaIn droplets on a SAM substrate illustrating the ability to pick up droplets of various sizes and making molecular junctions in-situ. (b) SEM image of an EGaIn droplet after being picked up by the cantilever.

flow. The high surface energy of the freshly exposed oxide-free EGaIn results in highly spherical shaped microparticles [292]. Once formed, the surface of the droplets are quickly oxidized to form a nanometric oxide layer which prevents further coalescence into larger droplets.

Subsequently, 10 μL of the emulsion is pipetted and drop casted on the alkanethiol SAM substrate to be studied or a polystyrene petri dish. After selecting a suitable microdroplet on the substrate, we approach a selected droplet with a gold-coated tipless cantilever (HQ:NSC36, 0.6 – 5 N/m) with a low force of ∼5 nN. Figure 6.1 illustrates the AFM EGaIn droplet probe system. We found that slight shearing while in contact with the droplet helped to release the droplet from the substrate, hence making it easier to pick up. The choice of substrate also affects the success rate of picking up of EGaIn droplets. Both these substrates chosen are less sticky to the EGaIn microdroplets. In comparison, gold or glass substrates resulted in a much lower success rate of picking up. This is also the reason we use a gold-coated cantilever which is "stickier" to the EGaIn than the substrate. Removing the droplet can be achieved by rastering the cantilever on the surface in contact mode until the droplet is detached.

Other less successful methods to pick up EGaIn droplets are also discussed in Appx. B.

6.4.2 Substrate preparation

Gold bottom electrodes were prepared using reported methods. ∼17.5 nm of gold was thermally evaporated (using a Shen Yang Ke Yi system) onto a silicon wafer (100). Glass substrates were attached onto the gold layer using a Norland UV-activated adhesive, cured in UV light for 1 h. The glass substrate can be lifted off from the silicon wafer using a blade (template stripping); the gold layer is adhered onto it while exposing the surface that was in contact with the silicon surface. This ensures sub-1 nm smoothness. Template-stripped gold is prepared just before immersion into the thiol solutions to prevent exposure of the gold surface to the environment.

6.4.3 Self-assembly

Solutions of the alkanethiols were prepared in ethanol with a concentration of ∼1 mM in a nitrogen atmosphere. Gold substrates were immersed and left overnight (∼15 h) in the solutions, collected the next day, and rinsed with ethanol followed by drying in a stream of nitrogen.

6.5 Characterisation of EGaIn droplet probes

The detailed characterisation and understanding of our EGaIn droplet probe system is crucial for its implementation in various applications. In this section, we look at the surface roughness of the droplet, its contact mechanics and properties of its native oxide layer.

6.5.1 Surface roughness of picked-up EGaIn droplet

We took AFM topographic images of a droplet that we have picked up on a cantilever. We used a much stiffer cantilever (40 vs 0.6 N/m) to image the droplet to prevent resonances with the droplet probe cantilever. The resulting droplet attached to the AFM cantilever is spherical (as shown by the AFM and SEM images in Fig. 6.2(a), (e)) and smooth with a root mean square roughness of 1.1 nm (as shown by the AFM topography images in Figs. 6.2(a – c). Once picked up, the microdroplet is strongly attached to the cantilever with a contact angle $\theta_c = 148°$ (Fig. 6.2(d)),

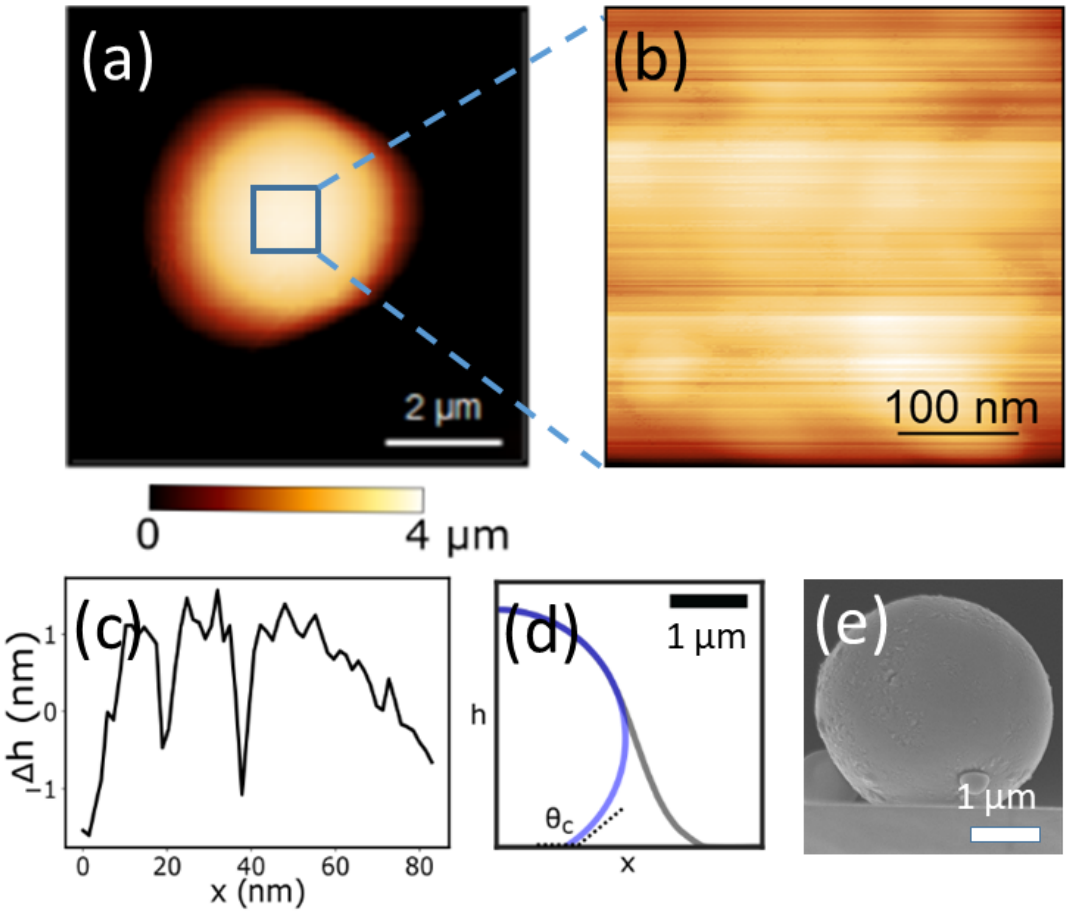


Figure 6.2: (a) AFM topographic image of an EGaIn droplet attached to a cantilever after the picking up process. (b) The corresponding AFM image of a zoomed-in region on the spherical droplet and (c) its corresponding line section. (d) A fitted sphere (blue line) based on a radially averaged line section (gray line) of the topographic image in (a). The contact angle is found to be $\theta_c = 148°$. (e) SEM image of the same EGaIn droplet.

presumably because of strong adhesion between the surface oxide layer of EGaIn and the gold coating of the cantilever. Hence, we can move the droplet to various regions on the substrate to form well-defined contacts repeatably without detaching from the cantilever. At the same time, the oxide layer also prevents direct contact of the liquid metal with gold; in the absence of this oxide layer (for example after exposure to hydrochloric acid vapour), EGaIn will amalgamate with the gold and the droplet will no longer be spherical (see Fig. 6.9).

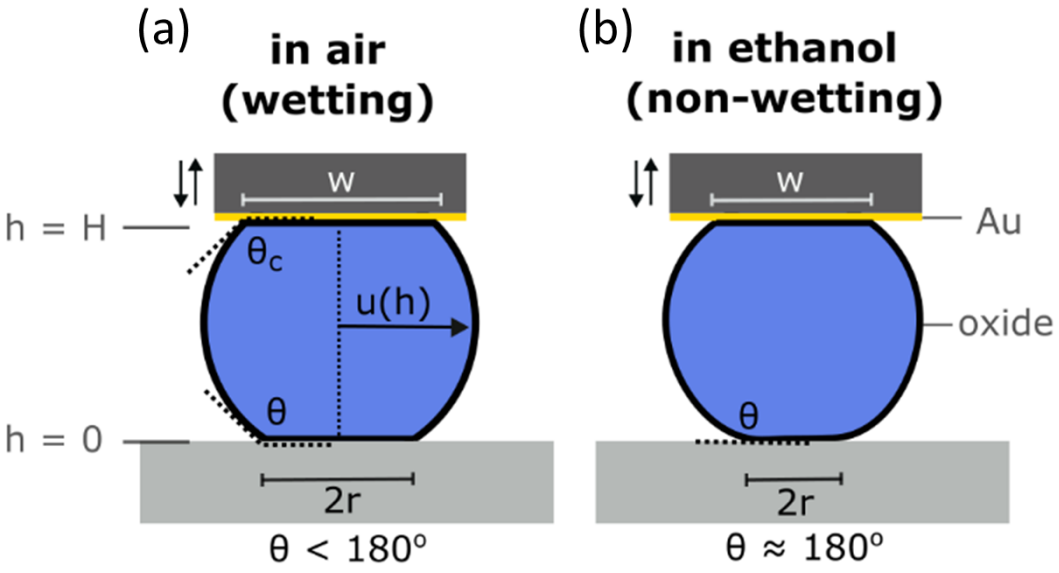


Figure 6.3: Droplet geometries in (a) air (wetting) and (b) in ethanol (non-wetting) during force spectroscopy measurements.

6.5.2 Contact mechanics of EGaIn droplets

We investigated the contact mechanics of EGaIn droplets on template-stripped gold surfaces functionalised with SAMs of different alkanethiols. Alkyl functional groups were chosen because they are widely used to render surfaces hydrophobic and alkanethiol SAMs are known to form stable molecular tunnelling junctions.

The contact mechanics of EGaIn droplets are greatly dependent on their wetting properties. An EGaIn droplet wets the alkanethiol surface with a contact angle $\theta < 180°$ in air, but is non-wetting (or at least nearly non-wetting) with $\theta \approx 180°$ when submerged in ethanol (Fig. 6.3). The different wetting behaviours have important implications on how well we can control the contact diameter $2r$ that EGaIn droplets make on alkanethiol surfaces.

Detailed contact mechanics and differences in wetting behaviours of EGaIn droplets can be investigated by performing force spectroscopy measurements on the alkanethiol surface C4 in air and in ethanol (Fig. 6.4(a), (b)). This is similar to previous work done by Daniel et al. and Escobar et al. [293–296]. After picking up an EGaIn droplet with diameter $2R = 10$ μm using a tipless AFM cantilever

($k = 5$ N/m), we use the piezomotor of the AFM to control the vertical motion of the EGaIn droplet. As the droplet approaches and retracts from the surface at a speed $U = 0.5$ μm/s, the force F experienced by the droplet can be deduced from the cantilever deflection (approach and retract curves are represented by dashed and full lines in Figures 6.4(a), (b), respectively).

In air, the droplet experiences a sudden snap-in force, $F_{\text{snap}} = 1.6$ μN due to capillary forces as it contacts and wets the surface (Fig. 6.4(a)). There is also strong droplet adhesion to the surface due to the wetting behaviour. The adhesion force, F_{adh} is measured to be 2.2 μN. We also observe a large hysteresis between the approach and retract curves.

In contrast, there is no detectable F_{snap} for an EGaIn droplet of similar diameter ($2R = 12$ μm) contacting the same C4 surface in ethanol. Moreover, there is little hysteresis between the approach and retract curves and minimal $F_{\text{adh}} = 1$ nN. This suggests that EGaIn droplets are non-wetting (or at least nearly non-wetting) when submerged in ethanol. Small discrete force jumps of magnitudes $\delta F \sim 1$ nN were observed in the approach and retract curves indicating that the droplets are slightly pinned and θ is only approximately 180°. We note that the droplet is non-wetting in ethanol, because ethanol is chemically similar to alkyl SAMs. The same non-wetting behaviour should be observed for EGaIn droplets submerged in other organic solvents such as hexane.

It is possible to relate the force spectroscopy measurements to the evolution of the microdroplet's contact diameter $2r$ and angle θ with time, since

$$F = -2\pi\gamma r \sin\theta + \pi r^2 \Delta P, \tag{6.1}$$

where $\Delta P \approx 2\gamma/R$ is the Laplace pressure inside the droplet, and $\gamma = 630$ mN/m in air and 400 mN/m in ethanol [264, 297]. Since we are moving the droplet slowly with a typical speed $U = 0.5$ μm/s, the droplet's shape is always in equilibrium (quasi-static approximation) and is therefore given by the axisymmetric Young-Laplace equation

$$\frac{u''}{(1+u'^2)^{3/2}} - \frac{1}{u\sqrt{1+u'^2}} = -\Delta P/\gamma \text{ for } h \in (0, H) \tag{6.2}$$

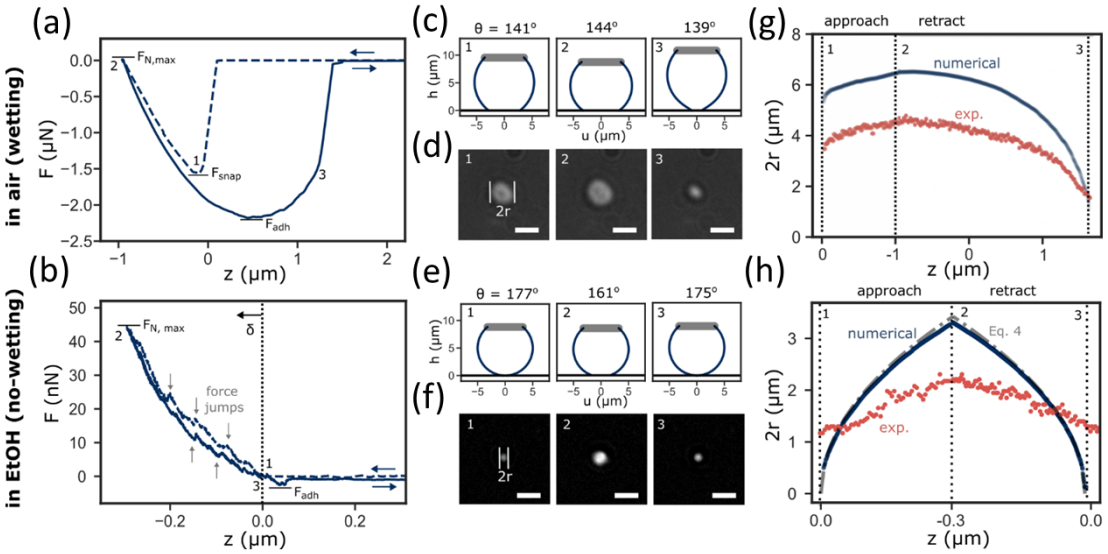


Figure 6.4: (a, b) Force spectroscopy of an EGaIn droplet ($2R = 10$, 12 μm) contacting the C4 surface in air and in ethanol, respectively. z is the droplet position after correcting for cantilever deflection. (c, d) Droplet geometries obtained by solving Young-Laplace equation and micrographs of the droplet's base at locations 1–3 in air. Scale bars are 4 μm. (e, f) The corresponding droplet geometries and micrographs in ethanol. Scale bars are 4 μm. (g, h) Comparison between $2r$ as predicted by Young-Laplace equation (blue lines) and observed experimentally in micrographs (red dots) in air and in ethanol, respectively.

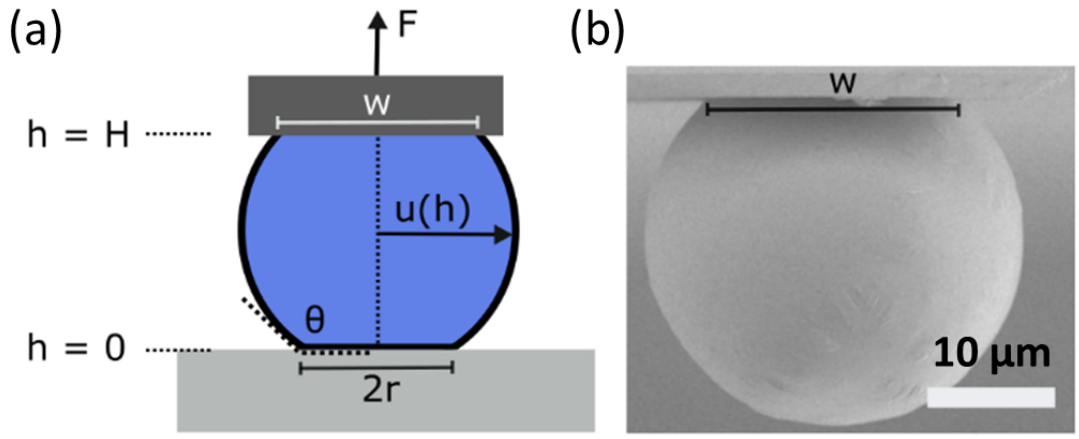


Figure 6.5: (a) Droplet geometry during force spectroscopy. (b) Side view of EGaIn droplet.

subject to the boundary conditions

$$\begin{aligned} u(0) &= r \\ u(H) &= w/2 \\ \int_0^H \pi u^2 dh &= V, \end{aligned} \tag{6.3}$$

where w is the width of the droplet contact on the AFM cantilever and V is the droplet's volume (Fig. 6.5(a)). w can be determined from sideview SEM image of the EGaIn droplet (Fig. 6.5(b)).

There are several ways to solve this boundary value problem numerically. Here, we use the shooting method, implemented in the Python programming language. Instead of solving the boundary value problem directly, we frame it as an initial value problem and numerically integrate Eq. 6.2 with Runge-Kutta method subject to the initial conditions

$$\begin{aligned} u(0) &= r \\ u'(0) &= -\cot\theta \end{aligned} \tag{6.4}$$

and the requirement that

$$\mathbf{m}(r, \Delta P, \theta) = \begin{pmatrix} u(H) - w/2 \\ \int_0^H \pi u^2 dh - V \\ F + 2\pi\gamma r \sin\theta - \pi r^2 \Delta p \end{pmatrix} = 0. \tag{6.5}$$

This converts the boundary value problem into a root-finding problem $\mathbf{m} = 0$, with r, θ, and ΔP as fitting parameters. An example code can be found in the github repository [298].

Therefore, by solving Eqns. 6.1 and 6.2 numerically, we can deduce the droplet's geometry both in air and in ethanol (Fig. 6.4(c), (e)), from the point of contact (position 1), to the maximal loading force (position 2) and just before detaching from the surface (position 3). The numerical results, in particular the base radius r, can then be compared to experimental r values measured under reflected light microscopy (Fig. 6.4(d), (f)).

For an EGaIn droplet in air, Eq. 6.1 simplifies to $\pi r^2(2\gamma/R) \approx 2\pi\gamma r \sin\theta$ and hence,

$$r = R\sin\theta \tag{6.6}$$

Table 6.1: Contact size of EGaIn droplets on different alkanethiol SAMs in air

2R (μm)	Surface	F_{N} (nN)	2r (μm)	r/R	θ
4.6	C4	10	2.8	0.61	143°
4.6	C4	10	1.8	0.40	158°
5.7	C4	10	2.7	0.47	152°
6.1	C4	10	2.0	0.32	161°
6.5	C4	10	2.0	0.31	162°
7.1	C4	50	3.6	0.50	150°
7.1	C6	10	2.7	0.38	158°
10.0	C4	10	5.6	0.56	146°
10.0	C6	20	4.8	0.48	151°
10.0	C8	10	5.3	0.53	148°
10.0	C10	10	4.6	0.46	153°
11.0	C4	10	4.6	0.42	155°
28.0	C4	5	14.0	0.50	150°
28.0	C4	20	14.5	0.52	149°
28.0	C6	10	13.3	0.48	152°
28.0	C8	10	14.0	0.50	150°
28.0	C10	10	13.6	0.49	151°
28.0	C10	20	14.0	0.50	150°

in the limit of small loading force F_{N}; r is relatively insensitive to the applied F_N and only depends on the droplet radius R and the contact angle θ. This is reflected in the numerical and experimental r values in Fig. 6.4(g), where r remains relatively constant when increasing F_{N} from -1500 nN to a maximum of 10 nN (position 1 to 2), with $2\,r_{\mathrm{numerical}}$ increasing from 5.6 to 6.4 μm and $2\,r_{\mathrm{exp}}$ increasing from 3.4 to 4.5 μm (an increase of between 15 and 30%). The contact angle θ is a material property given by the Young's relation $\cos\theta = (\gamma_{\mathrm{ls}} - \gamma_{\mathrm{s}})/\gamma$, where γ is the droplet's surface tension, γ_{s} is solid surface energy and γ_{ls} is the liquid-solid interfacial energy. We repeated the force spectroscopy measurements 18 times for droplets of different diameters (i.e. 5 – 30 μm) and found that $r/R = 0.46 \pm 0.09$ or equivalently $\theta = 152° \pm 6°$ (Eq. 6.6) for different alkanethiol surfaces with the applied force, F_N, ranging from 5 to 50 nN (See Table 6.1).

In contrast, for a (nearly) non-wetting EGaIn droplet in ethanol, we expect

$$r = \sqrt{2R\delta} \tag{6.7}$$

in the limit of small F_N and indentation depth $\delta = |z|$ (gray dashed-dot line in Fig. 6.4(h)). This is in good agreement with the simulation results (blue full line in Figure 6.4(h)). In ethanol, $2r$ increases more rapidly (in terms of percentage increase when compared to the same droplet in air) when increasing F_N from 0 to 45 nN, with $2\,r_{\text{numerical}}$ increasing from 0.5 to 3.3 μm and $2\,r_{\text{exp}}$ increasing from 1.1 to 2.3 μm (an increase of between 2 and 7 times). Because of the diffraction limit of the microscope, we cannot resolve $2\,r_{\text{exp}} < 1$ μm and therefore are likely to overestimate r_{exp} values near the point of contact $z = 0$, which partly explains the discrepancy between r_{exp} and Eq. 6.7.

This simplified analysis ignores the mechanical properties of the solid oxide layer (Young's modulus $E \sim 1$ GPa [299]) which exert an additional repulsive force during the indentation process. This explains why $r_{\text{numerical}}$ is systematically higher than r_{exp} in Figs. 6.4(g), (h). However, we are able to capture the main physics behind the contact mechanics of EGaIn droplets with important implications on how well we can control the contact diameter $2r$. As expected, the contact diameter is smaller for non-wetting droplets than for wetting droplets for the same applied force. The contact diameter also increases more quickly with increasing applied force for non-wetting droplets. More importantly, a hysteresis-free force curve in non-wetting droplets means more reproducible control of the contact diameter, which only depends on the amount of force applied, F_N and independent on how it is applied, i.e. path and rate independent. In contrast, the contact diameter for wetting droplets depends not only on the magnitude of the applied force, but also on whether it is on the approach or retract curves.

6.5.3 Crack formation in millimetric-sized droplet

As discussed, the oxide layer remains intact during force spectroscopy of micrometric sized droplets because of the small loading force applied $F_N = 10$ nN. This is reflected in the force spectroscopy curves which are smooth (Fig. 6.6(a)) and in the SEM image of the droplet showing a crack-free oxide layer after indentation (Fig. 6.6(b)).

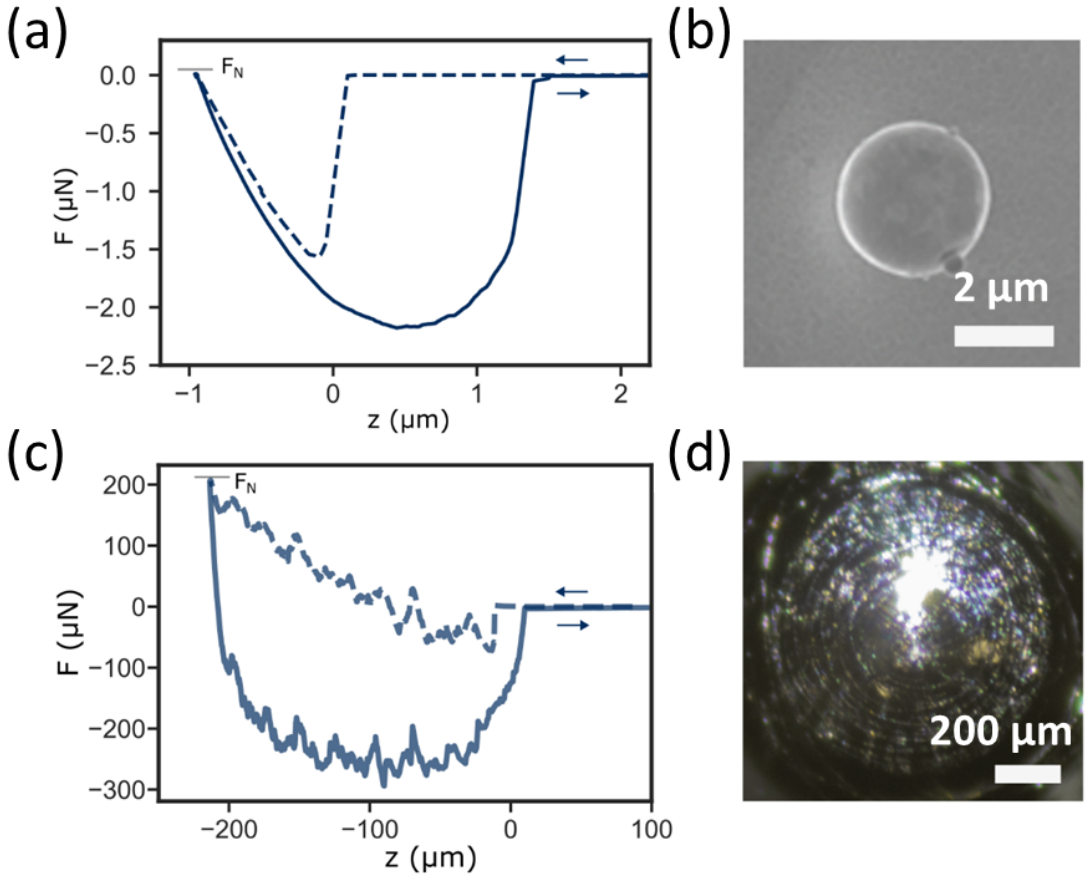


Figure 6.6: (a) Force spectroscopy for micrometer-sized EGaIn droplet. (b) SEM image of the micrometric droplet which remains smooth after force spectroscopy. (c) Force spectroscopy for millimetre-sized EGaIn droplet. (d) Optical micrograph showing concentric cracks on the base of millimetre-sized droplet after force spectroscopy.

In contrast, indenting a millimetric-sized EGaIn droplet ($2R \approx 4$ mm) with a maximum force $F_N = 200$ μN, ruptures the oxide layer. This is evident in the periodic and discrete jumps in the force curves (Fig. 6.6(c)) [300]. We similarly observed periodic, concentric rings at the bottom of the EGaIn droplet where the skin layer was ruptured (Fig. 6.6(d)) . Similar cracks were previously observed by other groups when indenting millimetric-sized droplets [300].

6.5.4 The effect of oxide for electrical measurements

We hypothesize that there are two layers of oxide in our EGaIn droplet probe system. One oxide layer between the cantilever and the droplet, and the other oxide layer between the droplet and the SAM. We believe that the oxide layer is intact

between the droplet and the cantilever as we do not observe any amalgamation of the EGaIn with the gold coated cantilever over time. This is in comparison to the traditional EGaIn syringe technique which only has one oxide layer between the EGaIn and substrate [286]. Here, we investigate whether having two oxide layers in the structures will affect electrical measurements.

Figure 6.7(a – c) illustrates the 3 three different experimental conditions in which we took IV sweeps on C4 SAM. We first used a sharp conductive tip to contact an EGaIn droplet sitting on C4 SAM surface while applying a small voltage of 1.5 V. At a small loading force $F_N = 10$ nN, the sharp tip sat on top of the droplet without puncturing the oxide layer (Fig. 6.7(a)), whereas at a loading force $F_N >$ 200 nN, the oxide layer was punctured (Fig. 6.7(b)). This is indicated by the "jumps" observed in the extend curve as well as the sharp increase in current (Fig. 6.7(d)). In our experiments with tipless cantilevers (Fig. 6.7(c)), we usually contact the droplet at a small $F_N = 5 – 10$ nN insufficient to puncture the oxide layer.

To confirm that the electrical properties are dominated by the SAM layer and not affected by the top oxide layer, we performed a voltage sweeps between -4 and 4 V and measured IV for the three configurations: on EGaIn, inside EGaIn and droplet probe (Fig. 6.7(a), (b) and (c), respectively). Figure 6.7(e) summarises the IV results. Each curve is an average of at least 40 separate IV curves. As expected, the case for two oxides is more resistive than the case for one oxide layer. This is because the conductive tip is only contacting a small area on the top of the droplet. After puncturing the EGaIn droplet, we observe higher conductivity. The IV of the droplet probe more closely resembles the one oxide case. Moreover, it appears to be more conductive. This is likely due to the larger contact surface area between the cantilever and the EGaIn droplet (Fig. 6.2(e)). This suggests that the SAM and not the oxide layers dominate the resistance.

6.6 Benchmarking on alkanethiol SAMs

In order to demonstrate the approach as a viable method, we measure current through SAMs of alkanethiols of various lengths, C4, C6, C8, C10, and extract the

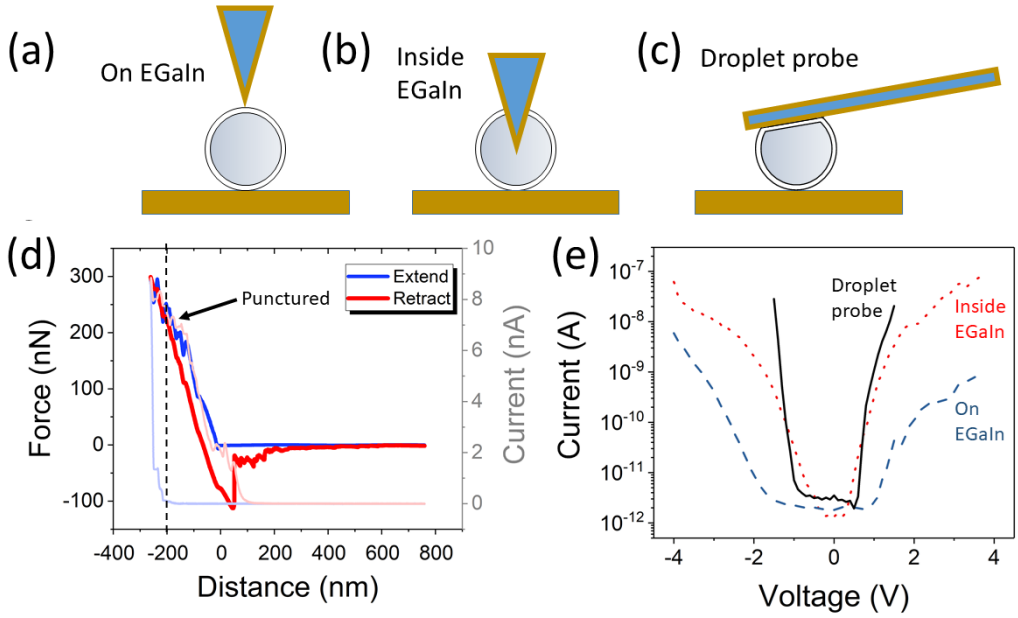


Figure 6.7: Conductive tip (a) sitting on, (b) piercing an EGaIn droplet and (c) the droplet probe AFM method. (d) Simultaneous force spectroscopy and current measurements for a conductive tip contacting the EGaIn droplet. (e) IV sweeps on C4 SAM for the three configurations in (a), (b) and (c). Each curve is an average of at least 40 separate curves.

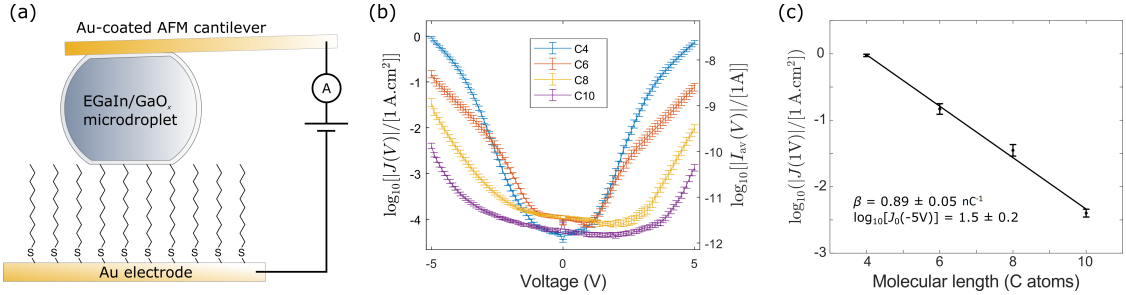


Figure 6.8: (a) Schematic of the electrical set-up. The EGaIn droplet probe contacts a molecular SAM adsorbed on a template-stripped gold substrate that is grounded. The structure is connected to a source-measure unit that sources a voltage and measures the current. (b) J(V) traces of junctions of different alkanethiol lengths. The right y-axis represents the corresponding current magnitude for an average-sized junction (with microdroplet diameter of 4.76 μm). (b) Extraction of the exponential decay parameter, β from current density values taken at -5 V. The error bars represent the 95% confidence interval.

exponential decay coefficient, β of the current density as a function of molecular length. This is a standard way to benchmark methods for contacting molecular SAMs as the value of the decay coefficient is a signature of molecular transport [301–303].

Samples were prepared for each of the four molecular lengths, and about 15 junctions were measured for each. The current was recorded as the voltage was scanned in the range -5 to +5 V. The diameter of the droplets used for the measurements is measured from the integrated microscope of the set-up. We use the droplet diameter to infer the geometric contact area, as explained in Sec. 6.5.2, to normalise the current and obtain the current density. The logarithm average of these measurements is shown for each length in Fig. 6.8(b), where the exponential decay of current density with molecular length can be clearly seen. A fit of this decay at -5V is shown in Fig. 6.8(c). It yields a decay parameter $\beta = 0.89 \pm 0.05$ nC^{-1}, close to the typical literature value of 1.0 $\pm$ 0.1 nC^{-1} from established methods. However, the value of J_0, i.e. the projection of current density for a zero carbon length, is low compared to most reported methods. For example, most micropore devices have a $\log_{10} J_0$ in the range of 5 – 9 (for J_0 in A/cm^2 and at 0.5V), while EGaIn-based junctions typically yield 2.0 – 4.2 in similar conditions [301]. Here, for a higher voltage magnitude, at -5V, $\log_{10} J_0 = 1.5 \pm 0.2$. This points to a lower contact efficiency, allowing us to contact a lower number of molecules. The flat regions observed at low voltages is due to sub-pA current being measured which is at the limit of our instrument. Low current is measured due to a very small contact area as discussed above.

Interestingly, the junctions show extreme robustness, and can be subjected to voltages in a range of -5 to 5 V without noticeable damage, compared to a usual safe range of -1.5 to 1.5 V for the EGaIn cone-shaped-tip technique. The indentation measurement, as described in Sec. 6.5.4, shows that the voltage drop across other parts of the structure is negligible in comparison to that across the molecular SAM. Hence, the junctions are indeed stable in this voltage range. The much smaller contact area means that a breakdown of the junctions are less likely to occur [304]. In the percolation model of thin film breakdown, the time to breakdown for any

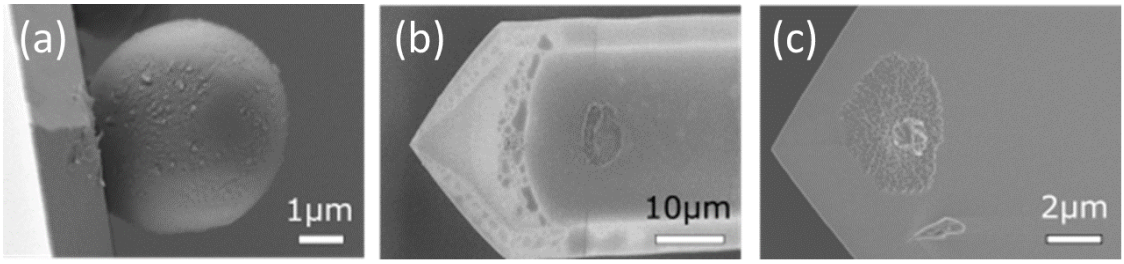


Figure 6.9: SEM image of (a) an EGaIn droplet probe 1 week after electrical measurements on SAM. The droplet probe remains conductive and maintains its spherical shape. (b) An EGaIn probe exposed to Hydrochloric acid vapour to remove the oxide. This results in the EGaIn losing its spherical shape as it wets and coats the cantilever. (c) Another example of an EGaIn droplet that has burst and amalgamated with gold coated cantilever. Cantilevers such as (b) and (c) will result in junctions that short-circuit and is not suitable for making reliable molecular junctions.

given value of voltage scales with A^{-1/β_W} where A is junction area, and β_W the Weibull slope. β_W is a positive value and a measure of the variation in the time to breakdown (i.e. Given the same conditions, a smaller junction will be stable for longer than a larger one.) [305]. This means that our method can produce junctions of exceptional stability, and address molecules over a larger voltage range which was previously inaccessible with other methods.

6.6.1 Stability of droplet probe

The EGaIn droplets are typically stable for at least a hundred voltage sweeps. Figure 6.9(a) shows a used tip after at least taking a hundred current measurements. There is no sign of deformation or amalgamation with the cantilever. In contrast, Fig. 6.9(b) and (c) represents situations where the oxide layer of the EGaIn droplet is removed with hydrochloric acid or damaged. This causes the liquid EGaIn inside to spill out, wet and amalgamate with the gold-coated cantilever.

6.7 Chapter Summary

We fabricated smooth microspheres (1 – 10 μm) via ultrasonication. Subsequently, these EGaIn particles can be manipulated in an AFM system hence conferring nanoscale precision. Since the EGaIn droplet is a fluid held together by an oxide skin, the contact area between the droplet and a surface can be reliably controlled

by tuning its wetting properties and applied force. This in combination with precise force control, we demonstrate an application of our probes by making small and well-defined molecular junctions. We verify this by extracting the decay coefficient, $\beta = 0.89 \pm 0.05$ nC^{-1}, from measurements of four alkanethiols with different carbon chain lengths. This value is comparable to the literature and is indicative of molecular behaviour. The ability to manipulate EGaIn microspheres in an AFM is not limited to applications in molecular electronics. It opens up the possibilities for exploring mesoscale physics and scaling down the many applications of liquid metals to the nanoscale.

Author Contributions

The SAM samples were prepared by Hippolyte Astier (Department of Chemistry, National University of Singapore). Analysis of contact mechanics was done together with the help of Dan Daniel (Institute of Materials Research and Engineering, A*STAR). The electrical set-up, measurements and analysis were done together with Hippolyte Astier. I conceived the method of fabricating EGaIn tips as well as fabricated them.

Curiouser and curiouser!

— Lewis Carroll, Alice's Adventures in Wonderland / Through the Looking-Glass

7 Conclusions

This work is mainly driven by the need to invent new ways to manipulate single micro and nanoparticles in a pick-and-place fashion. We have considered state-of-the-art methods available to manipulate particles and discussed the general considerations and challenges towards developing new particle manipulation methods. Inspired by the lack of manipulation techniques available for single particle manipulation in three-dimensions, we aim to develop techniques to achieve this using the AFM as a manipulation tool.

In Chapter 3 and 4, we show that nanoparticles can be picked up using an AFM tip by coating the tip with various functional coatings. Chemical functionalisation is able to attach multiple nanoparticles onto the tip fairly uniformly. However, picking up a single nanoparticle proved challenging with chemical methods. We showed that this is due to the passivating and active chemicals diffusing through each other. In contrast, the coating of materials capable of forming nanoscale conductive filaments are able to confine the electric field to a nanoscale region on the tip apex. We make use of this feature to pick up single 20 nm gold particles via dielectrophoresis. This facile fabrication of a single nanoparticle probe could lead to new applications in tip-enhanced Raman specroscopy as well as other plasmonic applications. Furthermore, we demonstrate an enhanced electrical resolution achieved in Kelvin probe force

microscopy due to the electric field confinement. The applications can also be applied to all other conductive AFM techniques.

Although picking up of nanometer scale particles has been achieved in Chapter 4, placing a single nanoparticle after picking it up has been extremely challenging due to strong adhesion to the manipulator. This is also known as the "sticky hands" problem mentioned in Chapter 1. Therefore, we explored the use of hollow cantilevers (also known as FluidFM technology) where an undepressure and overpressure can be used to aspirate and dispense particles which are larger than the aperture, similar to how a drinking straw works. We showed that 1 μm particles can be directly picked up and placed at any desired location in a liquid medium. However, the particles tend to move from its position when the liquid is dried. This would be a problem for applications in air. Therefore, we investigated whether we can directly deposit small nanoparticles through the aperture, similar to printing. Few to single nanoparticles can be deposited by using a dilute nanoparticle solution. Since the hollow cantilever is integrated with an AFM, we can develop ways to monitor the deposition in-situ by looking at the deflection signal of the cantilever. Furthermore, we have the ability to image a surface before and even during deposition which allows us to align our nanoparticle deposition to within <500 nm. This will have direct applications to fabricating microLED structures where precise positioning of quantum dots into nanostructures is required.

Manipulating larger micrometer sized particles gives us the flexibility to align and monitor the process optically. In Chapter 6, we show that a liquid metal (i.e. EGaIn) can be shaped into spherical microparticles. Single spheres can be picked up by an AFM cantilever forming a unique liquid metal probe. Taking advantage of the force feedback mechanism of the AFM, we are able to controllably adjust the contact area between the compliant liquid metal sphere and substrate. We demonstrate an application in molecular electronics by forming molecular junctions in the weak coupling regime, which would be difficult to achieve with metallic electrodes. This is the first work implementing the liquid metal electrode system together with an AFM. This opens the possibilities of studying electrical properties

of mixed molecule monolayers by taking electrical measurements while mapping the surface with nanometer scale precision. Furthermore, nanowelding applications using liquid metal can now be explored with nanometer scale precision provided by the AFM. Other liquid metals can also be explored. For example, we can control the phase (solid vs. liquid) of Gallium easily due to its low melting point of 30°C. This offers a way to tune its applications based on environmental temperature.

A variety of techniques have been developed to manipulate various types of micro and nanoparticles. The desired application often sets the requirements and parameters for manipulation (e.g. material, size and shape of particle, material and geometry of the substrate, environment, etc.). The techniques presented here are general and can serve as a guide which can be modified accordingly to suit the desired applications.

Throughout this thesis, I have presented multiple ways micro and nanoparticles can be manipulated by suitably functionalising an AFM tip. Along the way, I have demonstrated novel applications with these modified tips that would have been very difficult to achieve with conventional nanomanufacturing techniques. The general technique of manipulating different types and sizes of particles is not limited to the applications discussed in this thesis. Any experiment that aims to study the interaction between a single or few particle and a nanostructure would require precise alignment of the particle to the nanostructure. Hence, I believe that AFM manipulation technologies will find many uses in a wide variety of fields from electronics, photonics and biology.

Finally, I summarise my original key contributions as follows:

1. The invention of a novel and elegant method to fabricate electrically high-resolution AFM tips by coating with a suitable material (i.e. SAMs, carbon, GST). We demonstrate its high resolution by picking up a single 20 nm particle can be picked up at the tip apex. Moreover, these tips have direct applications to enhancing the electrical resolution of all conductive AFM techniques.

2. The demonstration of direct pick and place of 1 μm particles using a hollow cantilever with pressure control in a liquid medium. Moreover, nanoparticles can also be printed directly from the microchannel. Methods have been developed to monitor the printing process in-situ as well as to image the substrate during deposition to ensure good alignment, within 500 nm.

3. The demonstration of direct and precise manipulation of EGaIn microdroplets using an AFM, enabling us to control the contact area with a substrate on the micrometer scale. This allows us to form molecular junctions of exceptional stability and to address molecules over a larger voltage range previously inaccessible with other methods.

Publications and conferences

List of publications

Work presented in this thesis

1. Soh, E. J. et al. Filamentary High-Resolution Electrical Probes for Nanoengineering. Nano Letters 20, 1067–1073 (2020).

2. Soh, E. J. et al. Liquid metal droplet Atomic Force Microscopy for controlled-area molecular tunneling junctions (in preparation).

Contributions outside this thesis

1. Shu, Yu et al. Nanoscale Bilayer Mechanical Lithography Using Water as Developer. Nano Letters 21, 3827-3834 (2021).

Conferences attended

1. Soh, E. J. et al. High resolution electrical probes with single nanoparticle pick-up resolution, Materials Research Society Fall, 1–6 December, 2019, Boston, Massachusetts.

2. Soh, E. J. et al. Filamentary High-Resolution Electrical Probes. 30th Micromechanics and Microsystems Europe workshop, 18–20 August, 2019, Oxford, United Kingdom.

3. Soh, E. J. et al. Reconfigured Filamentary High Resolution Electrical Probes, Microscience Microscopy Congress, 1–4 July, 2019, Manchester, United Kingdom.

Appendices

A thinker sees his own actions as experiments and questions—as attempts to find out something. Success and failure are for him answers above all.

—Friedrich Nietzsche

A

Attempts at placing single particle

Contents

A.1 Placing on APTES coated substrate 127
A.2 Placing on photoresist substrates 128

In this chapter, we briefly look at the methods attempted to place single particles picked up with our filamentary high resolution probes. Although the methods discussed in this chapter did not work to place the particles, lessons can be learned and new methods conceived.

A.1 Placing on APTES coated substrate

We attempted the use of both negative DEP to repel particles from the AFM tip and the chemical affinity of gold nanoparticles to APTES monolayer to adhere the particle to the surface.

We first pattern markers and subsequently opening a window in between these markers on ITO substrates via e-beam lithography. ITO substrates were used as they are conductive, which allows KPFM characterisation as well as DEP to be carried out. APTES is assembled into these patterned windows similar to the process in Sec. 3.3.1. However, ethanol is used instead of toluene to prevent the

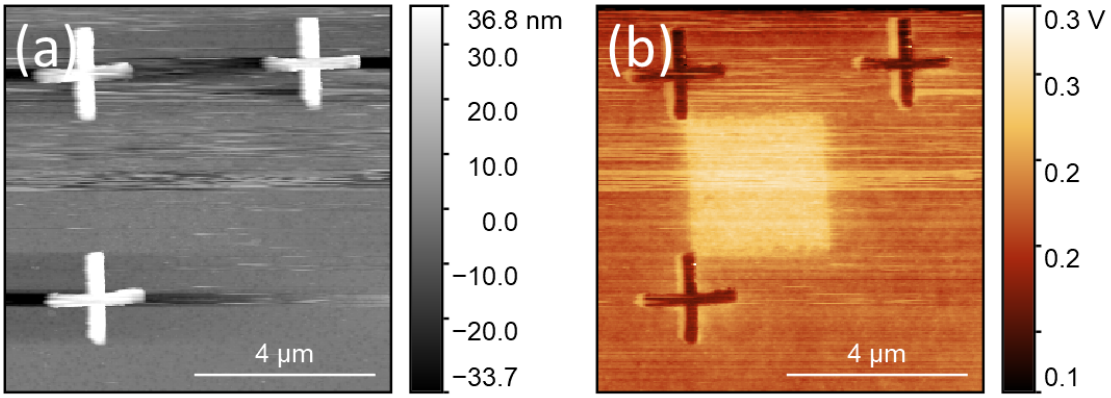


Figure A.1: (a) AFM image and (b) CPD image taken from KPFM. The APTES monolayer is very thin, hence not obvious in the height image. However, it is clearly seen in the CPD image.

photoresist from dissolving while APTES assembles. The presence of monolayer is checked in AFM and KPFM (Fig. A.1). Although there is little contrast in the height image due to the thinness of the monolayer, the CPD image from KPFM clearly shows the position of the APTES assembled.

We perform the experiments in both DI water and citrate buffer medium. A voltage of 10 V peak-to-peak at 10 MHz was applied for at least 60 s. 10 MHz ensures that we are in the negative DEP regime. Hence, the particle is expected to be repelled from the sharp tip and move towards the planar substrate. The distance between the tip and substrate was set to 20 nm.

Despite this process, no nanoparticles were observed to be deposited in AFM and SEM images taken subsequently. We hypothesise that the nanoparticles is strongly adhered to the tip after the picking up procedure. Moreover, the magnitude of negative DEP is half that of positive DEP. Although we have reached the maximum voltage output at 10 MHz for our equipment, it would be worthwhile to try apply a much larger voltage to produce a larger DEP force.

A.2 Placing on photoresist substrates

Since both negative DEP force and chemical affinity were insufficient to dislodge the particle from the tip onto a substrate, we tried to use a mechanical force to remove the particle. This is done by using a "sticky" substrate. In this case, the nanoparticle

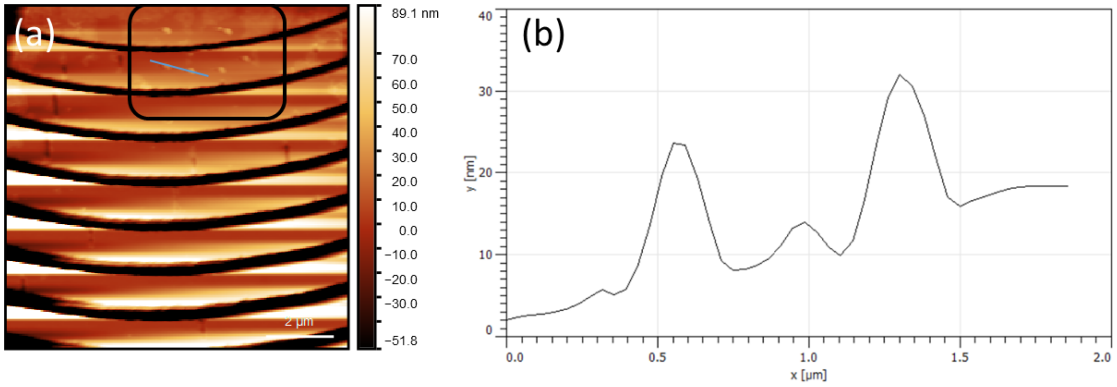


Figure A.2: (a) AFM image of the PMMA substrate after attempted deposition. The curved lines are simply patterns that act as a location marker. (b) Line cross section showing the bumps created.

tip is approached onto a polymethyl methacrylate (PMMA) substrate that is heated to its glass transition temperature. After at least 5 s in contact with the substrate the tip is lifted off and the substrate is cooled to below its glass transition temperature. An AFM image is subsequently taken to check if any particle has been deposited.

Figure A.2 shows the AFM image and the line section over the raised bumps area. Instead of depositing the nanoparticles, 'bumps' in the substrate were created as the tip indents upon approach and pulls on the glassy photoresist upon retracting the tip. This mechanism is similar to previous work on using AFM to indent polymer substrates for memory storage purposes [171].

Subsequent SEM images taken shows that the nanoparticle still remain attached to the tip. This is even after using the nanoparticle tip to image the polymer substrate.

B

Attempts at picking up single liquid metal microspheres

Contents

B.1 Picking up EGaIn microspheres at the liquid-air interface 131

In this chapter, we briefly looked at the methods attempted to pick up single EGaIn microspheres that did not work too well as mulitple particles are picked up. Ideally, we want a single particle to be picked up to avoid ambiguity in any subsequent AFM experiments. Eventually, a simple yet effective method was discovered as you would have seen in Chapter 6.

B.1 Picking up EGaIn microspheres at the liquid-air interface

Initial experiments to pick up EGaIn microspheres in air on a glass substrate had a very low success rate. Hence, to reduce the strong adhesive and capilliary forces present in air, we tried to pick up the EGaIn microparticles at a water-air interface. The EGaIn microparticles are diluted and suspended in water and a tipless cantilever is approached to attempt the picking up of EGaIn particles.

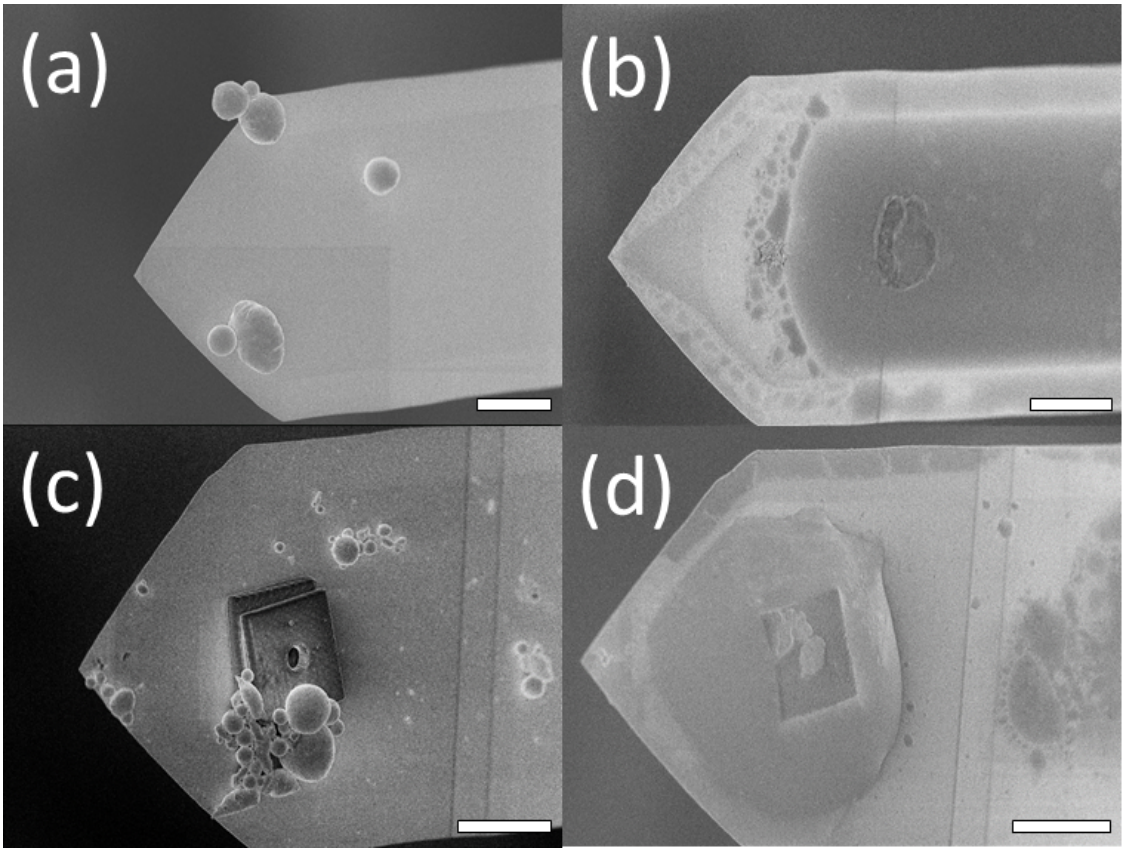


Figure B.1: SEM images of (a) a cantilever after picking up microparticles at the water-air interface. Multiple particles are picked up. (b) the cantilever after acid treatment. (c) the same process with a patterned structure on the cantilever to localise the picking up of particles and (d) the cantilever after acid treatment.

Figure B.1(a) shows the cantilever after picking up particles at the water-air interface. Multiple particles are picked up. For most AFM purposes, this will not be an issue as the contact point will only be determined by the largest particle. However, if the particles are of very similar sizes like the one pictured, it is ambiguous as to which particle makes contact. Moreover, there is a possibility of multiple particles touching the surface. We initially thought that exposing the particles to an acid vapour (i.e. 1M HCl) would remove the oxide layer and cause the multiple droplets to coalesce into a larger spherical droplet [265]. However, since the cantilever is coated in gold and EGaIn wets gold, we ended up spreading the EGaIn into a thin film coating over the cantilever (Fig. B.1(b)).

In order to prevent the spreading of the EGaIn over the entire cantilever, we patterned a polymer (i.e. PMMA) structure on the cantilever using a nanoscribe,

followed by the same picking up procedure at the water-air interface. We picked up multiple particles as well (Fig. B.1(c)). After the acid treatment, the EGaIn was not confined to the well structure that we patterned. It still spread over the structure and cantilever (Fig. B.1(d)).

Hence, we had to look for another approach to directly pick up single EGaIn particles and avoid the need for any acid post-treatment.

There are three stages of scientific discovery: first people deny it is true; then they deny it is important; finally they credit the wrong person.

— Alexander von Humboldt

References

1. Drexler, K. E. *Radical abundance: How a revolution in nanotechnology will change civilization* (Public Affairs, 2013).
2. Arole, V. M. & Munde, S. V. Fabrication of Nanomaterials By Top-Down and Bottom-Up Approaches-an Overview. *JAAST:Material Science (Special Issue* **1,** 2–89 (2014).
3. Mendes, P. M. *et al.* Gold nanoparticle patterning of silicon wafers using chemical e-beam lithography. *Langmuir* **20,** 3766–3768 (2004).
4. Drexler, K. E. *Engines of creation* (Anchor books, 1986).
5. Schweizer, D. K. & Eigler, E. K. *Positioning single atoms with a scanning tunneling microscope* 1990.
6. Sugimoto, Y. *et al.* Atom inlays performed at room temperature using atomic force microscopy. *Nature Materials* **4,** 156–159 (2005).
7. Heucke, S. F. *et al.* Placing individual molecules in the center of nanoapertures. *Nano Letters* **14,** 391–395 (2014).
8. Kim, S., Shafiei, F., Ratchford, D. & Li, X. Controlled AFM manipulation of small nanoparticles and assembly of hybrid nanostructures. *Nanotechnology* **22,** 115301. http://stacks.iop.org/0957-4484/22/i=11/a=115301?key=crossref.e6867109efe40b626ddf9d98c34128c3 (2011).
9. Fuechsle, M. *et al.* A single-atom transistor. *Nature Nanotechnology* **7,** 242–246 (2012).
10. Yin, C. *et al.* Untethered microgripper-the dexterous hand at microscale. *Biomedical Microdevices* **21** (2019).
11. Grigoriev, V., Bonod, N., Wenger, J. & Stout, B. Optimizing nanoparticle designs for ideal absorption of light. *ACS Photonics* **2,** 263–270 (2015).
12. Nishiguchi, K. & Oda, S. Electron transport in a single silicon quantum dot structure using a vertical silicon probe. *Annual Device Research Conference Digest* **4186,** 79–80 (2000).
13. Ding, Y. *et al.* Single nanoparticle semiconductor devices. *IEEE Transactions on Electron Devices* **53,** 2525–2531 (2006).
14. Barth, M. *et al.* Nanoassembled plasmonic-photonic hybrid cavity for tailored light-matter coupling. *Nano Letters* **10,** 891–895 (2010).
15. Xiao, Y.-F. *et al.* Strongly enhanced light-matter interaction in a hybrid photonic-plasmonic resonator. *Physical Review A* **85,** 31805 (2012).

16. Ashkin, A. Forces of a single-beam gradient laser trap on a dielectric sphere in the ray optics regime. *Biophysical Journal* **61,** 569–582. http://dx.doi.org/10.1016/S0006-3495(92)81860-X (1992).

17. Roosen, G. & Imbert, C. Optical levitation by means of two horizontal laser beams: A theoretical and experimental study. *Physics Letters A* **59,** 6–8 (1976).

18. Ashkin, A., Dziedzic, J. M., Bjorkholm, J. E. & Chu, S. Observation of a single-beam gradient force optical trap for dielectric particles. *Optics Letters* **11,** 288. arXiv: 1411.1912. https://www.osapublishing.org/abstract.cfm?URI=ol-11-5-288 (1986).

19. Ashkin, A., Dziedzic, J. M. & Yamane, T. Optical trapping and manipulation of single cells using. *Nature* **330,** 769–711 (1987).

20. Dholakia, K., Reece, P. & Gu, M. Optical micromanipulation. *Chemical Society Reviews* **37,** 42–55 (2008).

21. Devaney, A. J. & Wolf, E. Multipole expansions and plane wave representations of the electromagnetic field. *Journal of Mathematical Physics* **15,** 234–244 (1973).

22. Dorizzi, R. R. & Ulanowski, Z. Theoretical determination of the radiation force for a spherical particle illuminated by a focused laser beam. *Journal of Quantitative Spectroscopy and Radiative Transfer* **110,** 1483–1489 (2009).

23. Lin, S. & Hu, J. Optical trapping of nanoparticles. *Integrated Nanophotonic Resonators: Fundamentals, Devices, and Applications* **24,** 225–255 (2015).

24. Zhang, J., Kim, H. I., Oh, C. H., Sun, X. & Lee, H. Multidimensional manipulation of carbon nanotube bundles with optical tweezers. *Applied Physics Letters* **88,** 1–3 (2006).

25. Plewa, J., Tanner, E., Mueth, D. M. & Grier, D. G. Processing carbon nanotubes with holographic optical tweezers. *Optics Express* **12,** 1978 (2004).

26. Ashkin, A. Applications of laser radiation pressure. *Science* **210,** 1081–1088 (1980).

27. Hansen, P. M., Bhatia, V. K., Harrit, N. & Oddershede, L. Expanding the optical trapping range of gold nanoparticles. *Nano Letters* **5,** 1937–1942 (2005).

28. Bosanac, L., Aabo, T., Bendix, P. M. & Oddershede, L. B. Efficient optical trapping and visualization of silver nanoparticles. *Nano Letters* **8,** 1486–1491 (2008).

29. Svoboda, K & Block, S. M. Optical trapping of metallic Rayleigh particles. *Optics letters* **19,** 930–932 (1994).

30. Hester, B., Helmerson, K., Levin, C. & Halas, N. J. Optical trapping near resonance. *Optics InfoBase Conference Papers* (2008).

31. Arias-Gonzalez, J. R. and Nieto-Vesperinas, M. Optical forces on small particles : attractive and. *Journal of Optical Society of America A* **20,** 1201–1209 (2003).

32. Pelton, M. *et al.* Optical trapping and alignment of single gold nanorods using plasmon resonances. *Plasmonics: Metallic Nanostructures and their Optical Properties IV* **6323,** 63230E (2006).

33. Kawata, S., Inouye, Y. & Sugiura, T. Near-field scanning optical microscope with a laser trapped probe. *Japanese Journal of Applied Physics* **33,** L1725–L1727s (1994).

34. Prikulis, J. *et al.* Optical Spectroscopy of Single Trapped Metal Nanoparticles in Solution. *Nano Letters* **4,** 115–118 (2004).

35. Seol, Y., Carpenter, A. E. & Perkins, T. T. Gold nanoparticles: enhanced optical trapping and sensitivity coupled with significant heating. *Optics Letters* **31,** 2429–2431 (2006).

36. Dienerowitz, M., Mazilu, M., Reece, P. J., Krauss, T. F. & Dholakia, K. Optical vortex trap for resonant confinement of metal nanoparticles. *Optics Express* **16,** 4991 (2008).

37. Perkins, T. T., Quake, S. R., Smith, D. E. & Chu, S. Relaxation of a single DNA molecule observed by optical microscopy. *Science* **264,** 822–826 (1994).

38. Bustamante, C., Bryant, Z. & Smith, S. B. Ten years of tension: single-molecule DNA mechanics. **421** (2003).

39. Zare, D. T. C. & N, R. Biased Diffusion, Optical Trapping, and Manipulation of Single Molecules in Solution. *Journal of the American Chemical Society* **118,** 6512 (1996).

40. Hirano, K. *et al.* Direct laser trapping of single globular DNA molecules. *Nucleic acids symposium series* **26,** 99–100 (1999).

41. Li, H., Zhou, D., Browne, H. & Klenerman, D. Evidence for resonance optical trapping of individual fluorophore-labeled antibodies using single molecule fluorescence spectroscopy. *Journal of the American Chemical Society* **128,** 5711–5717 (2006).

42. Hong, C., Yang, S. & Ndukaife, J. C. Stand-off trapping and manipulation of sub-10 nm objects and biomolecules using opto-thermo-electrohydrodynamic tweezers. *Nature Nanotechnology.* http://dx.doi.org/10.1038/s41565-020-0760-z (2020).

43. Murphy, D. Lenses and geometrical optics. *Fundamentals of Light Microscopy and Electronic Imaging. Wiley-Liss, Inc., New York,* 43–60 (2001).

44. Chirico, G., Fumagalli, C. & Baldini, G. Trapped brownian motion in single- and two-photon excitation fluorescence correlation experiments. *Journal of Physical Chemistry B* **106,** 2508–2519 (2002).

45. Brust, M. & Kiely, C. J. Some recent advances in nanostructure preparation from gold and silver particles: A short topical review. *Colloids and Surfaces A: Physicochemical and Engineering Aspects* **202,** 175–186 (2002).

46. Cha, J. *et al.* Infrared spectroscopy and X-ray reflectivity study on thermal stability of Langmuir-Blodgett film. *Synthetic Metals* **117,** 169–171 (2001).

47. Khomutov, G. B. *et al.* Formation of hybrid polyanion/metal cation/anionic surfactant films via interface complexation and Langmuir-Blodgett technique. *Colloids and Surfaces A: Physicochemical and Engineering Aspects* **198-200,** 509–517 (2002).

48. Blodgett, K. B. & Langmuir, I. Built-up films of barium stearate and their optical properties. *Physical Review* **51,** 964–982 (1937).

49. Huang, S., Tsutsui, G., Sakaue, H., Shingubara, S. & Takahagi, T. Experimental conditions for a highly ordered monolayer of gold nanoparticles fabricated by the Langmuir–Blodgett method. *Journal of Vacuum Science & Technology B: Microelectronics and Nanometer Structures* **19,** 2045 (2001).

50. Chen, S. Langmuir-Blodgett fabrication of two-dimensional robust cross-linked nanoparticle assemblies. *Langmuir* **17,** 2878–2884 (2001).

51. Tian, Y. & Fendler, J. H. Langmuir-Blodgett film formation from fluorescence-activated, surfactant-capped, size-selected CdS nanoparticles spread on water surfaces. *Chemistry of Materials* **8,** 969–974 (1996).

52. Stanković, N. K. *et al.* Antibacterial and Antibiofouling Properties of Light Triggered Fluorescent Hydrophobic Carbon Quantum Dots Langmuir-Blodgett Thin Films. *ACS Sustainable Chemistry and Engineering* **6,** 4154–4163 (2018).

53. R. K. Iler. Multilayers of colloidal particles. *Journal of colloid and interface science* **21,** 569–594 (1966).

54. Gao, Z. *et al.* Electrostatic self-assembly synthesis of ZnFe2O4 quantum dots (ZnFe2O4@C) and electromagnetic microwave absorption. *Composites Part B: Engineering* **179,** 107417 (2019).

55. Hees, J., Kriele, A. & Williams, O. A. Electrostatic self-assembly of diamond nanoparticles. *Chemical Physics Letters* **509,** 12–15 (2011).

56. Zhang, S., Shao, Y., Yin, G. & Lin, Y. Electrostatic self-assembly of a pt-around-au nanocomposite with high activity towards formic acid oxidation. *Angewandte Chemie - International Edition* **49,** 2211–2214 (2010).

57. Cooper, T. M., Campbell, A. L. & Crane, R. L. Formation of Polypeptide-Dye Multilayers by an Electrostatic Self-Assembly Technique. *Langmuir* **11,** 2713–2718 (1995).

58. Kumar, A., Mandale, A. B. & Sastry, M. Sequential electrostatic assembly of amine-derivatized gold and carboxylic acid-derivatized silver colloidal particles on glass substrates. *Langmuir* **16,** 6921–6926 (2000).

59. Ulman, A. *An Introduction to Ultrathin Organic Films: From Langmuir–Blodgett to Self–Assembly* (Academic press, 2013).

60. Rizza, R. *et al.* Self-Assembly of Monolayers of Semiconductor Nanocrystallites. *Chemistry of Materials* **9,** 2969–2982 (1997).

61. Nakanishi, T., Ohtani, B. & Uosaki, K. Fabrication and characterization of CdS-nanoparticle mono- and multilayers on a self-assembled monolayer of alkanedithiols on gold. *Journal of Physical Chemistry B* **102,** 1571–1577 (1998).

62. Ap, A. *et al.* Organization Of Nanocrystal Molecules Using DNA. *Nature* **382,** 609–611 (1996).

63. Storhoff, J. J., Elghanian, R., Mucic, R. C., Mirkin, C. A. & Letsinger, R. L. One-pot colorimetric differentiation of polynucleotides with single base imperfections using gold nanoparticle probes. *Journal of the American Chemical Society* **120,** 1959–1964 (1998).

64. Mitchell, G. P., Mirkin, C. A. & Letsinger, R. L. Programmed assembly of DNA functionalized quantum dots. *Journal of the American Chemical Society* **121,** 8122–8123 (1999).

65. Inoue, A., Sugimoto, H., Yaku, H. & Fujii, M. DNA assembly of silicon quantum dots/gold nanoparticle nanocomposites. *RSC Advances* **6,** 63933–63939. http://dx.doi.org/10.1039/C6RA13565J (2016).

66. Deegan, R. D. *et al.* Capillary flow as the cause of ring stains from dried liquid drops. *Nature* **389,** 827–829 (1997).

67. Brinker, C. J. Evaporation-induced self-assembly: Functional nanostructures made easy. *MRS Bulletin* **29,** 631–640 (2004).

68. Li, M., Schnablegger, H. & Mann, S. Coupled synthesis and self-assembly of nanoparticles to give structures with controlled organization. *Nature* **402,** 393–395 (1999).

69. Xu, J., Xia, J. & Lin, Z. Evaporation-induced self-assembly of nanoparticles from a sphere-on-flat geometry. *Angewandte Chemie - International Edition* **46,** 1860–1863 (2007).

70. Murray, C. B., Kagan, C. R. & Bawendi, M. G. Self-organization of CdSe nanocrystallites into three-dimensional quantum dot superlattices. *Science* **270,** 1335–1338 (1995).

71. Whetten, R. L. *et al.* Nanocrystal gold molecules. *Advanced Materials* **8,** 428–433 (1996).

72. Mayya, K. S. & Sastry, M. Colloidal Nanoparticle Superlattices. *Langmuir* **15,** 1902–1904 (1999).

73. Kraus, T. *et al.* Nanoparticle printing with single-particle resolution. **2** (2007).

74. Asbahi, M. *et al.* Large Area Directed Self-Assembly of Sub-10 nm Particles with Single Particle Positioning Resolution. *Nano Letters* **15,** 6066–6070 (2015).

75. Cui, Y. *et al.* Integration of colloidal nanocrystals into lithographically patterned devices. *Nano Letters* **4,** 1093–1098 (2004).

76. Huang, H. W., Bhadrachalam, P., Ray, V. & Koh, S. J. Single-particle placement via self-limiting electrostatic gating. *Applied Physics Letters* **93,** 7–10 (2008).

77. Jackson, J. D. & Fox, R. F. Classical Electrodynamics, 3rd ed . *American Journal of Physics* **67,** 841–842 (1999).

78. Hynninen, A. P. & Dijkstra, M. Phase diagram of dipolar hard and soft spheres: Manipulation of colloidal crystal structures by an external field. *Physical Review Letters* **94** (2005).

79. Fraden, S., Hurd, A. J. & Meyer, R. B. Electric-field-induced association of colloidal particles. *Physical Review Letters* **63,** 2373–2376 (1989).

80. Lumsdon, S. O., Kaler, E. W. & Velev, O. D. Two-Dimensional Crystallization of Microspheres by a Coplanar AC Electric Field. *Langmuir* **20,** 2108–2116 (2004).

81. Ristenpart, W. D., Aksay, I. A. & Saville, D. A. Electrically Guided Assembly of Planar Superlattices in Binary Colloidal Suspensions. *Physical Review Letters* **90,** 4 (2003).

82. Fagan, J. A., Sides, P. J. & Prieve, D. C. Evidence of multiple electrohydrodynamic forces acting on a colloidal particle near an electrode due to an alternating current electric field. *Langmuir* **21,** 1784–1794 (2005).

83. Hu, Y., Glass, J. L., Griffith, A. E. & Fraden, S. Observation and simulation of electrohydrodynamic instabilities in aqueous colloidal suspensions. *The Journal of Chemical Physics* **100,** 4674–4682 (1994).

84. Lele, P. P., Mittal, M. & Furst, E. M. Anomalous particle rotation and resulting microstructure of colloids in AC electric fields. *Langmuir* **24,** 12842–12848 (2008).

85. Gong, T., Wu, D. T. & Marr, D. W. M. Electric Field-Reversible Three-Dimensional Colloidal Crystals, 5967–5970 (2003).

86. Hermanson, K. D., Lumsdon, S. O., Williams, J. P., Kaler, E. W. & Velev, O. D. Dielectrophoretic assembly of electrically functional microwires from nanoparticle suspensions. *Science* **294,** 1082–1086 (2001).

87. Jinesh, K. B. & Frenken, J. W. M. Capillary condensation in atomic scale friction: How water acts like a glue. *Physical Review Letters* (2006).

88. Smoukov, S. K., Gangwal, S., Marquez, M. & Velev, O. D. Reconfigurable responsive structures assembled from magnetic Janus particles. *Soft Matter* **5,** 1285–1292 (2009).

89. Yan, J., Skoko, D. & Marko, J. F. Near-field-magnetic-tweezer manipulation of single DNA molecules. *Physical Review E - Statistical, Nonlinear, and Soft Matter Physics* **70,** 1–5 (2004).

90. Fisher, J. K. *et al.* Thin-foil magnetic force system for high-numerical-aperture microscopy. *Review of Scientific Instruments* **77** (2006).

91. Gosse, C. & Croquette, V. Magnetic tweezers: Micromanipulation and force measurement at the molecular level. *Biophysical Journal* **82,** 3314–3329 (2002).

92. Romano, G., Sacconi, L., Capitanio, M. & Pavone, F. S. Force and torque measurements using magnetic micro beads for single molecule biophysics. *Optics Communications* **215,** 323–331 (2003).

93. Vries, A. H. B. D., Krenn, B. E., Driel, R. V. & Kanger, J. S. Micro Magnetic Tweezers for Nanomanipulation Inside Live Cells. *Biophysical Journal* **88,** 2137–2144. http://dx.doi.org/10.1529/biophysj.104.052035 (2005).

94. Danilowicz, C., Greenfield, D. & Prentiss, M. Dissociation of Ligand - Receptor Complexes Using Magnetic Tweezers. **77,** 3023–3028 (2005).

95. Kohl, M., Krevet, B. & Just, E. SMA microgripper system. *Sensors and Actuators, A: Physical* **97-98,** 646–652 (2002).

96. Vurchio, F. *et al.* Toward operations in a surgical scenario: Characterization of a microgripper via light microscopy approach. *Applied Sciences (Switzerland)* **9** (2019).

97. Cagliani, A. *et al.* Manipulation and in situ transmission electron microscope characterization of sub-100 nm nanostructures using a microfabricated nanogripper. *Journal of Micromechanics and Microengineering* **20** (2010).

98. Yu, M.-F., Dyer, M. J., Skidmore, G. D., Rhors, H. W. & Lu, X. K., Ausman, K. D., Ehr, J. R. V., Ruoff, R. S. 3-dimensional manipulation of carbon nanotubes under a scanning electron microscope. Nanotechnology. **10,** 244 (1999).

99. Mølhave, K. & Hansen, O. Electro-thermally actuated microgrippers with integrated force-feedback. *Journal of Micromechanics and Microengineering* **15,** 1265–1270 (2005).

100. Andersen, K. N. *et al.* Multimodal electrothermal silicon microgrippers for nanotube manipulation. *IEEE Transactions on Nanotechnology* **8,** 76–85 (2009).

101. Carlson, K. *et al.* A carbon nanofibre scanning probe assembled using an electrothermal microgripper. *Nanotechnology* **18** (2007).

102. Kim, P. & Lieber, C. M. Nanotube nanotweezers. *Science* **286,** 2148–2150 (1999).

103. Sardan, O. *et al.* Rapid prototyping of nanotube-based devices using topology-optimized microgrippers. *Nanotechnology* **19** (2008).

104. Jonsmann, J., Sigmund, O. & Bouwstra, S. Compliant electro-thermal microactuators. *Technical Digest. IEEE International MEMS 99 Conference. Twelfth IEEE International Conference on Micro Electro Mechanical Systems (Cat. No.99CH36291),* 588–593. http://ieeexplore.ieee.org/document/746894/ (1999).

105. Fearing, R. Survey of sticking effects for micro parts handling. *Proceedings 1995 IEEE/RSJ International Conference on Intelligent Robots and Systems. Human Robot Interaction and Cooperative Robots* **2,** 212–217 (1995).

106. Zhang, Y., Chen, B. K., Liu, X. & Sun, Y. Autonomous robotic pick-and-place of microobjects. *IEEE Transactions on Robotics* **26,** 200–207 (2010).

107. Hériban, D. & Gauthier, M. Robotic micro-assembly of microparts using a piezogripper. *2008 IEEE/RSJ International Conference on Intelligent Robots and Systems, IROS,* 4042–4047 (2008).

108. Israelachvili, J. N. *Intermolecular and surface forces* (Academic press, 2011).

109. Kittel, C. Introduction to solid state physics (1976).

110. Meyer, G. & Amer, N. M. Novel optical approach to atomic force microscopy. *Applied Physics Letters* **53,** 1045–1047 (1988).

111. Erlandsson, R., McClelland, G. M., Mate, C. M. & Chiang, S. Atomic force microscopy using optical interferometry. *Journal of Vacuum Science & Technology A: Vacuum, Surfaces, and Films* **6,** 266–270 (1988).

112. Brugger, J., Buser, R. A. & De Rooij, N. F. Micromachined atomic force microprobe with integrated capacitive read-out. *Journal of Micromechanics and Microengineering* **2,** 218–220 (1992).

113. Tortonese, M., Barrett, R. C. & Quate, C. F. Atomic resolution with an atomic force microscope using piezoresistive detection. *Applied Physics Letters* **62,** 834–836 (1993).

114. Edwards, H., Taylor, L., Duncan, W. & Melmed, A. J. Fast, high-resolution atomic force microscopy using a quartz tuning fork as actuator and sensor. *Journal of Applied Physics* **82,** 980–984 (1997).

115. Sitti, M. Controlled pushing of nanoparticles: Modeling and experiments. *IEEE/ASME Transactions on Mechatronics* **5,** 199–211 (2000).

116. Baur, C. *et al.* Nanoparticle manipulation by mechanical pushing: Underlying phenomena and real-time monitoring. *Nanotechnology* **9,** 360–364 (1998).

117. Hansen, L Theil and Kühle, A and Sørensen, Alexis Hammer and Bohr, Jakob and Lindelof, P., L Theil Hansen, A Kuhl, A H Sørensen, J. B. & Lindelof. A technique for positioning nanoparticles using an atomic force microscope. **337** (1998).

118. Junno, T., Deppert, K., Montelius, L. & Samuelson, L. Controlled manipulation of nanoparticles with an atomic force microscope. *Applied Physics Letters* **66,** 3627–3629. http://aip.scitation.org/doi/10.1063/1.113809 (1995).

119. Requicha, A. A. G. *et al.* Manipulation of nanoscale components with the AFM: Principles and applications. *Proceedings of the IEEE Conference on Nanotechnology,* 81–86 (2001).

120. Hwang, G. *et al.* Manufacturing of 3D Helical Microswimmer by AFM Micromanipulation for Microfluidic Applications. *IEEE Transactions on Semiconductor Manufacturing,* 1–8 (2021).

121. Wang, P. *et al.* Modification of AFM tips for facilitating picking-up of nanoparticles. *Chinese Physics Letters* **25,** 2407–2409 (2008).

122. Dietzel, D. *et al.* Frictional duality of metallic nanoparticles: Influence of particle morphology, orientation, and air exposure. *Physical Review B - Condensed Matter and Materials Physics* **82,** 1–9 (2010).

123. Rao, A., Wille, M. L., Gnecco, E., Mougin, K. & Meyer, E. Trajectory fluctuations accompanying the manipulation of spherical nanoparticles. *Physical Review B - Condensed Matter and Materials Physics* **80,** 2–5 (2009).

124. Ritter, C., Heyde, M., Schwarz, U. D. & Rademann, K. Controlled translational manipulation of small latex spheres by dynamic force microscopy. *Langmuir* **18,** 7798–7803 (2002).

125. Liu, Zhiguo and Li, Zhuang and Wei, Gang and Song, Yonghai and Wang, LI and Sun, L. Manipulation, dissection, and lithography using modified tapping mode atomic force microscope. *Microscopy research and technique* **69,** 998–1004 (2006).

126. Kim, S., Ratchford, D. C. & Li, X. Atomic force microscope nanomanipulation with simultaneous visual guidance. *ACS Nano* **3,** 2989–2994 (2009).

127. Chen, H., Xi, N. & Li, G. CAD-guided automated nanoassembly using atomic force microscopy-based nonrobotics. *IEEE Transactions on Automation Science and Engineering* **3,** 208–217 (2006).

128. Chuang, C. H. & Hung, C. H. AFM manipulation of nanoparticles based on dielectrophoresis. *NEMS 2011 - 6th IEEE International Conference on Nano/Micro Engineered and Molecular Systems,* 923–927 (2011).

129. Brown, K. A., Aguilar, J. A. & Westervelt, R. M. Coaxial atomic force microscope tweezers. *Applied Physics Letters* **96,** 1–4. arXiv: 1001.5262 (2010).

130. Brown, K. A. & Westervelt, R. M. Proposed triaxial atomic force microscope contact-free tweezers for nanoassembly. *Nanotechnology* **20** (2009).

131. Brown, K. A. & Westervelt, R. M. Triaxial AFM probes for noncontact trapping and manipulation. *Nano Letters* **11,** 3197–3201 (2011).

132. Decossas, Sébastien and Mazen, Frédéric and Baron, Thierry and Brémond, Georges and Souifi, A. Atomic force microscopy nanomanipulation of silicon nanocrystals for nanodevice fabrication. *Nanotechnology* **14,** 1272–1278 (2003).

133. Toset, J., Casuso, I., Samitier, J. & Gomila, G. Deflection-voltage curve modelling in atomic force microscopy and its use in DC electrostatic manipulation of gold nanoparticles. *Nanotechnology* **18** (2007).

134. Cheng, H.-w. *et al.* Characterization of single 1.8-nm Au nanoparticle attachments on AFM tips for single sub-4-nm object pickup, 1–10 (2013).

135. Cheng, H.-w. *et al.* Simple and Fast Method To Fabricate Single-Nanoparticle-Terminated Atomic Force Microscope Tips (2013).

136. Kashani, H. G., Shokrolahi, S, Moayyer, H. A. & Panahi, M. S. nanomanipulation using high voltage electrostatic forces Experimental and numerical investigation of nanoparticle releasing in AFM nanomanipulation using high voltage electrostatic forces. **034305** (2017).

137. Xu, J., Kwak, K. J., Lee, J. L. & Agarwal, G. Lifting and Sorting of Charged Au Nanoparticles by Electrostatic Forces in Atomic Force Microscopy, 2105–2108 (2010).

138. Toset, J. & Gomila, G. Three-dimensional manipulation of gold nanoparticles with electro-enhanced capillary forces. *Applied Physics Letters* **96,** 2008–2011 (2010).

139. Lyu, Y. K., Ji, Z. T., He, T., Lu, Z. & Zhang, W. Automated pick-and-place of single nanoparticle using electrically controlled low-surface energy nanotweezer. *AIP Advances* **11.** https://doi.org/10.1063/5.0041145 (2021).

140. Vakarelski, I. U. & Higashitani, K. Single-Nanoparticle-Terminated Tips for Scanning Probe Microscopy, 2931–2934 (2006).

141. Vakarelski, I. U., Brown, S. C. & Moudgil, B. M. Nanoparticle – terminated scanning probe microscopy tips and surface samples. *Advanced Powder Technology* **18,** 605–614. http://dx.doi.org/10.1163/156855207782514905 (2007).

142. Obataya, I., Nakamura, C. & Han, S. Nanoscale Operation of a Living Cell Using an Atomic Force Microscope with a Nanoneedle (2005).

143. Ong, Q. K. & Sokolov, I. Attachment of nanoparticles to the AFM tips for direct measurements of interaction between a single nanoparticle and surfaces. **310,** 385–390 (2007).

144. Grabar, K. C. *et al.* Two-Dimensional Arrays of Colloidal Gold Particles : A Flexible Approach to Macroscopic Metal Surfaces, 2353–2361 (1996).

145. Park, J. & Lee, H. Specific immobilization of nanospheres on template fabricated by using atomic force microscope lithography. **258,** 133–135 (2005).

146. Jaschke, M. *et al.* The atomic force microscope as a tool to study and manipulate local surface properties. *Biosensors and Bioelectronics* **11,** 601–612 (1996).

147. Jaschke, M. & Butt, H. J. Deposition of Organic Material by the Tip of a Scanning Force Microscope. *Langmuir* **11,** 1061–1064 (1995).

148. Piner, R. D., Zhu, J., Xu, F. & Hong, S. "Dip-Pen" Nanolithography. **283,** 661–664 (1999).

149. Li, Y., Maynor, B. & Liu, J. Electrochemical AFM "dip-pen" nanolithography and more. *Chinese Journal of Inorganic Chemistry* **18,** 75–78 (2002).

150. Sheehan, P. E., Whitman, L. J., King, W. P. & Nelson, B. A. Nanoscale deposition of solid inks via thermal dip pen nanolithography. *Applied Physics Letters* **85,** 1589–1591 (2004).

151. Demers, L. M. & Mirkin, C. A. Combinatorial templates generated by dip-pen nanolithography for the formation of two-dimensional particle arrays. *Angewandte Chemie - International Edition* **40,** 3069–3071 (2001).

152. Demers, L. M., Park, S.-J., Taton, T. A., Li, Z. & Mirkin, C. A. Orthogonal Assembly of Nanoparticle Building Blocks on Dip-Pen Nanolithographically Generated Templates of DNA. *Angewandte Chemie International Edition* **40,** 3071–3073 (2001).

153. Ben Ali, M., Ondarçuhu, T., Brust, M. & Joachim, C. Atomic force microscope tip nanoprinting of gold nanoclusters. *Langmuir* **18,** 872–876 (2002).

154. Loh, O. *et al.* Nanofountain-probe-based high-resolution patterning and single-cell injection of functionalized nanodiamonds. *Small* **5,** 1667–1674 (2009).

155. Kim, K. H. *et al.* Direct delivery and submicrometer patterning of DNA by a nanofountain probe. *Advanced Materials* **20,** 330–334 (2008).

156. Meister, A., Liley, M., Brugger, J., Pugin, R. & Heinzelmann, H. Nanodispenser for attoliter volume deposition using atomic force microscopy probes modified by focused-ion-beam milling. *Applied Physics Letters* **85,** 6260–6262 (2004).

157. Choi, T. Y., Poulikakos, D. & Grigoropoulos, C. P. Fountain-pen-based laser microstructuring with gold nanoparticle inks. *Applied Physics Letters* **85,** 13–15 (2004).

158. Belmont, A. S., Sokuler, M., Haupt, K. & Gheber, L. A. Direct writing of molecularly imprinted microstructures using a nanofountain pen. *Applied Physics Letters* **90** (2007).

159. Sokuler, M. & Gheber, L. A. Nano fountain pen manufacture of polymer lenses for nano-biochip applications. *Nano Letters* **6,** 848–853 (2006).

160. Wu, B., Ho, A., Moldovan, N. & Espinosa, H. D. Direct deposition and assembly of gold colloidal particles using a nanofountain probe. *Langmuir* **23,** 9120–9123 (2007).

161. Yoo, J., Pyo, J. & Je, J. H. Single inorganic-organic hybrid nanowires with ambipolar photoresponse. *Nanoscale* **6,** 3557–3560 (2014).

162. Yoo, J., Jeong, S., Kim, S. & Je, J. H. A stretchable nanowire UV-Vis-NIR photodetector with high performance. *Advanced Materials* **27,** 1712–1717 (2015).

163. Suryavanshi, A. P., Hu, J. & Yu, M. F. Meniscus-controlled continuous fabrication of arrays and rolls of extremely long micro- And nano-fibers. *Advanced Materials* **20,** 793–796 (2008).

164. Suryavanshi, A. *Meniscus controlled three-dimensional nanofabrication* (University of Illinois at Urbana-Champaign, 2007).

165. Meister, A., Liley, M., Brugger, J., Pugin, R. & Heinzelmann, H. Nanodispenser for attoliter volume deposition using atomic force microscopy probes modified by focused-ion-beam milling. *Applied Physics Letters* **85,** 6260–6262 (2004).

166. Fang, A., Dujardin, E., Ondarc, T. & Cedex, T. Control of Droplet Size in Liquid Nanodispensing (2006).

167. Hwang, K., Shin, C. Y., Mingwu, R., Lee, S. H. & mo Kim, H. Design of a nano-printer based on AFPN (Active Fountain Pen Nano-lithography) using switch control. *Evolutionary Ecology* **25,** 977–985 (2011).

168. Shmuylovich, L., Shen, A. Q. & Stone, H. A. Surface morphology of drying latex films: Multiple ring formation. *Langmuir* **18,** 3441–3445 (2002).

169. Won, K. H., Weon, B. M. & Je, J. H. Polymer composite microtube array produced by meniscus-guided approach. *AIP Advances* **3** (2013).

170. Lynge Eriksen, R., Ricardo Daria, V. & Glückstad, J. Fully dynamic multiple-beam optical tweezers. *Optics Express* **10,** 597 (2002).

171. Binnig, G. K. The " Millipede "— More than one thousand tips for future AFM data storage We report on a new atomic force microscope. *IBM Journal of Research and Development* **44,** 323–340. http://ieeexplore.ieee.org/lpdocs/epic03/wrapper.htm?arnumber=5389137 (2000).

172. Schmid, G. & Simon, U. Gold nanoparticles: assembly and electrical properties in 1–3 dimensions. *Chem. Commun.,* 697–710. http://xlink.rsc.org/?DOI=B411696H (2005).

173. Online, V. Biological applications of gold nanoparticles. *Chemical Society Reviews* **37,** 1909–30. http://www.ncbi.nlm.nih.gov/pubmed/18762839 (2008).

174. Homberger, M. & Simon, U. On the application potential of gold nanoparticles in nanoelectronics and biomedicine. *Philosophical Transactions of the Royal Society A: Mathematical, Physical and Engineering Sciences* **368,** 1405–1453. http://rsta.royalsocietypublishing.org/cgi/doi/10.1098/rsta.2009.0275 (2010).

175. Venditti, I. Gold nanoparticles in photonic crystals applications: A review. *Materials* **10,** 1–18 (2017).

176. Love, J. C., Estroff, L. A., Kriebel, J. K., Nuzzo, R. G. & Whitesides, G. M. *Self-assembled monolayers of thiolates on metals as a form of nanotechnology* **4,** 1103–1169 (2005).

177. Gankin, A. *et al.* Molecular and Ionic Dipole Effects on the Electronic Properties of Si-/SiO2-Grafted Alkylamine Monolayers. *ACS Applied Materials and Interfaces* **9,** 44873–44879 (2017).

178. Chauhan, A. K. *et al.* Self-assembly of the 3-aminopropyltrimethoxysilane multilayers on Si and hysteretic current-voltage characteristics. *Applied Physics A: Materials Science and Processing* **90,** 581–589 (2008).

179. Ben Haddada, M. *et al.* Optimizing the immobilization of gold nanoparticles on functionalized silicon surfaces: Amine- vs thiol-terminated silane. *Gold Bulletin* **46,** 335–341 (2013).

180. Manifar, T., Rezaee, A., Sheikhzadeh, M. & Mittler, S. Formation of uniform self-assembly monolayers by choosing the right solvent: OTS on silicon wafer, a case study. *Applied Surface Science* **254,** 4611–4619 (2008).

181. Lin, S. Y., Yang, K. C. & Chen, L. J. Effect of surface hydrophobicity on critical pinning concentration of nanoparticles to trigger the coffee ring formation during the evaporation process of sessile drops of nanofluids. *Journal of Physical Chemistry C* **119,** 3050–3059 (2015).

182. Dalvi, V. H. & Rossky, P. J. Molecular origins of fluorocarbon hydrophobicity. *Proceedings of the National Academy of Sciences* **107,** 13603–13607 (2010).

183. Ketkar, S. 2021. https://rp.versummaterials.com/versummaterials/resource-center/versum-lab-notes/assay-means-purity-right/.

184. Hirai, H. & Aizawa, H. *Preparation of Stable Dispersions of Colloidal Gold in Hexanes by Phase Transfer* 1993.

185. Kyaw, H. H., Al-Harthi, S. H., Sellai, A. & Dutta, J. Self-organization of gold nanoparticles on silanated surfaces. *Beilstein Journal of Nanotechnology* **6,** 2345–2353 (2015).

186. He, H. X. *et al.* Fabrication of designed architectures of Au nanoparticles on solid substrate with printed self-assembled monolayers as templates. *Langmuir* **16,** 3846–3851 (2000).

187. Porter, M. D., Bright, T. B., Allara, D. L. & Chidsey, C. E. Spontaneously Organized Molecular Assemblies. 4. Structural Characterization of n-Alkyl Thiol Monolayers on Gold by Optical Ellipsometry, Infrared Spectroscopy, and Electrochemistry. *Journal of the American Chemical Society* **109,** 3559–3568 (1987).

188. Widrig, C. A., Chung, C. & Porter, M. D. The electrochemical desorption of n-alkanethiol monolayers from polycrystalline Au and Ag electrodes. *Journal of Electroanalytical Chemistry* **310,** 335–359 (1991).

189. Yang, F. *et al.* Nanoscale multilevel switching in Ge2Sb2Te5 thin film with conductive atomic force microscopy. *Nanotechnology* **27,** 35706 (2015).

190. Sebastian, A. *et al.* Resistance switching at the nanometre scale in amorphous carbon. *New Journal of Physics* **13** (2011).

191. Soh, E. J. *et al.* Filamentary High-Resolution Electrical Probes for Nanoengineering. *Nano Letters* **20,** 1067–1073 (2020).

192. Ovshinsky, S. R. Reversible electrical switching phenomena in disordered structures. *Physical Review Letters* **21,** 1450 (1968).

193. Yang, F. *et al.* Conductive Atomic Force Microscopy (C-AFM) observation of conducting nanofilaments formation in GeSbTe phase change materials. *Applied Physics A* **112,** 663–667 (2013).

194. Hong, S. S., Cha, J. J. & Cui, Y. One nanometer resolution electrical probe via atomic metal filament formation. *Nano letters* **11,** 231–235 (2010).

195. Pohl, H. A. Dielectrophoresis. *The behavior of neutral matter in nonuniform electric fields* (1978).

196. Leiterer, C. *et al.* High precision attachment of silver nanoparticles on AFM tips by dielectrophoresis. *Analytical and Bioanalytical Chemistry* **408,** 3625–3631. http://dx.doi.org/10.1007/s00216-016-9447-6 (2016).

197. Pethig, R. Dielectrophoresis: Status of the theory, technology, and applications. *Biomicrofluidics* **4** (2010).

198. Gierhart, B. C., Howitt, D. G., Chen, S. J., Smith, R. L. & Collins, S. D. Frequency dependence of gold nanoparticle superassembly by dielectrophoresis. *Langmuir* **23,** 12450–12456 (2007).

199. Cheon, D., Kumar, S. & Kim, G. H. Assembly of gold nanoparticles of different diameters between nanogap electrodes. *Applied Physics Letters* **96,** 1–4 (2010).

200. Xiong, X. *et al.* Directed assembly of gold nanoparticle nanowires and networks for nanodevices. *Applied Physics Letters* **91,** 1–4 (2007).

201. Gascoyne, P. R. & Vykoukal, J. Particle separation by dielectrophoresis.pdf. *Electrophoresis* **23,** 1973–1983. http://www.ncbi.nlm.nih.gov/pmc/articles/PMC2726256/ (2009).

202. Ding, H. *et al.* Influence of induced-charge electrokinetic phenomena on the dielectrophoretic assembly of gold nanoparticles in a conductive-island-based microelectrode system. *Langmuir* **29,** 12093–12103 (2013).

203. Li, M., Qu, Y., Dong, Z., Wang, Y. & Li, W. J. Limitations of au particle nanoassembly using dielectrophoretic force - A parametric experimental and theoretical study. *IEEE Transactions on Nanotechnology* **7,** 477–479 (2008).

204. Pacios, M. *et al.* Direct manufacturing of ultrathin graphite on three-dimensional nanoscale features. *Scientific Reports* **6,** 1–8. http://dx.doi.org/10.1038/srep22700 (2016).

205. Kim, D. *et al.* Electrical observations of filamentary conductions for the resistive memory switching in NiO films. *Applied physics letters* **88,** 202102 (2006).

206. Hoppe, H *et al.* Kelvin probe force microscopy study on conjugated polymer/fullerene bulk heterojunction organic solar cells. *Nano letters* **5,** 269–274 (2005).

207. Liu, L. & Li, G. Electrical characterization of single-walled carbon nanotubes in organic solar cells by Kelvin probe force microscopy. *Applied Physics Letters* **96,** 33 (2010).

208. Sarwat, S. G. *et al.* Revealing Strain-Induced Effects in Ultrathin Heterostructures at the Nanoscale. *Nano letters* **18,** 2467–2474 (2018).

209. Clack, N. G., Salaita, K. & Groves, J. T. Electrostatic readout of DNA microarrays with charged microspheres. *Nature biotechnology* **26,** 825 (2008).

210. Finot, E. *et al.* Effect of cholesterol on electrostatics in lipid- protein films of a pulmonary surfactant. *Langmuir* **26,** 1929–1935 (2010).

211. Girard, P. & Titkov, A. N. *Electrostatic Force and Force Gradient Microscopy: Principles, Points of Interest and Application to Characterisation of Semiconductor Materials and Devices* (eds Bhushan, B. & Fuchs, H.) 283–320. https://doi.org/10.1007/3-540-27453-7_9 (Springer Berlin Heidelberg, Berlin, Heidelberg, 2006).

212. Axt, A., Hermes, I. M., Bergmann, V. W., Tausendpfund, N. & Weber, S. A. Know your full potential: Quantitative Kelvin probe force microscopy on nanoscale electrical devices. *Beilstein Journal of Nanotechnology* **9,** 1809–1919 (2018).

213. Ziegler, D. & Stemmer, A. Force gradient sensitive detection in lift-mode Kelvin probe force microscopy. *Nanotechnology* **22** (2011).

214. Zerweck, U., Loppacher, C., Otto, T., Grafström, S. & Eng, L. M. Accuracy and resolution limits of Kelvin probe force microscopy. *Physical Review B* **71,** 125424 (2005).

215. Colchero, J., Gil, A. & Baró, A. M. Resolution enhancement and improved data interpretation in electrostatic force microscopy. *Physical Review B - Condensed Matter and Materials Physics* **64,** 1–11 (2001).

216. Mazzotta, G. *et al.* Solubilization of Carbon Nanotubes with Ethylene-Vinyl Acetate for Solution-Processed Conductive Films and Charge Extraction Layers in Perovskite Solar Cells. *ACS Applied Materials and Interfaces* **11,** 1185–1191 (2019).

217. Brown, K. A., Satzinger, K. J. & Westervelt, R. M. High spatial resolution Kelvin probe force microscopy with coaxial probes. *Nanotechnology* **23,** 115703 (2012).

218. Dörig, P. *et al.* Force-controlled spatial manipulation of viable mammalian cells and micro- organisms by means of FluidFM technology and micro-organisms by means of FluidFM technology. **023701,** 1–4 (2018).

219. Stiefel, P., Zambelli, T. & Vorholta, J. A. Isolation of optically targeted single bacteria by application of fluidic force microscopy to aerobic anoxygenic phototrophs from the phyllosphere. *Applied and Environmental Microbiology* **79,** 4895–4905 (2013).

220. Dörig, P. *et al.* Exchangeable colloidal AFM probes for the quantification of irreversible and long-term interactions. *Biophysical Journal* **105,** 463–472 (2013).

221. Berenschot, E. J. *et al.* 3D nanofabrication of fluidic components by corner lithography. *Small* **8,** 3823–3831 (2012).

222. Deladi, S. *et al.* Fabrication of micromachined fountain pen with in situ characterization possibility of nanoscale surface modification. *Journal of Micromechanics and Microengineering* **15,** 528–534 (2005).

223. Dorwling-Carter, L. *et al.* Simultaneous scanning ion conductance and atomic force microscopy with a nanopore: Effect of the aperture edge on the ion current images. *Journal of Applied Physics* **124** (2018).

224. Gauthier, M., Régnier, S., Rougeot, P. & Chaillet, N. Analysis of forces for micromanipulations in dry and liquid media. *Journal of Micromechatronics* **3,** 389–413 (2006).

225. Chandra, S. & Batur, C. Contact Angle Manipulation for Micro Gripping. **2060** (2014).

226. Fuchiwaki, O. & Kumagai, K. Development of Wet Tweezers Based on Capillary Force for Complex - Shaped and Heterogeneous Micro - Assembly, 1003–1009 (2013).

227. Grutzeck, H. & Kiesewetter, L. Downscaling of grippers for micro assembly. *Microsystem Technologies* **8,** 27–31 (2002).

228. Saftics, A. *et al.* Biomimetic Dextran-Based Hydrogel Layers for Cell Micropatterning over Large Areas Using the FluidFM BOT Technology. *Langmuir* (2019).

229. Ventrici De Souza, J. *et al.* Three-Dimensional Nanoprinting via Direct Delivery. *Journal of Physical Chemistry B* **122,** 956–962 (2018).

230. Grüter, R. R., Dielacher, B., Hirt, L., Vörös, J. & Zambelli, T. Patterning gold nanoparticles in liquid environment with high ionic strength for local fabrication of up to 100μm long metallic interconnections. *Nanotechnology* **26,** 1–10 (2015).

231. Hutchings, I. M. & Martin, G. D. *Inkjet Technology for Digital Fabrication* 1–372 (2012).

232. Beija, M., Afonso, C. A. & Martinho, J. M. Synthesis and applications of rhodamine derivatives as fluorescent probes. *Chemical Society Reviews* **38,** 2410–2433 (2009).

233. Zhang, J. *et al.* Controlled Molecular Assembly via Dynamic Confinement of Solvent. *Journal of Physical Chemistry Letters* **9,** 6232–6237 (2018).

234. Frederix, P., Werten, P. & Yablon, D. FluidFM: Precise fluidic positioning and delivery platform with applications in cell biology and soft matter. *Microscopy* (2018).

235. Haverinen, H. M., Myllyla, R. A. & Jabbour, G. E. Inkjet Printed RGB Quantum Dot-Hybrid LED. *Journal of display technology* **8,** 681–683 (2010).

236. Lodahl, P., Mahmoodian, S. & Stobbe, S. Interfacing single photons and single quantum dots with photonic nanostructures. *Reviews of Modern Physics* **87,** 347–400. arXiv: 1312.1079 (2015).

237. Michalet, X. Quantum Dots for Live Cells , **538,** 538–545 (2013).

238. Resch-Genger, U., Grabolle, M., Cavaliere-Jaricot, S., Nitschke, R. & Nann, T. Quantum dots versus organic dyes as fluorescent labels. *Nature Methods* **5,** 763–775 (2008).

239. Curto, A. G. *et al.* Unidirectional emission of a quantum dot coupled to a nanoantenna. *Science* **329,** 930–933 (2010).

240. Bai, Z. *et al.* Hydroxyl-Terminated CuInS2 Based Quantum Dots: Toward Efficient and Bright Light Emitting Diodes. *Chemistry of Materials* **28,** 1085–1091 (2016).

241. Zhang, Y. *et al.* Time-dependent photoluminescence blue shift of the quantum dots in living cells: Effect of oxidation by singlet oxygen. *Journal of the American Chemical Society* **128,** 13396–13401 (2006).

242. Lim, J. *et al.* Influence of shell thickness on the performance of light-emitting devices based on CdSe/Zn 1- X Cd x S core/shell heterostructured quantum dots. *Advanced Materials* **26,** 8034–8040 (2014).

243. Polovitsyn, A. *et al.* Synthesis of Air-Stable CdSe/ZnS Core-Shell Nanoplatelets with Tunable Emission Wavelength. *Chemistry of Materials* **29,** 5671–5680 (2017).

244. Saboktakin, M. *et al.* Metal-enhanced upconversion luminescence tunable through metal nanoparticle-nanophosphor separation. *ACS Nano* **6,** 8758–8766 (2012).

245. Talapin, D. V., Lee, J. S., Kovalenko, M. V. & Shevchenko, E. V. Prospects of colloidal nanocrystals for electronic and optoelectronic applications. *Chemical Reviews* **110,** 389–458 (2010).

246. Kim, B. H. *et al.* High-resolution patterns of quantum dots formed by electrohydrodynamic jet printing for light-emitting diodes. *Nano Letters* **15,** 969–973 (2015).

247. Palankar, R., Medvedev, N., Rong, A. & Delcea, M. Fabrication of quantum dot microarrays using electron beam lithography for applications in analyte sensing and cellular dynamics. *ACS Nano* **7,** 4617–4628 (2013).

248. Mayer, F. *et al.* Multimaterial 3D laser microprinting using an integrated microfluidic system. *Science Advances* **5,** 1–8 (2019).

249. Tang, L. *et al.* Nanometre-scale germanium photodetector enhanced by a near-infrared dipole antenna. *Nature Photonics* **2,** 226–229 (2008).

250. Cubukcu, E., Kort, E. A., Crozier, K. B. & Capasso, F. Plasmonic laser antenna. *Applied Physics Letters* **89** (2006).

251. Anker, J. N. *et al.* Biosensing with plasmonic nanosensors. *Nanoscience and Technology: A Collection of Reviews from Nature Journals* **7,** 308–319 (2009).

252. Zambrana-Puyalto, X. & Bonod, N. Purcell factor of spherical Mie resonators. *Physical Review B - Condensed Matter and Materials Physics* **91,** 1–11 (2015).

253. Dieleman, C. D. *et al.* Universal direct patterning of colloidal quantum dots by (extreme) ultraviolet and electron beam lithography. *Nanoscale* **12,** 11306–11316 (2020).

254. Nandwana, V. *et al.* Direct patterning of quantum dot nanostructures via electron beam lithography. *Journal of Materials Chemistry* **21,** 16859–16862 (2011).

255. Fu, Y. H. & Kuznetsov, A. I. *(12) United States Patent* (2020).

256. Daeneke, T *et al.* Liquid metals: fundamentals and applications in chemistry. *Chemical Society Reviews* **47,** 4073–4111 (2018).

257. Joshipura, I. D., Ayers, H. R., Majidi, C. & Dickey, M. D. Methods to pattern liquid metals. *Journal of materials chemistry c* **3,** 3834–3841 (2015).

258. Lin, Y. *et al.* Handwritten, soft circuit boards and antennas using liquid metal nanoparticles. *Small* **11,** 6397–6403 (2015).

259. Markvicka, E. J., Bartlett, M. D., Huang, X. & Majidi, C. An autonomously electrically self-healing liquid metal–elastomer composite for robust soft-matter robotics and electronics. *Nature materials* **17,** 618–624 (2018).

260. Wang, M., Trlica, C, Khan, M., Dickey, M. & Adams, J. A reconfigurable liquid metal antenna driven by electrochemically controlled capillarity. *Journal of Applied Physics* **117,** 194901 (2015).

261. Wang, J., Liu, S., Vardeny, Z. V. & Nahata, A. Liquid metal-based plasmonics. *Optics express* **20,** 2346–2353 (2012).

262. Reineck, P. *et al.* UV plasmonic properties of colloidal liquid-metal eutectic gallium-indium alloy nanoparticles. *Scientific reports* **9,** 1–7 (2019).

263. Mayyas, M. *et al.* Liquid-Metal-Templated Synthesis of 2D Graphitic Materials at Room Temperature. *Advanced Materials* **32,** 2001997 (2020).

264. Dickey, M. D. *et al.* Eutectic gallium-indium (EGaIn): a liquid metal alloy for the formation of stable structures in microchannels at room temperature. *Advanced functional materials* **18,** 1097–1104 (2008).

265. Dickey, M. D. *et al.* Eutectic gallium-indium (EGaIn): A liquid metal alloy for the formation of stable structures in microchannels at room temperature. *Advanced Functional Materials* **18,** 1097–1104 (2008).

266. Khan, M. R., Eaker, C. B., Bowden, E. F. & Dickey, M. D. Giant and switchable surface activity of liquid metal via surface oxidation. *Proceedings of the National Academy of Sciences* **111,** 14047–14051 (2014).

267. Farrell, Z. J. & Tabor, C. Control of gallium oxide growth on liquid metal eutectic gallium/indium nanoparticles via thiolation. *Langmuir* **34,** 234–240 (2018).

268. Tevis, I. D., Newcomb, L. B. & Thuo, M. Synthesis of liquid core–shell particles and solid patchy multicomponent particles by shearing liquids into complex particles (SLICE). *Langmuir* **30,** 14308–14313 (2014).

269. Yan, J. *et al.* Shape-controlled synthesis of liquid metal nanodroplets for photothermal therapy. *Nano Research* **12,** 1313–1320 (2019).

270. Chiechi, R. C., Weiss, E. A., Dickey, M. D. & Whitesides, G. M. Eutectic gallium–indium (EGaIn): a moldable liquid metal for electrical characterization of self-assembled monolayers. *Angewandte Chemie International Edition* **47,** 142–144 (2008).

271. Xiong, M., Gao, Y. & Liu, J. Fabrication of magnetic nano liquid metal fluid through loading of Ni nanoparticles into gallium or its alloy. *Journal of magnetism and magnetic materials* **354,** 279–283 (2014).

272. Shu, J. *et al.* Unconventional locomotion of liquid metal droplets driven by magnetic fields. *Soft Matter* **14,** 7113–7118 (2018).

273. Ma, B. *et al.* A versatile approach for direct patterning of liquid metal using magnetic field. *Advanced Functional Materials* **29,** 1901370 (2019).

274. Gozen, B. A., Tabatabai, A., Ozdoganlar, O. B. & Majidi, C. High-density soft-matter electronics with micron-scale line width. *Advanced materials* **26,** 5211–5216 (2014).

275. Cheng, S. & Wu, Z. Microfluidic electronics. *Lab on a Chip* **12,** 2782–2791 (2012).

276. Cumby, B. L. *et al.* Reconfigurable liquid metal circuits by Laplace pressure shaping. *Applied Physics Letters* **101,** 174102 (2012).

277. Ladd, C., So, J.-H., Muth, J. & Dickey, M. D. 3D printing of free standing liquid metal microstructures. *Advanced Materials* **25,** 5081–5085 (2013).

278. Chen, F., Hihath, J., Huang, Z., Li, X. & Tao, N. J. Measurement of single-molecule conductance. *Annual Review of Physical Chemistry* **58,** 535–564 (2007).

279. Xu, B. & Tao, N. J. Measurement of single-molecule resistance by repeated formation of molecular junctions. *Science* **301,** 1221–1223 (2003).

280. Wold, D. J. & Frisbie, C. D. Formation of a Metal - Molecule - Metal Junction by Contacting an Alkanethiol Self-Assembled Monolayer with Formation of Metal - Molecule - Metal Tunnel Junctions : Microcontacts to Alkanethiol Monolayers with a Conducting AFM Tip Department of, 2970–2971 (2000).

281. Kim, T. W., Wang, G., Lee, H. & Lee, T. Statistical analysis of electronic properties of alkanethiols in metal-molecule-metal junctions. *Nanotechnology* **18** (2007).

282. Beebe, J. M. & Kushmerick, J. G. Nanoscale switch elements from self-assembled monolayers on silver. *Applied Physics Letters* **90,** 18–21 (2007).

283. Milani, F., Grave, C., Ferri, V., Samorì, P. & Rampi, M. A. Ultrathin π-conjugated polymer films for simple fabrication of large-area molecular junctions. *ChemPhysChem* **8,** 515–518 (2007).

284. Akkerman, H. B., Blom, P. W., De Leeuw, D. M. & De Boer, B. Towards molecular electronics with large-area molecular junctions. *Nature* **441,** 69–72 (2006).

285. York, R. L., Nguyen, P. T. & Slowinski, K. Long-range electron transfer through monolayers and bilayers of alkanethiols in electrochemically controlled Hg-Hg tunneling junctions. *Journal of the American Chemical Society* **125,** 5948–5953 (2003).

286. Chiechi, R. C., Weiss, E. A., Dickey, M. D. & Whitesides, G. M. Eutectic gallium-indium (EGaIn): A moldable liquid metal for electrical characterization of self-assembled monolayers. *Angewandte Chemie - International Edition* **47,** 142–144 (2008).

287. Cademartiri, L. *et al.* Electrical resistance of Ag TS-S(CH 2) n -1CH 3//Ga 2O 3/EGaIn tunneling junctions. *Journal of Physical Chemistry C* **116,** 10848–10860 (2012).

288. Simeone, F. C. *et al.* Defining the value of injection current and effective electrical contact area for egain-based molecular tunneling junctions. *Journal of the American Chemical Society* **135,** 18131–18144 (2013).

289. Han, Y. & Nijhuis, C. A. Functional Redox-Active Molecular Tunnel Junctions. *Chemistry–An Asian Journal* **15,** 3752–3770 (2020).

290. Han, Y. *et al.* Electric-field-driven dual-functional molecular switches in tunnel junctions. *Nature materials* **19,** 843–848 (2020).

291. Lear, T. R. *et al.* Liquid metal particle popping: Macroscale to nanoscale. *Extreme Mechanics Letters* **13,** 126–134 (2017).

292. Larsen, R. J., Dickey, M. D., Whitesides, G. M. & Weitz, D. A. Viscoelastic properties of oxide-coated liquid metals. *Journal of rheology* **53,** 1305–1326 (2009).

293. Daniel, D. *et al.* Mapping Micrometer-Scale Wetting Properties of Superhydrophobic Surfaces. *Proc. Natl. Acad. Sci. U.S.A.* **116,** 50 (2019).

294. Daniel, D. *et al.* Quantifying Surface Wetting Properties Using Droplet Probe Atomic Force Microscopy. *ACS Applied Materials & Interfaces* **12,** 42386–42392 (2020).

295. Xie, L., Shi, C., Cui, X. & Zeng, H. Surface Forces and Interaction Mechanisms of Emulsion Drops and Gas Bubbles in Complex Fluids. *Langmuir* **33,** 3911–3925 (2017).

296. Escobar, J. V., Garza, C. & Castillo, R. Measuring Adhesion on Rough Surfaces Using Atomic Force Microscopy with a liquid probe. *Beilstein J. Nanotechnol.* **8,** 813–825 (2017).

297. Handschuh-Wang, S., Chen, Y., Zhu, L. & Zhou, X. Analysis and Transformations of Room-Temperature Liquid Metal Interfaces–A Closer Look through Interfacial Tension. *ChemPhysChem* **19,** 1584–1592 (2018).

298. Daniel, D. *Codes for Solving Young-Laplace Equation* https://github.com/ddaniel331/laplace_solver_2. Accessed: 2021-06-08. 2021.

299. Morris, N. J., Farrell, Z. J. & Tabor, C. E. Chemically modifying the mechanical properties of core–shell liquid metal nanoparticles. *Nanoscale* **11,** 17308–17318 (2019).

300. Yunusa, M., Amador, G. J., Drotlef, D.-M. & Sitti, M. Wrinkling instability and adhesion of a highly bendable gallium oxide nanofilm encapsulating a liquid-gallium droplet. *Nano lett.* **18,** 2498–2504 (2018).

301. Karuppannan, S. K., Neoh, E. H. L., Vilan, A. & Nijhuis, C. A. Protective Layers Based on Carbon Paint To Yield High-Quality Large-Area Molecular Junctions with Low Contact Resistance. *Journal of the American Chemical Society* **142,** 3513–3524 (2020).

302. Puebla-Hellmann, G., Venkatesan, K., Mayor, M. & Lörtscher, E. Metallic nanoparticle contacts for high-yield, ambient-stable molecular-monolayer devices. *Nature* **559,** 232–235 (2018).

303. Jeong, H. *et al.* A new approach for high-yield metal–molecule–metal junctions by direct metal transfer method. *Nanotechnology* **26,** 025601 (2014).

304. Yuan, L., Jiang, L. & Nijhuis, C. A. The Drive Force of Electrical Breakdown of Large-Area Molecular Tunnel Junctions. *Advanced Functional Materials* **28,** 1801710 (2018).

305. Stathis, J. H. Percolation models for gate oxide breakdown. *Journal of applied physics* **86,** 5757–5766 (1999).